SOLID STATE NMR INVESTIGATIONS OF LIPID BILAYERS AND BIOMEMBRANE BINDING MOLECULES: DENDRIMERS AND AMYLIN

by

Pieter E. S. Smith

A dissertation submitted in partial fulfillment
of the requirements for the degree of
Doctor of Philosophy
(Biophysics)
in The University of Michigan
2010

Doctoral Committee:

Professor Ayyalusamy Ramamoorthy, Chair
Professor Hashim M. Al-Hashimi
Professor Mark M. Banaszak Holl
Professor Zhan Chen
Professor Adam J. Matzger

"Because if you're not somebody, you're gonna be somebody's fool"
- Laurence Tureaud (Mr. T)

To my parents, for their love, support and encouragement. To ouma Marthie, for her compassion and wisdom. To my brothers, for being great company and being "fine young men." To my friends, Akash, Neil, Ron, Chamaree, Ravi, Matt, and many others, for making life more enjoyable. To my labmates, for sharing their food with me. And for sharing in my other experiences (both good and bad). To Shivani, for her infectious enthusiasm.

ACKNOWLEDGEMENTS

I would like to thank my advisor, Dr. Ramamoorthy, for supplying an environment conducive to discovery and learning.

I would also like to thank Drs. Ronald Soong, Jeffrey Brender, and Ulrich Dürr who taught me a great deal about NMR and biophysics in general. I especially appreciate their genuine enthusiasm for science and their openness. Thanks to Dr. Jiadi Xu, Kazutoshi Yamamoto, and Chris Kojiro for helping maintain our NMR spectrometers and for their advice on various NMR-related topics.

I would like to thank Drs. Takegoshi, Takeda, and all the other members of the Takegoshi lab at Kyoto University for accomodating me during my stay. They also helped me learn a great deal about the detailed functioning of NMR spectrometers, about pulse programming, and spin physics. Furthermore, I would like to thank the Biophysics program and the Kyoto University Global COE program for enabling my visit to the Takegoshi lab.

A Merit Fellowship from University of Michigan's Rackham graduate school supported me during my studies. This research was supported by funding from the National Institutes of Health (NIH) (please see the end of chapter acknowledgements). Funding from the NIH and the National Science Foundation supported the NMR instruments used in this work.

TABLE OF CONTENTS

LIST OF FIGURES

LIST OF APPENDICES

ABSTRACT

The goal of this project was to investigate the interaction between lipid binding molecules, such as peptides and drug compounds, with biological lipid bilayers. The results demonstrate that human amylin, a peptide hormone implicated in type II adult onset diabetes, disrupts cell membranes via a curvature inducing mechanism. In order to assess the effects that the various membrane-associated molecules have on lipid bilayers, a combination of differential scanning calorimetry (DSC) and solid state NMR methods were used. The amyloidogenic and toxic $hIAPP_{1-37}$ peptide, the non-toxic and non-amyloidogenic $rIAPP_{1-37}$ peptide, and the toxic but largely non-amyloidogenic $rIAPP_{1-19}$ and $hIAPP_{1-19}$ fragments were characterized. It is also shown that hyperbranched polymers with nanotherapeutic applications, known as poly(amidoamine) dendrimers, are thermodynamically stable when inserted inside zwitterionic lipid bilayers using ^{1}H radio frequency driven dipolar recoupling (RFDR) and ^{1}H magic angle spinning (MAS) nuclear Overhauser effect spectroscopy (NOESY) techniques. ^{14}N and ^{31}P NMR experiments on static samples and measurements of the mobility of C-H bonds using a 2D proton detected local field protocol under MAS corroborate these results. The localization of dendrimers in the hydrophobic core of lipid bilayers restricts the motion of bilayer lipid tails, with the smaller G5 dendrimer having more of an effect than the larger G7 dendrimer. Furthermore, solid state NMR techniques are developed to study the lipid bilayers and the molecules that associate with them. These methods drastically increase the spectral resolution of 2D solid state NMR techniques and allow more accurate

structure and dynamics information to be extracted from solid phase NMR samples. These techniques, known as separated local field (SLF) techniques, are used to obtain information about the orientation dependent local fields at each chemical site in a molecule under investigation. SLF techniques have been very important in the extraction of structural information from aligned samples in the solid state. Furthermore, a method is proposed to enable resonance assignment to be made on uniformly labeled samples. This method promises to overcome many of the difficulties inherent in solid state NMR studies of the structure and dynamics of biological membranes and the molecules that associate with them.

CHAPTER 1

INTRODUCTION

The structural biology of biomembranes and the molecules that associate with them has rapidly evolved into a new frontier of science. Although there are still a few major challenges, solid state NMR spectroscopy has become an invaluable tool in obtaining structural images of membrane proteins and other biomembrane associated molecules under physiological conditions.

In this project, solid state NMR was used to understand the interaction of therapeutics with cell membranes and to probe the pathological membrane disruptive properties of amylin, a peptide implicated in type II diabetes. The results demonstrate amylin disrupts cell membranes via a curvature inducing mechanism, a finding that may significantly aid in the development of treatments for adult-onset diabetes. Furthermore, the interaction between cell membranes and poly(amidoamine) (PAMAM) dendrimers, which show great promise in targeted drug delivery and gene therapy applications, were studied. It is expected that understanding PAMAM dendrimers' interactions with membranes will aid the development of more effective dendrimer-based therapeutic nanodevices. Solid state NMR studies show that PAMAM dendrimers are thermodynamically stable when intercalated in zwitterionic lipid bilayers and may therefore localize in the hydrophobic core of lipid bilayers.

Moreover, the dual limitations of low sensitivity and low resolution that often face solid state NMR spectroscopists are addressed with the development of new solid state NMR techniques. These techniques have improved the resolution achieved when measuring weak dipolar couplings via proton evolved local field solid (PELF) state NMR experiments and made them more applicable to the structural studies of membrane proteins and other cell membrane associated molecules by greatly increasing the quantity and quality of the structural and dynamical information that might be extracted from PELF spectra.

1.1 Lipid membranes

Lipid membranes envelop the contents of the cells, allowing them to maintain chemical environments optimal for the biochemical reactions that sustain their life. Furthermore, membranes can serve to create other unique compartments within cells each with their own unique chemical environments. Because of their important roles as creators of unique chemical environments, they represent targets for cytotoxic agents. Moreover, because lipid membranes form a barrier to the inner contents of cells of the human body, they are often a first point of contact pharmaceuticals. And because of their ubiquity in the human body, they are implicated in the pathology of various diseases, including type II diabetes (1-5).

The quantitative study of lipid membranes reveals that they are far more than inert barriers (6-8). Experiments show that far from being a passive bystander in the function of membrane proteins, the membrane can have a reciprocal relationship with the biomolecules associated with it, with both biomolecule and lipid membrane changing the biophysical properties of each other. The properties of the plasma membrane determine

how amyloid peptides such as hIAPP (1-5), lipophilic drugs such as curcumin (9-10), and membrane proteins such as mechanosensitive membrane channels (6, 11-13) interact with them.

The properties of cell membranes can be mimicked in lipid bilayers. Natural lipid bilayers are mostly made up of phospholipids, which are made up of a phosphate group, a diglyceride, and an organic molecule such as choline (Figure 1.1) (14). Several properties of lipids can influence their interaction with their environments. These include intrinsic bilayer curvature, bilayer thickness, and acyl chain characteristics. Bilayer properties are determined by the size and charge of the headgroup and the length and degree of unsaturation of the acyl chains. Although lipid bilayers constructed from one or a few synthetic phospholipids neglect the protein component of biological membranes, they provide a simple and convenient system for investigating the role of different lipid properties in modulating biomembrane-molecule interactions.

Membranes composed of lipids with phosphatidylethanolamine (PE) headgroups (Figure 1.1A) have a tendency to form curved surfaces, and are therefore useful for the study of biological membranes possessing a high degree of curvature. The binding of amyloid peptides to pancreatic islet cell membranes is sensitive to the presence of anionic lipids, such as lipids with the phosphatidylglycerol (PG) headgroup (Figure 1.1C) (15). Because negatively charged membranes are common in nature, PG lipid bilayers are a good mimic of a plethora of naturally occurring biological lipid membranes, including the membranes of pancreatic islet cells and bacteria (14). The outer leaflet of most eukaryotic cells' cell membrane is composed principally of lipids with

phosphatidylcholine (PC) headgroups (14). For this reason, PC lipid bilayers may be used to model most eukaryotic lipid membranes.

The fluidity of biological membranes is important to the functioning of membrane associated molecules, such as mechanosensitive channels. Bilayer fluidity is affected by the incorporation of cholesterol, the degree of lipid acyl chain saturation, and the properties of their acyl chains. Bilayers may be composed of lipids with symmetric acyl chains (both acyl chains are the same) or lipids with assymetric acyl chains (different acyl chains). 1-palmitoyl-2-oleoyl-glycerophospholipids (PO-glycerophospholipids), one type of lipid that is used in these studies, have a 16 carbon long, saturated (no double bonds), palmitoyl chain in the first position and an 18 carbon long oleoyl chain with a double bond between C9 and C10 in the second position (the carbons of the acyl chains are labeled starting with the carbon closest to the lipid headgroup). PO-glycerophospholipids are convenient because they are common in natural biological lipid membranes, have favorable thermodynamic properties and phase behavior, and are commercially available at a reasonable cost. Dimyristoyl-glycerophospholipids (DM-glycerophospholipids) are symmetric lipids and have two 14 carbon, saturated myristoyl chains in both acyl chain positions. These lipids are particularly amenable to the study of a lipid liquid crystalline to gel phase transition with occurs near room temperature (~24 °C), are in physiologically relevant phase at physiological temperatures, and are also commercially available at a reasonable cost. Furthermore, the properties of DM-glycerophospholipids are well known, which make them a good model system for studying molecules' interactions with lipids (16).

Because lipids are amphipathic, in aqueous environments they tend to arrange in a manner that sequesters the hydrophobic regions from the aqueous phase. Depending on various properties of the lipids and the thermal energy available to them, aqueous aggregates of lipids might adopt various supermolecular structures as illustrated in Figure 1.2. Cell membrane lipids normally assume a fluid lamellar phase (Figure 1.2B). In this phase, a lipid bilayer forms, with lipid headgroups facing the aqueous phase on either side of the bilayer and the lipid acyl chains (tails) forming the hydrophobic core of the lipid bilayer. The lipid bilayer in this phase might be described as a sheet-like, or lamellar, structure with two layers or leaflets of lipids arranging to sequester the hydrophobic lipid tails. In this phase, lipid bilayers will form vesicles, which assures that there is no contact between water molecules and the hydrophobic core of the lipid bilayer. This phase might be described as a two dimensional fluid phase with lipids diffusing rapidly within the plane of the lipid bilayer and rotating rapidly about an axis normal to the plane of the bilayer. Nevertheless, motion perpendicular to the plane of the lipid bilayer and flip-flop between the leaflets of the lipid bilayer. The acyl chains of the lipids are highly flexible, and, assuming no carbon-carbon double bonds, rotation about carbon-carbon bonds of the acyl chain is unhindered. In fact, there is a finite, but small, probability that the terminal methyl group of the acyl chains of the lipid molecule would be near the glycerol region of a lipids. Furthermore, in the dynamic sheet-like arrangement of the lipid bilayer, water molecules penetrate down to the glycerol backbone of the lipid molecule, which defines the hydrophobic/hydrophilic interface of the lipid bilayer. The gel phase of lipid bilayers, which occurs at lower temperatures, is characterized by the lipids' tails being in an extended, all-trans, conformations, and

oriented slightly away from the lipid bilayer normal. In this phase, lipid molecules become more rigid (14, 17).

However, the lamellar arrangement of lipids into bilayers is not stable for all lipids. Depending on the cross-sectional areas that different regions (the headgroup and acyl chains) of the lipid molecule occupy, aqueous mixtures of lipids might assume any of a number of non-lamellar phases. Various aspects of lipids' chemical environments might affect the relative cross-sectional area that their headgroups and acyl chains occupy, including pH, the level of hydration, and temperature. Lipids that have a smaller acyl chains, relative to their headgroups, prefer to form supermolecular structures characterized by negative curvature, such as the inverted cylinders that characterize the inverted hexagonal phase illustrated in Figure 1.2D. On the other hand, lipids that have smaller headgroups, relative to their acyl chains, prefer to form supermolecular structures characterized by positive curvature, such as the cylindrical structures that characterize the regular hexagonal phase illustrated in Figure 1.2D. In these phases, rapid lipid translation, rotation, and acyl chain motion occurs just as in the fluid lamellar phase.

Lipids in a lamellar phase might experience a force tending to curve them, or curvature strain (18). This force might be imparted by peptides which tend to change the cross-sectional area occupied by lipid tails relative to the cross sectional area occupied by lipid headgroups. Increases in temperature will increase the cross-sectional area occupied by the lipid tails faster than it will increase the cross-sectional area occupied by lipid headgroups, which may lead to increased negative curvature strain or to a transition to negatively curved phases. Furthermore, membrane curvature, through its effects on the lateral pressure profile of the membrane of the lipid bilayer, affects the function

membrane associated proteins and peptides. Non-lamellar lipid phases may be formed temporarily in the process of vesicle budding, membrane fusion, and other membrane processes (14, 17-21). Furthermore, the formation non-lamellar phases is relevant to the pathology of amyloid peptide aggregates and in the function of antimicrobial peptides and curvature strain is believed to play a particularly important role in the formation of toroidal pore or wormhole structures. Importantly, mixtures of long and short chained lipids known as bicelles can produce supermolecular structures that mimic toroidal pores and are therefore useful in the study of peptides' curvature strain inducing properties (2).

1.2 Bicelles

Bicelles are a model membrane system used predominately for biophysical studies of membrane-associated amphiphiles (22-24). It is an aqueous mixtures of long chain lipids (DMPC, commonly) and short chain lipids or detergents (DHPC, commonly). These mixtures are stable over a wide range of lipid concentrations, temperatures, and [DMPC]/[DHPC] ratios, known as q-ratios (25-26). Bicelles with a q>2.5 have a tendency to align in a magnetic field. This alignment is exhibited in a temperature range of approximately ~30-45 °C and a variety of lipid concentrations (25, 27-28).

These lipid mixtures align because of the anisotropy of the diamagnetic susceptibility tensor, $\Delta\chi = \chi_{\parallel} - \chi_{\perp}$, where $\chi_{\parallel}$ and $\chi_{\perp}$ represent the volume magnetic susceptibilities of bicelle lipids parallel and perpendicular, respectively, to the lipids' long molecular axis (22, 29-31). Because the lipids in a bicelle mixture have a tendency to arrange in the "swiss cheese" configuration shown in figure 1.3C, the tendency of the bicelle lamellae to align with the magnetic field is a consequence of the aggregate sum of

the alignment forces experienced by individual lipid molecules. For phospholipids, it is generally the case that $\Delta\chi < 0$. The Helmholtz free energy density of the bicelle aggregates is given by (31):

$$F(\beta_{ln}) = -\frac{1}{2}N\Delta\chi\left(\vec{n}\cdot\vec{B}\right)^2 \qquad [1.1]$$

where β_{ln} is the angle between the bilayer normal, $\vec{n}$, and the magnetic field, $\vec{B}$, and *N* is the number of lipid molecules per unit volume. According to the above equation, the Helmholtz free energy is lowest when the bicelle bilayer normal is oriented perpendicular to the spectrometer magnetic field. Because $\Delta\chi < 0$, these bicelles are said to be negatively aligned in this case. Bicelles may be reoriented so that their bilayer normal is parallel to the spectrometer magnetic field by the addition of trivalent lanthanide cations with a large enough positive magnetic susceptability anisotropy, such as Eu^{3+}, Tm^{3+}, Yb^{3+}, or Er^{3+} (31) (figure 1.4). Because in these bicelles, $\Delta\chi > 0$, lanthanide-doped bicelles are said to be positively aligned.

Only a small amount of lanthanide ions are needed to change the orientation of bicelles. These ions preferentially associate with the phosphate moiety of lipids. In fact, lanthanide-doped positively aligned bicelles were originally developed as an alternative to sandwiching lipids between glass plates and mechanically aligning them (30-32). Positively aligned bicelles are easier to prepare than negatively aligned bicelles and tolerate higher levels of hydration. However, the possibility of lanthanide ions interacting with the proteins or other membrane associated molecules under study limits their applications. Chelated lipids may be used to overcome problems associated with lanthanide ions interacting with molecules under study (30).

In recent years, the morphology of bicelles has been well-characterized and a general agreement over the structure of bicelles under different conditions has generally been achieved. This agreement has been facilitated especially by small angle neutron (SANS) and NMR (27, 33-34). Diagrams of bicelle morphology are shown in figure 1.3. At $q<2$ or below the gel-to-liquid crystalline phase transition of DMPC, DMPC/DHPC bicelles are disc shaped, with DHPC arranged around the periphery of these discs. At $q\sim2$, or near DMPC's gel-to-liquid crystalline phase transition, negatively aligned DMPC/DHPC bicelle mixtures enter a nematic phase, adopting supermolecular structures of DMPC-rich ribbons with their edges coated with DHPC (34). In positively aligned bicelles, the dominant morphology appears to be DMPC lamallae with wormhole or toroidal pore perforations, resembling slices of swiss cheese. Phase diagrams for positively and negatively aligned bicelles are provided in figures 1.5 and 1.6. These figures are adapted from (33). Note that it is possible for bicelle lipid mixtures to adopt a multilamellar vesicle morphology at certain temperatures and hydration levels.

Notably, the wormhole structure of the perforations of bicelle lamellae mimics the toroidal pore structure suspected to be formed in the process of many peptides' membrane disruption (35-37). It has been demonstrated that bicelles are useful as a model membrane system for studying peptides' affinity for the curved regions of toroidal pores. In particular, they have been used to study the pathological membrane association of the type II diabetes peptide, amylin, also known as human Islet Amyloid Polypeptide (hIAPP) (2).

1.3 The involvement of human Islet Amyloid Polypeptide in the pathology of type II, adult-onset diabetes

Type II diabetes mellitus is a clinical syndrome that manifests as decreased insulin sensitivity and increased blood glucose levels. Furthermore, it is also associated with amyloid deposits in the pancreatic islets of Langerhans and decreased insulin production by pancreatic β-cells. In 1987, the protein component of islet amyloid was determined to be hIAPP (38-39). Human IAPP is coexpressed and cosecreted with insulin by pancreatic β-cells. The aggregation of hIAPP has been shown to be key to the loss of β-cell mass (40-42). By disrupting β-cell membranes, hIAPP aggregates allow the entry of Ca^{2+} ions into the cell, which imposes oxidative stress on the β-cell as its mitochondria attempt to maintain the cell's ion balance (43-49).

The amyloid deposits associated with type II diabetes are similar to amyloid deposits associated with neurodegenerative diseases such as Huntington's disease (50), Alzheimer's disease (51-54), prion encephalopathy (55), amyotrophic lateral sclerosis (56), and Parkinson's disease (57-58). Furthermore, in both neurodegenerative diseases and type II diabetes, cell loss is associated with abnormal aggregation of a locally expressed protein. Because these proteins all share a tendency to aggregate in aqueous environments, the question of whether amyloid formation is a cause or consequence of cell death arose. Those who favored amyloid as having a primary role in neurodegenerative disease coined the term "amyloid hypothesis" (51).

A number of articles of evidence have been put forth in support of the amyloid hypothesis for neurodegenerative diseases. The amyloid peptide responsible for Alzheimer's diseases is amyloid-β (Aβ), which is a cleaved fragment of the amyloid

precursor protein (APP). Genetic mutations of the APP gene that increase the self-aggregation of Aβ lead Alzheimer's disease (59). Furthermore, Alzheimer's disease is also caused by mutations that enhance the processing of APP into amyloidogenic Aβ (60). Furthermore, evidence suggests that genetic variability in Aβ amyloid clearance may conribute to the risk of late-onset Alzheimer's disease (61-65). Despite the similarity of amyloid deposition being associated with the pathology of Alzheimer's disease and type II diabetes, however, it is not clear that the β-cell cytotoxicity of hIAPP is related to amyloid deposition and clearance.

It has been observed that the severity of the type II diabetes disease state often correlates poorly with the extent of amyloid deposition (66). Islet amyloid is found in nondiabetic individuals and is associated with aging (67). Furthermore, islet amyloid is not present in all islets in people with type II diabetes (68). Several studies have argued for small, nonfibrillar oligomers as the toxic forms of amyloid proteins (44, 69-71). An alternative hypothesis proposed by Engel et al. (72) is that it is the process of fiber growth, and not the fibers themselves or any particular aggregated species of hIAPP, that is responsible for the membrane disrupting properties of hIAPP. Nevertheless, it has been shown that a truncated version of hIAPP, $hIAPP_{1-19}$, a peptide that does not form fibers, is as at least as membrane disrupting as full length hIAPP (73). Moreover, $hIAPP_{1-19}$ displays the same curvature inducing properties as full length hIAPP (2).

1.4 Poly(amidoamine) dendrimers and lipid membranes

Understanding the interaction of nanoparticles with biological membranes (either the plasma membranes of living cells or their organelle membranes) is of vital for designing medical nanotherapeutics. In particular, poly(amidoamine) (PAMAM)

dendrimer nanoparticles have varied applications because of their controlled size, uniformity, easily modifiable surface chemistry, and aqueous solubility (74). Although targeting therapeutics is best accomplished with minimal dendrimer-membrane interaction to avoid interference with the targeting groups (75-79), a strong dendrimer-membrane interaction is necessary for systemic therapeutics, such as transfection vectors, to facilitate delivery of their cargo through membranous barriers (80-82). Because of the increased use of nanoparticles in commercial applications, there is increased concern over the possibility of the adverse effects nanoparticles might have upon human or environmental exposure (83-86). Previous studies have shown that the net charge and the surface area of the nanoparticle are the main determinants of membrane disruption (85-86). Furthermore, it has been shown that membrane binding, pore formation, and leakage are induced by cationic nanoparticles (81, 87-94).

What follows is an exposition on the various techniques used to study lipid bilayers in this project. The intention is to provide sufficient background for a general reader to understand and appreciate the work presented in later chapters.

1.5 Solid state NMR

The investigation of lipid bilayer systems presents a unique challenge. Many techniques cannot be used because of the nature of the lipid sample under investigation. X-ray crystallography, solution NMR, X-ray and neutron diffraction have been used to study lipid bilayer systems, but the use of these technique typically requires sample conditions that preclude the use of physiologically relevant, fully-hydrated lipid bilayers. Although fluorescence methods may be used to study fully hydrated lipid bilayers, their use often requires labels that may interfere with normal peptide-lipid interaction. Other

techniques, such as differential scanning calorimetry (DSC), CD, and FTIR only provide average information on lipid dynamics and structure, and DSC is limited to lipids and temperature conditions with observable phase changes. Therefore solid state NMR is often the most appropriate technique for obtaining obtaining atomic-level structural and dynamic data on lipids and lipid associated molecules in the solid state.

Despite the many advantages of using solid state NMR methods for the study of membrane systems, there are also challenges associated with the use of solid state NMR methods. Solid-state NMR is characterized by a lack of isotropic motion on NMR timescales. Because motions are slow, anisotropic interactions are not averaged out. Broad lines with complex lineshapes, containing a wealth of structural and dynamic information result. This data has often been used to study the structure and dynamics of peptide and lipid systems (2, 95-105). Nevertheless, the breadth of solid-state NMR resonances can have dramatic obscuring effects. Often it is difficult or impossible to resolve more than one resonance line. The main interactions leading to poor resolution in solid state NMR spectra studied here include the anisotropic shielding of the magnetic field by electrons (chemical shift anisotropy or CSA) and the through-space interaction of the magnetic dipoles of NMR active nuclei (dipolar coupling).

NMR signal arises from the interaction of nuclear spins with the magnetic field. Different nuclei in the sample can be distinguished by differences in their chemical shift, which is the result of the electron cloud around the nucleus shielding it from the NMR spectrometer's static magnetic field. Most often, the electron cloud is *not* symmetric and therefore the degree to which the spectrometer's magnetic field is shielded is generally orientation dependent. The magnetic field induced by the electron cloud might be in any

direction, but because of the strength of the spectrometer's magnetic field relative to the induced field, only the component parallel or antiparallel to the spectrometer's magnetic field has a non-negligable effect on the nucleus. Generally, the magnetic field induced by the electron cloud opposes the spectrometer magnetic field to some degree, hence the term chemical "shielding." The asymmetry of the electron cloud shielding around a nucleus has a fixed orientation relative to the molecular frame and is described by the chemical shift anisotropy (CSA) tensor with principle values σ_{11}, σ_{22}, and σ_{33} as shown in figure 1.7. Fast spinning of the sample can average all the orientations of a nucleus around the magic angle, which averages the chemical shielding to an average value. The chemical shift Hamiltonian is given by (106)

$$\hat{H}_{CS} = \gamma B_0 \hat{I}_Z(\sigma_{11}\sin^2\theta\cos^2\phi + \sigma_{22}\sin^2\theta\sin^2\phi + \sigma_{33}\cos^2\theta) \qquad [1.2]$$

where $\hat{H}_{CS}$ is the chemical shift Hamiltonian, γ is the gyromagnetic ratio (a constant of proportionality that relates the nucleus's angular momentum to its magnetic moment), B_0 is the static spectrometer magnetic field, $\hat{I}_Z$ is the z angular momentum operator, σ_{11}, σ_{22}, and σ_{33} are CSA tensor principle values, and θ and ϕ are the angles defined as shown in figure 1.7. In practice, because it is very difficult to determine the frequency at which a bare nucleus resonates, chemical shift values are often used (note that chemical shift values carry the opposite sign of chemical shielding values). Chemical shift values, instead of being referenced to the resonance frequency of a bare nucleus, are referenced to the resonance frequence of a reference compound, such as tetramethylsilane (TMS), which is often used as a reference for ^{13}C NMR spectra. The greek letter "σ" is used for chemical shielding and "δ" is used for chemical shift. The chemical shift Hamiltonian in terms of chemical shifts is given by (106)

$$\hat{\mathrm{H}}_{\mathrm{CS}} = -\gamma B_0 \hat{\mathrm{I}}_{\mathrm{Z}}(\delta_{11}\sin^2\theta\cos^2\phi + \delta_{22}\sin^2\theta\sin^2\phi + \delta_{33}\cos^2\theta) \quad [1.3]$$

Note that the sign of the Hamiltonian has changed. This equation can be rewritten as (106)

$$\hat{\mathrm{H}}_{\mathrm{CS}} = -\gamma B_0 \hat{\mathrm{I}}_{\mathrm{Z}}[\delta_{\mathrm{iso}} + \Delta\delta(3\cos^2\theta - 1 + \eta_{cs}\sin^2\theta\cos2\phi)] \quad [1.4]$$

where $\Delta\delta$, the chemical shift anisotropy, is defined as (106)

$$\Delta\delta = \delta_{33} - \frac{\delta_{11} + \delta_{22}}{2} \quad [1.4.1]$$

and η_{cs}, the asymmetry parameter, is defined as (106)

$$\eta_{cs} = \frac{\delta_{22} + \delta_{11}}{\delta_{33} - \delta_{iso}} \quad [1.4.2]$$

as reported in (107). In solution NMR, fast molecular tumbling will average chemical shifts to an isotropic value. Note that fast mechanical rotation of the sample about an angle of θ=54.7° will impart a time dependence to θ and ϕ that averages $\Delta\delta(3\cos^2\theta - 1 + \eta_{cs}\sin^2\theta\cos2\phi)$ to zero, leaving only isotropic chemical shift values which are the same values as the chemical shifts observed in solution NMR.

Dipolar interactions arise when one nucleus feels the magnetic field of another nucleus. The strength of the dipolar coupling depends on the distance between the two nuclei and the orientation of the internuclear vector in the magnetic field (Figure 1.8AFigure 1.7). Therefore, measurements of dipolar coupling can be used to precisely determine an unknown distance between two nuclei or the orientation of an internuclear vector in an aligned sample. In unaligned samples, any orientation of the internuclear vector is equally likely. This leasds to a very broad doublet for powder samples. In aligned samples, only a single orientation is present, which leads to a single pair of

narrow peaks with a splitting corresponding to the dipolar coupling at that orientation (Figure 1.8BFigure 1.7).

1.6 Differential scanning calorimetry

Differential scanning calorimetry (DSC) is a useful tool for studying the phase transitions of lipids. A differential scanning calorimeter measures the difference in the amount of heat required to increase the temperature of a sample and reference. These differences in heat are recorded as a function of temperature (108). Figure 1.9 shows a typical DSC spectrum observed for a water mixture of 1,2-dipalmitoleoyl-*sn*-glycero-3-phosphoethanolamine (DiPoPE), which has an L_α to H_{II} phase transition temperature (T_H) of ~ 43°C. Because the H_{II} phase of DiPoPE exhibits a great deal of negative curvature (see figure 1.2D) if a biomolecule stabilizes the H_{II} phase by reducing T_H, then it indicates that has a tendency to induce negative curvature . In contrast, if a biomolecule destabilizes the H_{II} phase by increasing T_H, then it indicates that it has a tendency to induce positive curvature (2, 109-111). In contrast, if a biomolecule destabilizes the H_{II} phase by increasing T_H, then it indicates that it has a tendency to induce positive curvature (36, 112-113).

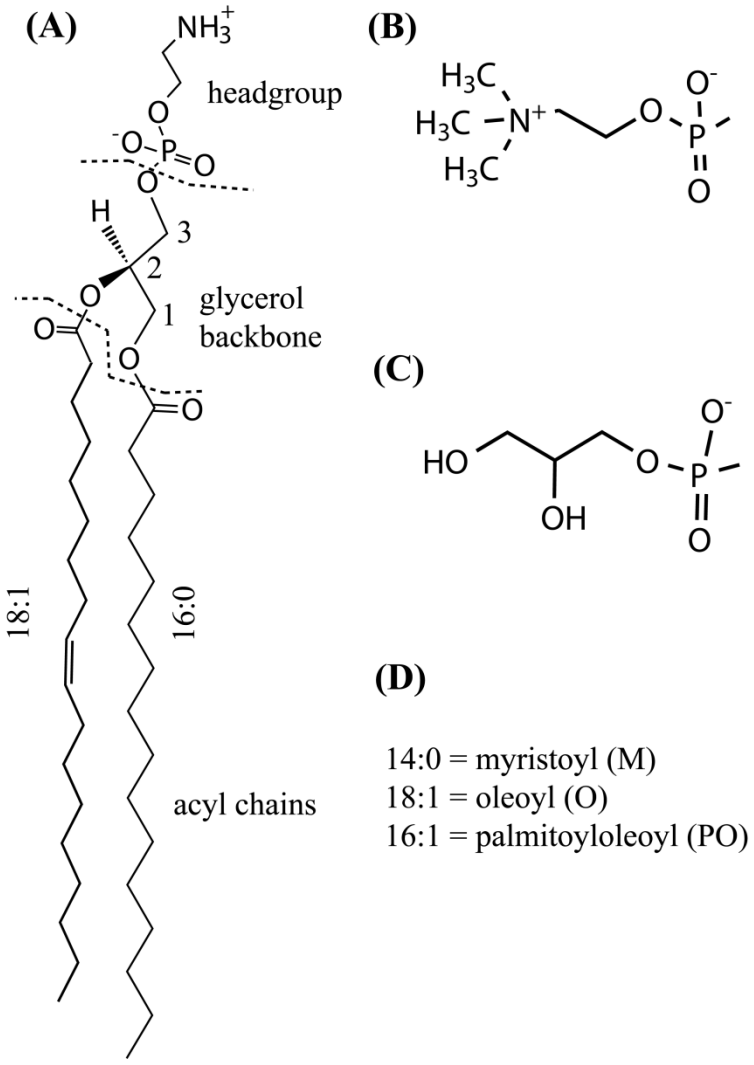

Figure 1.1 The molecular structure and nomenclature of lipids. (A) A glycerophospholipid molecule (POPE). The acyl chain, glycerol backbone, and headgroup regions indicated (dashed lines demarcate the different regions of the lipid molecule). The glycerol backbone is numbered as shown and, in this case, palmitoyl (P, 16:0) is attached at position 1, oleoyl is attached at position 2, and the headgroup (phosphatidylethanolamine or PE) is attached at position 3. Acyl chain carbon atoms are labeled starting at the carbonyl carbon, which is labeled carbon 1. Lipid names are constructed by naming the acyl chains first and then the headgroup. The molecular structures of (B) phosphatidylcholine (PC) and (C) phosphatidylglycerol headgroups. (D) The types of acyl chains used in this work and their length, number of double bonds, and abbreviations. Their length and number of double bonds is reported as length:number of double bonds.

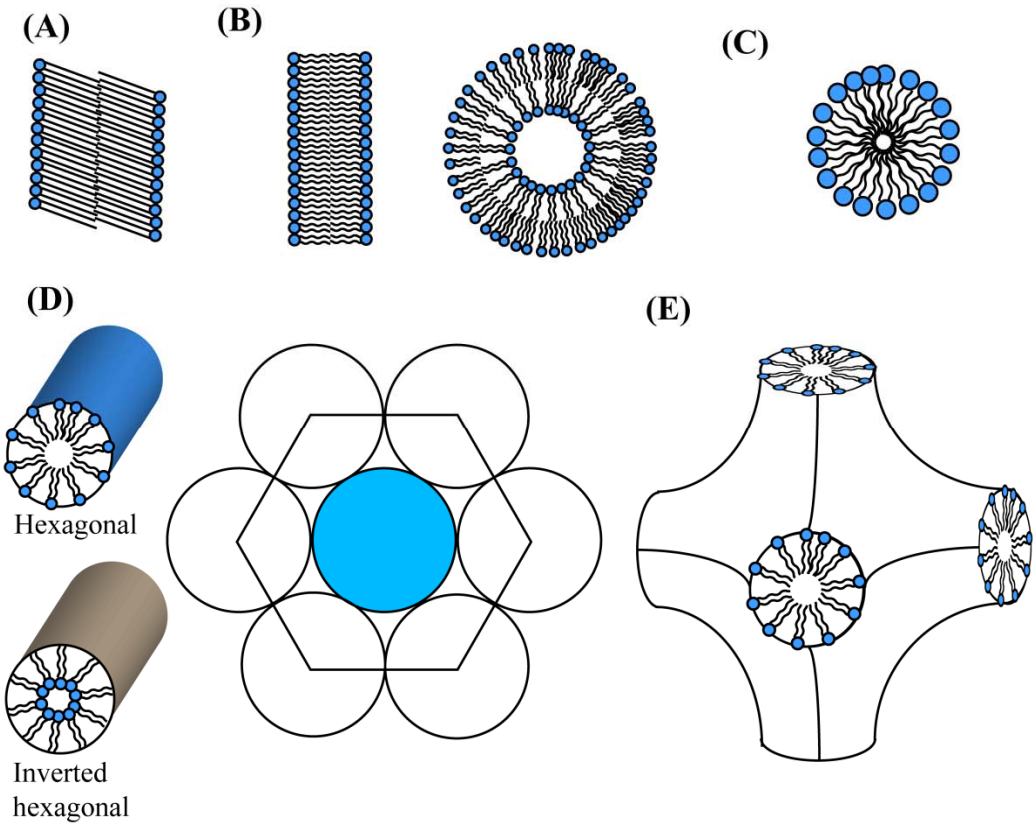

Figure 1.2 Lipid polymorphism and phase behavior. (A) The gel phase where lipid molecules are highly rigid and ordered. (B) The fluid lamellar phase. In this phase, lipids have a high degree of mobility. Lipids in this phase are described as being in a two-dimensional fluid. (C) The micelle phase, in which rapid lipid reorientation occurs. (D) On the left hand side, the normal and inverted hexagonal phases are shown. In these phases, lipid monolayers roll up into cylinders. These phases are called "hexagonal" phases because when these cylinders stack side-by-side, every lipid cylinder will be surrounded by a regular hexagon of lipid cylinders, as shown on the right side of (D). (E) The cubic phase. Fast diffusion of lipids in this phase cause them to reorient quickly on the NMR timescale.

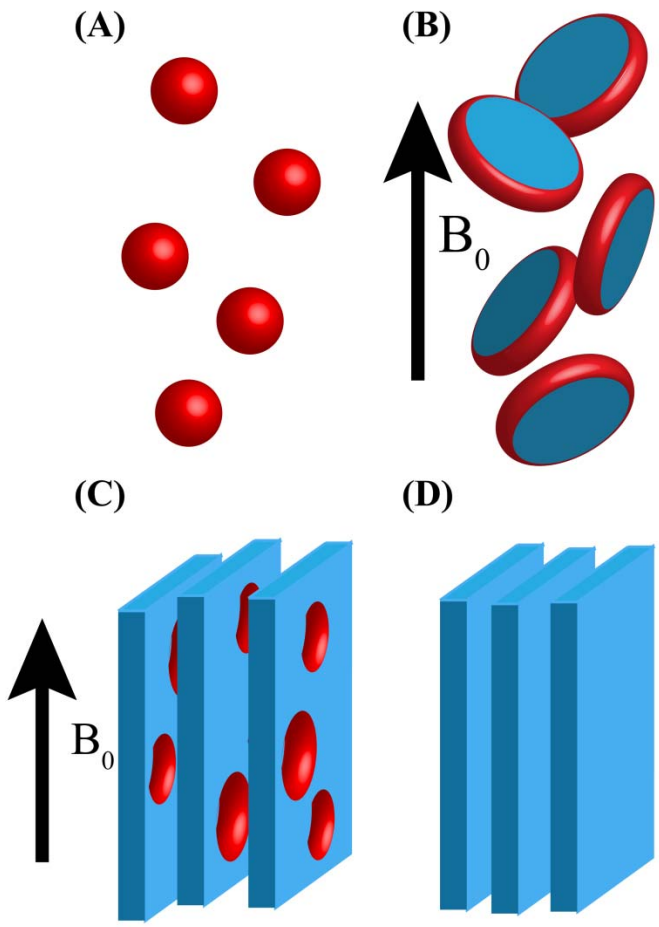

Figure 1.3 The morphologies of bicelle lipid mixtures at various Q-ratios. (A) At a Q=0, micellar structures are formed. (B) At higher Q-ratios, discoidal bicelles form. (C) When Q>3, perforated lamellar sheets that resemble slices of swiss cheese are likely to form. Depending on the specific lipids used in the bicelle mixture, other morphologies are also possible, such as a nematic phase DMPC-rich ribbons with DHPC around the edges (32). (D) At infinite Q-ratio, a lamellar phase is observed and multilamellar vesicles (MLVs) typically form.

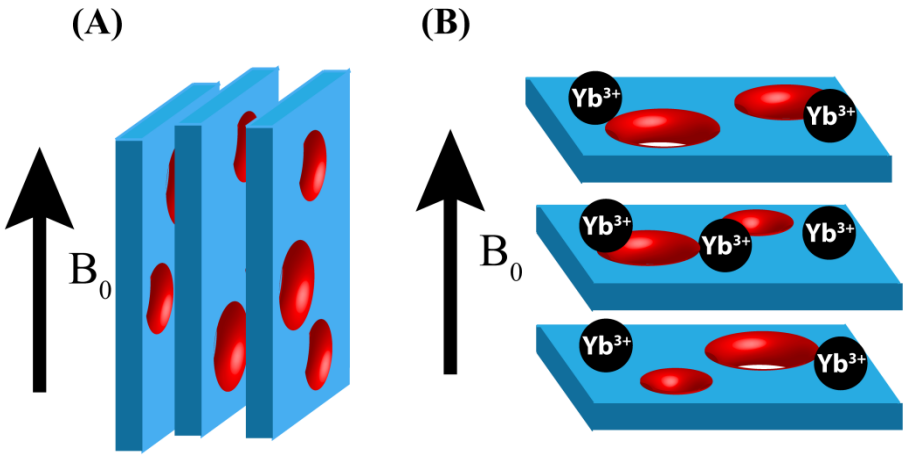

Figure 1.4 Certain trivalent lanthanide cations may be used to reorient bicelles. (A) In the absence of trivalent lanthanide cations bicelles are naturally negatively aligned, with their bicelle bilayer normal is perpendicular to the magnetic field. (B) The addition of trivalent lanthanide cations reorients the bicelles, so that their bicelle bilayer normal is parallel to the magnetic field. These lanthanide doped bicelles are also referred to as positively aligned bicelles.

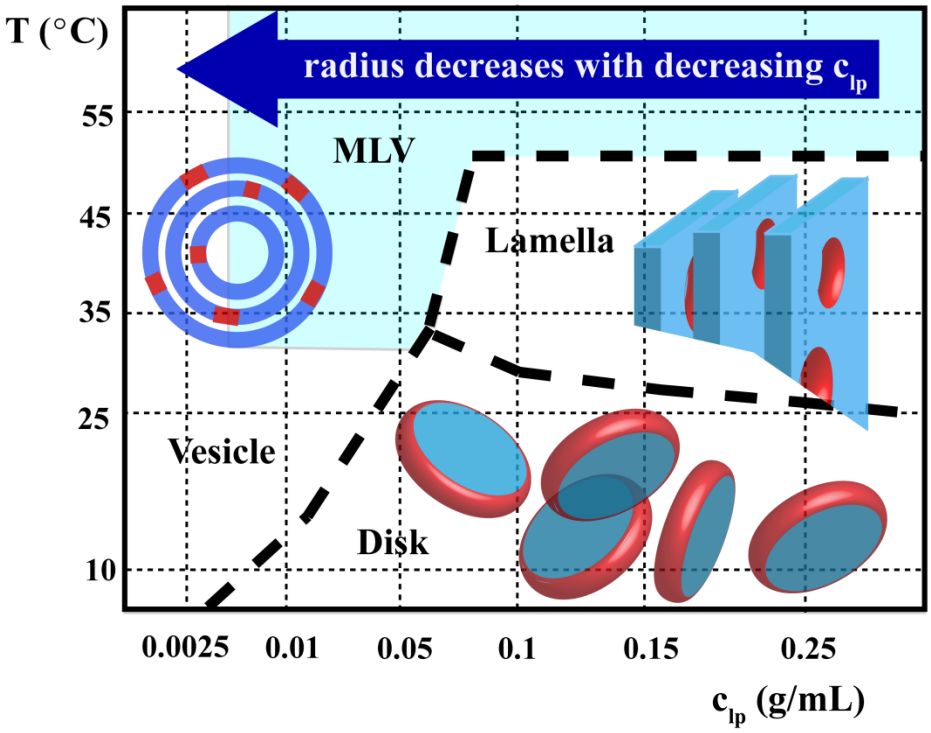

Figure 1.5 A phase diagram for negatively aligned bicelles. The phase diagram of DMPC/DHPC bicelles at a *q*-ratio of 3.2 and at various temperatures and concentrations of lipid (c_{lp}). Adapted from (33).

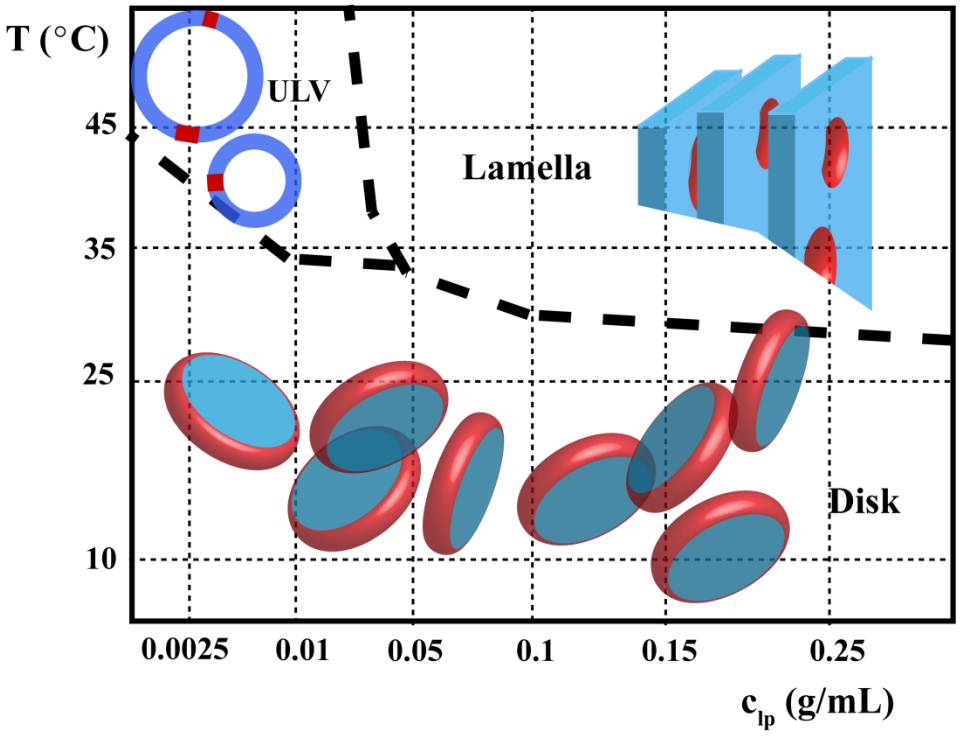

Figure 1.6 A phase diagram for positively aligned bicelles. The phase diagram of DMPC/DMPG/DHPC bicelles at a *q*-ratio of 3.4 with molar ratios of DMPC/DMPG/DHPC/Tm^{3+} at molar ratios of 3.2/0.21/1.0/0.043, respectively, and at various temperatures and concentrations of lipid (c_{lp}). Unilamellar vesicles is abbreviated as ULV. Adapted from (33).

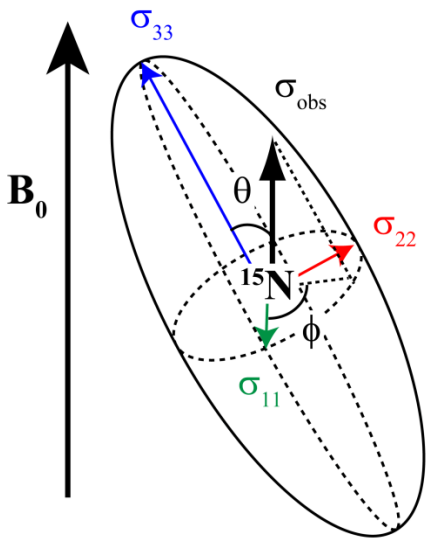

Figure 1.7 Chemical shift anisotropy. The chemical shift anisotropy (CSA) tensor describes the orientational dependence and degree of shielding around a particular nucleus.

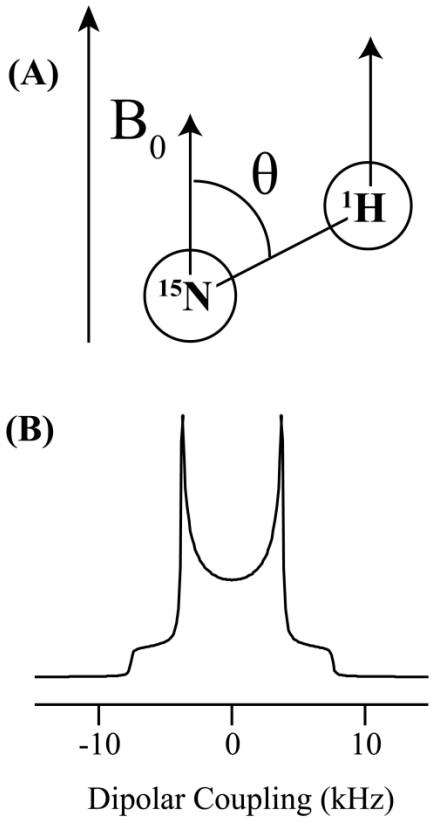

Figure 1.8 The dipolar coupling interaction. (A) The strength of the dipolar coupling between two NMR-active nuclei depends on the orientation of the vector connecting the two nuclear spins relative to the magnetic field. (B) In unaligned NMR samples, where all orientations are equally likely, a Pake doublet powder pattern results, where all possible values of dipolar coupling contribute to the spectrum.

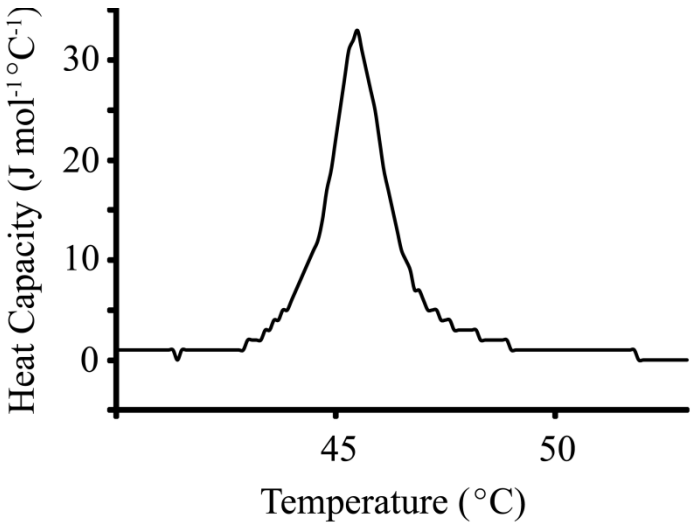

Figure 1.9 A differential scanning calorimetry scan of pure dipalmitoylphosphatidylethanolamine.

1.7 References

1. Jo, E., J. McLaurin, C. M. Yip, P. St. George-Hyslop, and P. E. Fraser. 2000. α-Synuclein Membrane Interactions and Lipid Specificity. J. Biol. Chem. 275:34328-34334.

2. Smith, P. E. S., J. R. Brender, and A. Ramamoorthy. 2009. Induction of Negative Curvature as a Mechanism of Cell Toxicity by Amyloidogenic Peptides: The Case of Islet Amyloid Polypeptide. J. Am. Chem. Soc. 131:4470-4478.

3. Relini, A., O. Cavalleri, R. Rolandi, and A. Gliozzi. 2009. The two-fold aspect of the interplay of amyloidogenic proteins with lipid membranes. Chem. Phys. Lipids 158:1-9.

4. Zhu, M., P. O. Souillac, C. Ionescu-Zanetti, S. A. Carter, and A. L. Fink. 2002. Surface-catalyzed Amyloid Fibril Formation. J. Biol. Chem. 277:50914-50922.

5. Ambroggio, E. E., D. H. Kim, F. Separovic, C. J. Barrow, K. J. Barnham, L. A. Bagatolli, and G. D. Fidelio. 2005. Surface Behavior and Lipid Interaction of Alzheimer β-Amyloid Peptide 1-42: A Membrane-Disrupting Peptide. Biophys. J. 88:2706-2713.

6. Andersen, O. S., and R. E. Koeppe. 2007. Bilayer Thickness and Membrane Protein Function: An Energetic Perspective. Annu. Rev. Biophys. Biomol. Struct. 36:107-130.

7. Marsh, D. 2008. Protein modulation of lipids, and vice-versa, in membranes. Biochim. Biophys. Acta 1778:1545-1575.

8. Phillips, R., T. Ursell, P. Wiggins, and P. Sens. 2009. Emerging roles for lipids in shaping membrane-protein function. Nature 459:379-385.

9. Barry, J., M. Fritz, J. R. Brender, P. E. S. Smith, D.-K. Lee, and A. Ramamoorthy. 2009. Determining the Effects of Lipophilic Drugs on Membrane Structure by Solid-State NMR Spectroscopy: The Case of the Antioxidant Curcumin. J. Am. Chem. Soc. 131:4490-4498.

10. Ingolfsson, H. I., R. E. Koeppe, and O. S. Andersen. 2007. Curcumin is a Modulator of Bilayer Material Properties. Biochemistry 46:10384-10391.

11. Sukharev, S. I., W. J. Sigurdson, C. Kung, and F. Sachs. 1999. Energetic and Spatial Parameters for Gating of the Bacterial Large Conductance Mechanosensitive Channel, MscL. J. Gen. Physiol. 113:525-540.

12. Moe, P., and P. Blount. 2005. Assessment of Potential Stimuli for Mechano-Dependent Gating of MscL: Effects of Pressure, Tension, and Lipid Headgroups. Biochemistry 44:12239-12244.

13. Suchyna, T. M., S. E. Tape, R. E. Koeppe, O. S. Andersen, F. Sachs, and P. A. Gottlieb. 2004. Bilayer-dependent inhibition of mechanosensitive channels by neuroactive peptide enantiomers. Nature 430:235-240.

14. Yeagle, P. L. 1993. The Membranes of Cells. Academic Press, San Diego.

15. Jayasinghe, S. A., and R. Langen. 2005. Lipid Membranes Modulate the Structure of Islet Amyloid Polypeptide. Biochemistry 44:12113-12119.

16. Marsh, D. 1990. CRC Handbook of Lipid Bilayers. CRC Press, Ann Arbor, MI.

17. Nagle, J. F., and S. Tristram-Nagle. 2000. Structure of lipid bilayers. Biochim. Biophys. Acta 1469:159-195.

18. Zimmerberg, J., and M. M. Kozlov. 2006. How proteins produce cellular membrane curvature. Nat. Rev. Mol. Cell Biol. 7:9-19.

19. Cullis, P. R., and B. Dekruijff. 1979. Lipid Polymorphism and the Functional Roles of Lipids in Biological Membranes. Biochim. Biophys. Acta 559:399-420.

20. Gruner, S. M. 1985. Intrinsic Curvature Hypothesis for Biomembrane Lipid Composition: A Role for Nonbilayer Lipids. Proc. Natl. Acad. Sci. USA 82:3665-3669.

21. Janes, N. 1996. Curvature stress and polymorphism in membranes. Chem. Phys. Lipids 81:133-150.

22. Sanders, C. R., B. J. Hare, K. P. Howard, and J. H. Prestegard. 1994. Magnetically-oriented phospholipid micelles as a tool for the study of membrane-associated molecules. Prog. Nucl. Mag. Res. Sp. 26:421-444.

23. Park, S. H., S. Prytulla, A. A. De Angelis, J. M. Brown, H. Kiefer, and S. J. Opella. 2006. High-Resolution NMR Spectroscopy of a GPCR in Aligned Bicelles. J. Am. Chem. Soc. 128:7402-7403.

24. Park, S. H., A. A. De Angelis, A. A. Nevzorov, C. H. Wu, and S. J. Opella. 2006. Three-Dimensional Structure of the Transmembrane Domain of Vpu from HIV-1 in Aligned Phospholipid Bicelles. Biophys. J. 91:3032-3042.

25. Sanders, C. R., and J. P. Schwonek. 1992. Characterization of magnetically orientable bilayers in mixtures of dihexanoylphosphatidylcholine and dimyristoylphosphatidylcholine by solid-state NMR. Biochemistry 31:8898-8905.

26. Sanders, C. R., and R. S. Prosser. 1998. Bicelles: a model membrane system for all seasons? Structure 6:1227-1234.

27. Nieh, M.-P., C. J. Glinka, S. Krueger, R. S. Prosser, and J. Katsaras. 2001. SANS Study of the Structural Phases of Magnetically Alignable Lanthanide-Doped Phospholipid Mixtures. Langmuir 17:2629-2638.

28. Yamamoto, K., R. Soong, and A. Ramamoorthy. 2009. Comprehensive Analysis of Lipid Dynamics Variation with Lipid Composition and Hydration of Bicelles Using Nuclear Magnetic Resonance (NMR) Spectroscopy. Langmuir 25:7010-7018.

29. Prosser, R. S., V. B. Volkov, and I. V. Shiyanovskaya. 1998. Solid-state NMR studies of magnetically aligned phospholipid membranes: Taming lanthanides for membrane protein studies. Biochem. Cell Biol. 76:443-451.

30. Prosser, R. S., V. B. Volkov, and I. V. Shiyanovskaya. 1998. Novel Chelate-Induced Magnetic Alignment of Biological Membranes. Biophys. J. 75:2163-2169.

31. Prosser, R. S., J. S. Hwang, and R. R. Vold. 1998. Magnetically Aligned Phospholipid Bilayers with Positive Ordering: A New Model Membrane System. Biophys. J. 74:2405-2418.

32. Vold, R. R., and R. S. Prosser. 1996. Magnetically Oriented Phospholipid Bilayered Micelles for Structural Studies of Polypeptides. Does the Ideal Bicelle Exist? J. Magn. Reson. B 113:267-271.

33. Nieh, M.-P., C. J. Glinka, S. Krueger, R. S. Prosser, and J. Katsaras. 2002. SANS Study on the Effect of Lanthanide Ions and Charged Lipids on the Morphology of Phospholipid Mixtures. Biophys. J. 82:2487-2498.

34. Nieh, M.-P., V. A. Raghunathan, C. J. Glinka, T. A. Harroun, G. Pabst, and J. Katsaras. 2004. Magnetically Alignable Phase of Phospholipid "Bicelle" Mixtures Is a Chiral Nematic Made Up of Wormlike Micelles. Langmuir 20:7893-7897.

35. Ramamoorthy, A., S. Thennarasu, D.-K. Lee, A. Tan, and L. Maloy. 2006. Solid-State NMR Investigation of the Membrane-Disrupting Mechanism of Antimicrobial Peptides MSI-78 and MSI-594 Derived from Magainin 2 and Melittin. Biophys. J. 91:206-216.

36. Hallock, K. J., D.-K. Lee, and A. Ramamoorthy. 2003. MSI-78, an Analogue of the Magainin Antimicrobial Peptides, Disrupts Lipid Bilayer Structure via Positive Curvature Strain. Biophys. J. 84:3052-3060.

37. Henzler Wildman, K. A., D.-K. Lee, and A. Ramamoorthy. 2003. Mechanism of Lipid Bilayer Disruption by the Human Antimicrobial Peptide, LL-37. Biochemistry 42:6545-6558.

38. Cooper, G. J., A. C. Willis, A. Clark, R. C. Turner, R. B. Sim, and K. B. Reid. 1987. Purification and characterization of a peptide from amyloid-rich pancreases of type 2 diabetic patients. Proc. Natl. Acad. Sci. USA 84:8628-8632.

39. Westermark, P., C. Wernstedt, T. O'Brien, D. Hayden, and K. Johnson. 1987. Islet amyloid in type 2 human diabetes mellitus and adult diabetic cats contains a novel putative polypeptide hormone. Am. J. Pathol. 127:414-417.

40. Butler, P. C., J. Chou, W. B. Carter, Y. N. Wang, B. H. Bu, D. Chang, J. K. Chang, and R. A. Rizza. 1990. Effects of meal ingestion on plasma amylin concentration in NIDDM and nondiabetic humans. Diabetes 39:752-756.

41. Kahn, S. E., D. A. D'Alessio, M. W. Schwartz, W. Y. Fujimoto, J. W. Ensinck, G. J. Taborsky, and D. Porte. 1990. Evidence of cosecretion of islet amyloid polypeptide and insulin by beta-cells. Diabetes 39:634-638.

42. Leffert, J. D., C. B. Newgard, H. Okamoto, J. L. Milburn, and K. L. Luskey. 1989. Rat amylin: cloning and tissue-specific expression in pancreatic islets. Proc. Natl. Acad. Sci. USA 86:3127-3130.

43. Kayed, R., Y. Sokolov, B. Edmonds, T. M. McIntire, S. C. Milton, J. E. Hall, and C. G. Glabe. 2004. Permeabilization of Lipid Bilayers Is a Common Conformation-dependent Activity of Soluble Amyloid Oligomers in Protein Misfolding Diseases. J. Biol. Chem. 279:46363-46366.

44. Mirzabekov, T. A., M.-c. Lin, and B. L. Kagan. 1996. Pore Formation by the Cytotoxic Islet Amyloid Peptide Amylin. J. Biol. Chem. 271:1988-1992.

45. Demuro, A., E. Mina, R. Kayed, S. C. Milton, I. Parker, and C. G. Glabe. 2005. Calcium Dysregulation and Membrane Disruption as a Ubiquitous Neurotoxic Mechanism of Soluble Amyloid Oligomers. J. Biol. Chem. 280:17294-17300.

46. Mattson, M. P., and S. L. Chan. 2003. Calcium orchestrates apoptosis. Nat. Cell Biol. 5:1041-1043.

47. Mattson, M. P., and Y. Goodman. 1995. Different amyloidogenic peptides share a similar mechanism of neurotoxicity involving reactive oxygen species and calcium. Brain Res. 676:219-224.

48. Lastra, G., and C. Manrique. 2007. The Expanding Role of Oxidative Stress, Renin Angiotensin System, and β-Cell Dysfunction in the Cardiometabolic Syndrome and Type 2 Diabetes Mellitus. Antioxid. Redox Sig. 9:943-954.

49. Ritzel, R. A., J. J. Meier, C.-Y. Lin, J. D. Veldhuis, and P. C. Butler. 2007. Human Islet Amyloid Polypeptide Oligomers Disrupt Cell Coupling, Induce Apoptosis, and Impair Insulin Secretion in Isolated Human Islets. Diabetes 56:65-71.

50. Chen, S., V. Berthelier, J. B. Hamilton, B. O'Nuallai, and R. Wetzel. 2002. Amyloid-like Features of Polyglutamine Aggregates and Their Assembly Kinetics. Biochemistry 41:7391-7399.

51. Hardy, J., and D. J. Selkoe. 2002. The Amyloid Hypothesis of Alzheimer's Disease: Progress and Problems on the Road to Therapeutics. Science 297:353-356.

52. Tanzi, R. E., and L. Bertram. 2005. Twenty Years of the Alzheimer s Disease Amyloid Hypothesis: A Genetic Perspective. Cell 120:545-555.

53. Gotz, J., J. R. Streffer, D. David, A. Schild, F. Hoerndli, L. Pennanen, P. Kurosinski, and F. Chen. 2004. Transgenic animal models of Alzheimer's disease and related disorders: histopathology, behavior and therapy. Mol. Psychiatry 9:664-683.

54. Chartier-Harlin, M.-C., F. Crawford, H. Houlden, A. Warren, D. Hughes, L. Fidani, A. Goate, M. Rossor, P. Roques, J. Hardy, and M. Mullan. 1991. Early-onset Alzheimer's disease caused by mutations at codon 717 of the [beta]-amyloid precursor protein gene. Nature 353:844-846.

55. Simoneau, S., H. Rezaei, N. Salès, G. Kaiser-Schulz, M. Lefebvre-Roque, C. Vidal, J.-G. Fournier, J. Comte, F. Wopfner, J. Grosclaude, H. Schätzl, and C. I. Lasmézas. 2007. In Vitro and In Vivo Neurotoxicity of Prion Protein Oligomers. PLoS Pathog. 3:e125.

56. Wootz, H., I. Hansson, L. Korhonen, U. Näpänkangas, and D. Lindholm. 2004. Caspase-12 cleavage and increased oxidative stress during motoneuron degeneration in transgenic mouse model of ALS. Biochem. Biophys. Res. Commun. 322:281-286.

57. Ryu, E. J., H. P. Harding, J. M. Angelastro, O. V. Vitolo, D. Ron, and L. A. Greene. 2002. Endoplasmic Reticulum Stress and the Unfolded Protein Response in Cellular Models of Parkinson's Disease. J. Neurosci. 22:10690-10698.

58. Imai, Y., M. Soda, H. Inoue, N. Hattori, Y. Mizuno, and R. Takahashi. 2001. An Unfolded Putative Transmembrane Polypeptide, which Can Lead to Endoplasmic Reticulum Stress, Is a Substrate of Parkin. Cell 105:891-902.

59. Wisniewski, T., J. Ghiso, and B. Frangione. 1991. Peptides homologous to the amyloid protein of Alzheimer's disease containing a glutamine for glutamic acid substitution have accelerated amyloid fibril formation. Biochem. Biophys. Res. Commun. 179:1247-1254.

60. Scheuner, D., C. Eckman, M. Jensen, X. Song, M. Citron, N. Suzuki, T. D. Bird, J. Hardy, M. Hutton, W. Kukull, E. Larson, L. Levy-Lahad, M. Viitanen, E. Peskind, P. Poorkaj, G. Schellenberg, R. Tanzi, W. Wasco, L. Lannfelt, D. Selkoe, and S. Younkin. 1996. Secreted amyloid β-protein similar to that in the

senile plaques of Alzheimer's disease is increased in vivo by the presenilin 1 and 2 and APP mutations linked to familial Alzheimer's disease. Nat. Med. 2:864-870.

61. Wavrant-DeVrièze, F., J.-C. Lambert, L. Stas, R. Crook, D. Cottel, F. Pasquier, B. Frigard, M. Lambrechts, E. Thiry, P. Amouyel, J. Pérez-Tur, M. C. Chartier-Harlin, J. Hardy, and F. Van Leuven. 1999. Association between coding variability in the LRP gene and the risk of late-onset Alzheimer's disease. Hum. Genet. 104:432-434.

62. Myers, A., P. Holmans, H. Marshall, J. Kwon, D. Meyer, D. Ramic, S. Shears, J. Booth, F. W. DeVrieze, R. Crook, M. Hamshere, R. Abraham, N. Tunstall, F. Rice, S. Carty, S. Lillystone, P. Kehoe, V. Rudrasingham, L. Jones, S. Lovestone, J. Perez-Tur, J. Williams, M. J. Owen, J. Hardy, and A. M. Goate. 2000. Susceptibility Locus for Alzheimer's Disease on Chromosome 10. Science 290:2304-2305.

63. Ertekin-Taner, N., N. Graff-Radford, L. H. Younkin, C. Eckman, M. Baker, J. Adamson, J. Ronald, J. Blangero, M. Hutton, and S. G. Younkin. 2000. Linkage of Plasma Aβ42 to a Quantitative Locus on Chromosome 10 in Late-Onset Alzheimer's Disease Pedigrees. Science 290:2303-2304.

64. Bertram, L., D. Blacker, K. Mullin, D. Keeney, J. Jones, S. Basu, S. Yhu, M. G. McInnis, R. C. P. Go, K. Vekrellis, D. J. Selkoe, A. J. Saunders, and R. E. Tanzi. 2000. Evidence for Genetic Linkage of Alzheimer's Disease to Chromosome 10q. Science 290:2302-2303.

65. Olson, J. M., K. A. B. Goddard, and D. M. Dudek. 2001. The Amyloid Precursor Protein Locus and Very-Late-Onset Alzheimer Disease. Am. J. Hum. Genet. 69:895-899.

66. Clark, A., and M. R. Nilsson. 2004. Islet amyloid: a complication of islet dysfunction or an aetiological factor in Type 2 diabetes? Diabetologia 47:157-169.

67. Westermark, P. 1976. The Nature of Amyloid in Islets of Langerhans in Old Age. Academic Press, New York.

68. Westermark, P. 1973. Fine structure of islets of Langerhans in insular amyloidosis. Virchows Archiv. A Pathol. Anat. 359:1-18.

69. Jayasinghe, S. A., and R. Langen. 2007. Membrane interaction of islet amyloid polypeptide. Biochim. Biophys. Acta 1768:2002-2009.

70. Janson, J., R. H. Ashley, D. Harrison, S. McIntyre, and P. C. Butler. 1999. The mechanism of islet amyloid polypeptide toxicity is membrane disruption by intermediate-sized toxic amyloid particles. Diabetes 48:491-498.

71. Kawahara, M., Y. Kuroda, N. Arispe, and E. Rojas. 2000. Alzheimer's β-Amyloid, Human Islet Amylin, and Prion Protein Fragment Evoke Intracellular Free Calcium Elevations by a Common Mechanism in a Hypothalamic GnRH Neuronal Cell Line. J. Biol. Chem. 275:14077-14083.

72. Engel, M. F. M., L. Khemtémourian, C. C. Kleijer, H. J. D. Meeldijk, J. Jacobs, A. J. Verkleij, B. de Kruijff, J. A. Killian, and J. W. M. Höppener. 2008. Membrane damage by human islet amyloid polypeptide through fibril growth at the membrane. Proc. Natl. Acad. Sci. USA 105:6033-6038.

73. Brender, J. R., E. L. Lee, M. A. Cavitt, A. Gafni, D. G. Steel, and A. Ramamoorthy. 2008. Amyloid Fiber Formation and Membrane Disruption are Separate Processes Localized in Two Distinct Regions of IAPP, the Type-2-Diabetes-Related Peptide. J. Am. Chem. Soc. 130:6424-6429.

74. Esfand, R., and D. A. Tomalia. 2001. Poly(amidoamine) (PAMAM) dendrimers: from biomimicry to drug delivery and biomedical applications. Drug Discov. Today 6:427-436.

75. Langer, R. 1998. Drug Delivery and Targeting. Nature 392:5-10.

76. Quintana, A., E. Raczka, L. Piehler, I. Lee, A. Myc, I. Majoros, A. Patri, T. Thomas, J. Mulé, and J. Baker. 2002. Design and Function of a Dendrimer-Based Therapeutic Nanodevice Targeted to Tumor Cells Through the Folate Receptor. Pharm. Res. 19:1310-1316.

77. Kukowska-Latallo, J. F., K. A. Candido, Z. Cao, S. S. Nigavekar, I. J. Majoros, T. P. Thomas, L. P. Balogh, M. K. Khan, and J. R. Baker, Jr. 2005. Nanoparticle Targeting of Anticancer Drug Improves Therapeutic Response in Animal Model of Human Epithelial Cancer. Cancer Res. 65:5317-5324.

78. Shiota, M., Y. Ikeda, Z. Kaul, J. Itadani, S. C. Kaul, and R. Wadhwa. 2007. Internalizing Antibody-Based Targeted Gene Delivery for Human Cancer Cells. Hum. Gene Ther. 65:5317-5324.

79. Parveen, S., and S. K. Sahoo. 2008. Polymeric nanoparticles for cancer therapy. J. Drug Targeting 16:108-123.

80. Braun, C. S., J. A. Vetro, D. A. Tomalia, G. S. Koe, J. G. Koe, and C. R. Middaugh. 2005. Structure/function relationships of polyamidoamine/DNA dendrimers as gene delivery vehicles. J. Pharm. Sci. 94:423-436.

81. Zhang, Z.-Y., and B. D. Smith. 2000. High-Generation Polycationic Dendrimers Are Unusually Effective at Disrupting Anionic Vesicles: Membrane Bending Model. Bioconjugate Chem. 11:805-814.

82. Zhang, S., B. Zhao, H. Jiang, B. Wang, and B. Ma. 2007. Cationic lipids and polymers mediated vectors for delivery of siRNA. J. Controlled Release 123:1-10.

83. Fischer, D., Y. Li, B. Ahlemeyer, J. Krieglstein, and T. Kissel. 2003. In vitro cytotoxicity testing of polycations: influence of polymer structure on cell viability and hemolysis. Biomaterials 24:1121-1131.

84. Maynard, A. D., R. J. Aitken, T. Butz, V. Colvin, K. Donaldson, G. Oberdörster, M. A. Philbert, J. Ryan, A. Seaton, V. Stone, S. S. Tinkle, L. Tran, N. J. Walker, and D. B. Warheit. 2006. Safe handling of nanotechnology. Nature 444:267-269.

85. Oberdörster, G., E. Oberdörster, and J. Oberdörster. 2005. Nanotoxicology: An Emerging Discipline Evolving from Studies of Ultrafine Particles. Environ. Health Perspect. 113:823-839.

86. Leroueil, P. R., S. A. Berry, K. Duthie, G. Han, V. M. Rotello, D. Q. McNerny, J. R. Baker, B. G. Orr, and M. M. Banaszak Holl. 2008. Wide Varieties of Cationic Nanoparticles Induce Defects in Supported Lipid Bilayers. Nano Lett. 8:420-424.

87. Leroueil, P. R., S. Hong, A. Mecke, J. R. Baker, B. G. Orr, and M. M. Banaszak Holl. 2007. Nanoparticle Interaction with Biological Membranes: Does Nanotechnology Present a Janus Face? Acc. Chem. Res. 40:335-342.

88. Hong, S., P. R. Leroueil, E. K. Janus, J. L. Peters, M.-M. Kober, M. T. Islam, B. G. Orr, J. R. Baker, and M. M. Banaszak Holl. 2006. Interaction of Polycationic Polymers with Supported Lipid Bilayers and Cells: Nanoscale Hole Formation and Enhanced Membrane Permeability. Bioconjugate Chem. 17:728-734.

89. Hong, S., A. U. Bielinska, A. Mecke, B. Keszler, J. L. Beals, X. Shi, L. Balogh, B. G. Orr, J. R. Baker, and M. M. Banaszak Holl. 2004. Interaction of Poly(amidoamine) Dendrimers with Supported Lipid Bilayers and Cells: Hole Formation and the Relation to Transport. Bioconjugate Chem. 15:774-782.

90. Monteiro-Riviere, N. A., R. J. Nemanich, A. O. Inman, Y. Y. Wang, and J. E. Riviere. 2005. Multi-walled carbon nanotube interactions with human epidermal keratinocytes. Toxicol. Lett. 155:377-384.

91. Oberdörster, E. 2004. Manufactured Nanomaterials (Fullerenes, C-60) Induce Oxidative Stress in the Brain of Juvenile Largemouth Bass. Environ. Health Perspect. 112:1058-1062.

92. Tinkle, S. S., J. M. Antonini, B. A. Rich, J. R. Roberts, R. Salmen, K. DePree, and E. J. Adkins. 2003. Skin as a Route of Exposure and Sensitization in Chronic Beryllium Disease. Environ. Health Perspect. 111:1202-1208.

93. Oberdörster, G., R. M. Celein, J. Ferin, and B. Weiss. 1995. Association of Particulate Air Pollution and Acute Mortality: Involvement of Ultrafine Particles? Inhalation Toxic. 7:111-124.

94. El-Sayed, M., M. Ginski, C. Rhodes, and H. Ghandehari. 2002. Transepithelial transport of poly(amidoamine) dendrimers across Caco-2 cell monolayers. J. Controlled Release 81:355-365.

95. Brender, J. R., U. H. N. Dürr, D. Heyl, M. B. Budarapu, and A. Ramamoorthy. 2007. Membrane fragmentation by an amyloidogenic fragment of human Islet Amyloid Polypeptide detected by solid-state NMR spectroscopy of membrane nanotubes. Biochim. Biophys. Acta 1768:2026-2029.

96. Park, S. H., A. A. Mrse, A. A. Nevzorov, M. F. Mesleh, M. Oblatt-Montal, M. Montal, and S. J. Opella. 2003. Three-dimensional Structure of the Channel-forming Trans-membrane Domain of Virus Protein "u" (Vpu) from HIV-1. J. Mol. Biol. 333:409-424.

97. Dürr, U. H. N., K. Yamamoto, S.-C. Im, L. Waskell, and A. Ramamoorthy. 2007. Solid-State NMR Reveals Structural and Dynamical Properties of a Membrane-Anchored Electron-Carrier Protein, Cytochrome b5. J. Am. Chem. Soc. 129:6670-6671.

98. Bechinger, B. 1999. The structure, dynamics and orientation of antimicrobial peptides in membranes by multidimensional solid-state NMR spectroscopy. Biochim. Biophys. Acta 1462:157-183.

99. Davis, J. H., and M. Auger. 1999. Static and magic angle spinning NMR of membrane peptides and proteins. Prog. Nucl. Mag. Res. Sp. 35:1-84.

100. Fu, R. Q., and T. A. Cross. 1999. Solid-state nuclear magnetic resonance investigation of protein and polypeptide structure. Annu. Rev. Biophys. Biomolec. Struct. 28:235-268.

101. Marassi, F. M., and S. J. Opella. 1998. NMR structural studies of membrane proteins. Curr. Opin. Struct. Biol. 8:640-648.

102. Watts, A. 1998. Solid-state NMR approaches for studying the interaction of peptides and proteins with membranes. Biochim. Biophys. Acta 1376:297-318.

103. Cross, T. A., and S. J. Opella. 1994. Solid-State NMR Structural Studies of Peptides and Proteins in Membranes. Curr. Opin. Struct. Biol. 4:574-581.

104. Warschawski, D. E., M. Traikia, P. F. Devaux, and G. Bodenhausen. 1998. Solid-state NMR for the study of membrane systems: The use of anisotropic interactions. Biochimie 80:437-450.

105. Bechinger, B. 2000. Biophysical investigations of membrane perturbations by polypeptides using solid-state NMR spectroscopy (review). Mol. Membr. Biol. 17:135-142.

106. Abragam, A. 1978. Principles of Nuclear Magnetism. Claredon Press, Oxford.

107. Mason, J. 1993. Conventions for the reporting of nuclear magnetic shielding (or shift) tensors suggested by participants in the NATO ARW on NMR shielding constants at the University of Maryland, College Park, July 1992. Solid State Nucl. Mag. 2:285-288.

108. Cooper, A., and C. M. Johnson. 1994. Introduction to Microcalorimetry and Biomolecular Energetics. In Methods in Molecular Biology. C. Jones, B. Mulloy, and A. H. Thomas, editors. Humana Press, Totawa, N.J.

109. Powers, J.-P. S., A. Tan, A. Ramamoorthy, and R. E. W. Hancock. 2005. Solution Structure and Interaction of the Antimicrobial Polyphemusins with Lipid Membranes. Biochemistry 44:15504-15513.

110. Davies, S. M. A., R. F. Epand, J. P. Bradshaw, and R. M. Epand. 1998. Modulation of Lipid Polymorphism by the Feline Leukemia Virus Fusion Peptide: Implications for the Fusion Mechanism. Biochemistry 37:5720-5729.

111. Koulov, A. V., L. Vares, M. Jain, and B. D. Smith. 2002. Cationic triple-chain amphiphiles facilitate vesicle fusion compared to double-chain or single-chain analogues. Biochim. Biophys. Acta 1564:459-465.

112. Alves, I. D., N. Goasdoué, I. Correia, S. Aubry, C. Galanth, S. Sagan, S. Lavielle, and G. Chassaing. 2008. Membrane interaction and perturbation mechanisms induced by two cationic cell penetrating peptides with distinct charge distribution. Biochim. Biophys. Acta 1780:948-959.

113. Tytler, E. M., J. P. Segrest, R. M. Epand, S. Q. Nie, R. F. Epand, V. K. Mishra, Y. V. Venkatachalapathi, and G. M. Anantharamaiah. 1993. Reciprocal effects of apolipoprotein and lytic peptide analogs on membranes. Cross-sectional molecular shapes of amphipathic alpha helixes control membrane stability. J. Biol. Chem. 268:22112-22118.

CHAPTER 2

ISLET AMYLOID POLYPEPTIDE DISRUPTS CELL MEMBRANES BY A CURVATURE INDUCTION MECHANISM*

2.1 Summary

The death of insulin-producing β-cells is a key step in the pathogenesis of type 2 diabetes. The amyloidogenic peptide Islet Amyloid Polypeptide (IAPP, also known as amylin) has been shown to disrupt β-cell membranes leading to β-cell death. Despite the strong evidence linking IAPP to the destruction of β-cell membrane integrity and cell death, the mechanism of IAPP toxicity is poorly understood. In particular, the effect of IAPP on the bilayer structure has largely been uncharacterized. In this study, we have determined the effect of the amyloidogenic and toxic $hIAPP_{1-37}$ peptide and the non-toxic and non-amyloidogenic $rIAPP_{1-37}$ peptide on membranes by a combination of DSC and solid-state NMR spectroscopy. We also characterized the toxic but largely non-amyloidogenic $rIAPP_{1-19}$ and $hIAPP_{1-19}$ fragments. DSC shows that both amyloidogenic ($hIAPP_{1-37}$) and largely non-amyloidogenic toxic versions of the peptide ($hIAPP_{1-19}$ and $rIAPP_{1-19}$) strongly favor the formation of negative curvature in lipid bilayers, while the non-toxic full-length rat IAPP peptide does not. This result was confirmed by solid-state NMR spectroscopy which shows that in bicelles composed of regions of high curvature

* Reproduced in part with permission from Smith, P. E. S., J. R. Brender, and A. Ramamoorthy. 2009. Induction of Negative Curvature as a Mechanism of Cell Toxicity by Amyloidogenic Peptides: The Case of Islet Amyloid Polypeptide. J. Am. Chem. Soc. 131:4470-4478. Copyright 2009 American Chemical Society

and low curvature, non-toxic $rIAPP_{1-37}$ binds to the regions of low curvature while toxic $rIAPP_{1-19}$ bind to regions of high curvature. Similarly, solid-state NMR spectroscopy shows that the toxic $rIAPP_{1-19}$ peptide significantly disrupts the lipid bilayer structure, whereas the non-toxic full-length rat-IAPP has no significant effect. These results indicate IAPP may induce the formation of pores by the induction of excess membrane curvature, and can be used to guide the design of compounds that can prevent the cell-toxicity of IAPP. This mechanism may be important to understand the toxicity of other amyloidogenic proteins. This atomic-level solid-state NMR study also demonstrates the use of bicelles to measure the affinity of biomolecules for negatively or positively curved regions of membrane, which we believe will be useful in a variety of biochemical and biophysical investigations related to the cell membrane.

2.2 Introduction

Amyloid proteins have been implicated in the etiology of numerous diseases like type 2 diabetes (1), Alzheimer's disease (2-4), Parkinson's disease (5-6), Huntington's disease (7), and Bovine Spongiform Encephalopathy (8). Investigating the mechanisms that trigger the amyloid misfolding process is critical in the development of compounds to treat these diseases. Several studies have shown that the interactions of these amyloid proteins/peptides with cell membranes catalyze the conversion from their non-toxic to their toxic forms (9-17). Therefore, the affinity of amyloidogenic peptides towards the cell membrane is particularly important in the formation of toxic oligomeric intermediates that leads to the disruption of lipid bilayer structure. In this study we report an investigation of IAPP (also known as amylin)-membrane interactions that are correlated with type 2 diabetes.

Type 2 diabetes is the result of both increased resistance to insulin and decreased insulin production by β-cells (18). The relative contribution of each factor to the pathology of the disease is still uncertain, however recent research suggests that most genes predisposing individuals to type 2 diabetes are associated with the maintenance of β-cell mass and not insulin resistance (19), illustrating the key role the loss of β-cell mass plays in the early stages of the disease (20-21). The pathological aggregation of human Islet Amyloid Polypeptide (hIAPP, also known as amylin) has been shown to be central to this process. IAPP is a 37 residue peptide hormone that acts synergistically with insulin in glycemic control. Dense masses of IAPP composed of long cross beta-sheet amyloid fibers are found in the pancreatic islets of 90% of diabetic patients (22). Aggregates of hIAPP disrupt the integrity of the β-cell membrane, allowing entry of Ca^{+2} ions into the cell (23-26). Elevated intracellular calcium levels then impose oxidative stress on the β-cell as the mitochondria attempt to maintain ion balance in the cell. The ultimate result is apoptosis and β-cell death (26-29).

Several characteristics of hIAPP may explain its membrane disrupting activity, but one of the most notable features of hIAPP is its tendency to distort membranes (30-32). These morphological changes in membrane structure appear to be related to the aggregation of the peptide. The linear growth of a rigid amyloid fiber attached to a flexible membrane causes a curvature strain in the membrane, which is relieved by a distortion of the membrane shape. An excessive amount of curvature strain can result in membrane fragmentation by the forcible detachment of membrane patches from the surface (30, 33-34). Moreover, it is likely that a distorted membrane will be more permeable to the passage of small solutes (32). Other highly curved membrane structures

have also been observed after the addition of hIAPP. Highly curved striations in the membrane surface have been reported in liposomal suspensions and islet cells in the regions where the amyloid fiber contacts the membrane surface (14, 24). Striations of the membrane cause a mechanical stress within the membrane and may be responsible for the opening of mechanosensitive calcium channels by IAPP leading to an ER stress response and β-cell death (35).

Curvature plays an important role in the normal physiological functioning of biomembranes, allowing them to assume shapes that are optimal for their function. Peptides can alter the energetic cost of deforming the bilayer and, because membrane proteins are energetically coupled to the bilayer, peptide binding can lead to conformational changes in other membrane proteins throughout the bilayer (36-37). For example, by inducing excessive curvature in the membrane certain antimicrobial peptides create transient pores that kill the target bacteria (38-41). It is possible that membrane curvature plays a similar role in the pathology of IAPP as it plays in the function of antimicrobial peptides. To investigate this possibility, we characterized IAPP induced membrane curvature in lipid bilayers and study its effects on the physicochemical properties of the bilayer. Furthermore, we uncovered a correlation between the toxicity of IAPP and its fragments and their ability to induce negative curvature strain in lipid bilayers.

To test the effect of curvature stress in membrane damage by IAPP and to isolate the effects of non-amyloid dependent membrane damage, we have used four IAPP peptides (Figure 2.1) that have different propensities for the formation of amyloid fibers and for disrupting membranes. Full-length $hIAPP_{1-37}$ forms amyloid fibers and displays a

high toxicity to cells (1, 25, 42-46). The rat version of IAPP ($rIAPP_{1-37}$) differs from hIAPP by six residues, all but one of these (the H18R substitution) are in the 20-29 region believed to be primarily responsible for the aggregation into amyloid fibers (47). The prolines within the $rIAPP_{1-37}$ sequence are believed to prevent the aggregation of $rIAPP_{1-37}$ into amyloid fibers. Despite possessing a similar α-helical conformation in the membrane as $hIAPP_{1-37}$, $rIAPP_{1-37}$ does not disrupt membranes to a significant extent and is non-toxic to cells (13, 15). The 1-19 fragment of hIAPP lacks the amyloidogenic region (residues 20-29) and does not form amyloid fibers while bound to the membrane (48), although it has a weak propensity to form amyloid fibers in solution (49). Nevertheless, despite its lack of amyloidogenicity, $hIAPP_{1-19}$ has a high potential to disrupt both artificial membranes and islet cells (48, 50). Like $hIAPP_{1-19}$, $rIAPP_{1-19}$ is also toxic to islet cells, albeit at a reduced rate (50).

It has been a major challenge to measure the affinity of biomolecules such as peptides or proteins for negatively or positively curved cell membrane regions. The main difficulties are in identifying a suitable model membrane that possesses both senses of curvature and a biophysical tool that can measure high-resolution structural details associated with the biomolecule-membrane binding. In this study, we demonstrate the use of bicelles as suitable model membranes to accomplish this task. Solid-state NMR experiments on magnetically aligned 9:9:4 DMPC: DMPG: DHPC bicelles were used to determine the atomic-level disruption of lipid bilayer structures due to IAPP peptides. While 2D PDLF solid-state NMR experiments were used to determine the peptide-induced changes in the order of ^{13}C-^{1}H bonds in the hydrophobic core and the glycerol regions of the lipids, ^{31}P chemical shift and ^{14}N quadrupole coupling parameters were

used to evaluate changes in the head group region. DSC experiments were used to determine the peptide-induced curvature strain on DiPoPE lipid bilayers. These results are correlated with the cell-toxicity of IAPP peptides and used to determine the mechanism of membrane disruption.

2.3 Experimental Methods

All lipids were purchased from Avanti Polar Lipids (Alabaster, AL). Chloroform and methanol were procured from Aldrich Chemical Inc. (Milwaukee, WI). All chemicals were used without further purification.

2.3.1 Preparation of Peptide Samples

Lyophilized $hIAPP_{1-37}$, $hIAPP_{1-19}$, or $rIAPP_{1-19}$ was dissolved in HFIP at a concentration of 10 mg/ml for one hour to break up any pre-formed aggregates present in the solution. Aliquots of the peptide stock solution were then flash-frozen in liquid nitrogen and lyophilized again for more than 16 hours at less than 1 millitorr vacuum to completely remove HFIP. The lyophilized pellet was then dissolved in methanol at 4 mg/ml and then the appropriate amount was added to lipids dissolved in choloroform to prepare samples for NMR or DSC experiments as given in detail below. Rat $IAPP_{1-37}$, which does not aggregate, was dissolved directly in methanol at 4 mg/ml. Note that while the L_α to H_{II} transition temperatures were reproducible, the amount of DiPoPE lipid in the DSC spectrometer cells was very sensitive to sample preparation and therefore the intensities of the peaks were not reproducible.

2.3.2 Preparation of Bicelle Samples

Bicelles were prepared by mixing 60 mg total of DMPC, DMPG, and DHPC (9:9:4 mole ratio, q ratio = 4.5) dissolved in chloroform with the appropriate amount of the peptide (1% rIAPP1-37, 0.5% $rIAPP_{1-19}$) dissolved in methanol. The bulk solvent was removed by slowly evaporating the lipid mixture under a stream of nitrogen. Residual solvent was removed placing the sample under high vacuum overnight. The dried sample was then rehydrated by the addition of 200 μL of 10 mM pH 7.4 HEPES buffer containing 150 mM NaCl buffer to give a hydration level of 66%. The samples were then subjected to repeated heating and cooling cycles above and below the bicelle formation temperature until clear transparent solutions were formed. The sample was not subjected to freezing during the heating and cooling cycles, as previously frozen samples yielded poorly aligned bicelles.

2.3.3 Solid state NMR Spectroscopy

All of the experiments were performed on a Chemagnetics/Varian Infinity 400 MHz solid-state NMR spectrometer. Each sample was equilibrated at 30° C for at least 30 minutes before starting the experiment. ^{31}P NMR spectra were obtained using a spin-echo sequence (90°−τ−180°−τ−acquisition; τ = 125 μs) with a 90° pulse length of 5 μs under 30 kHz proton decoupling. Chemical shifts were referenced by setting the isotropic chemical shift peak of phosphoric acid to 0 ppm. ^{14}N quadrupolar spectra were recorded using a quadrupolar echo sequence (90°−τ−90°−τ−acquisition; τ = 80 μs) without proton decoupling. Proton detected local field (PDLF) spectra were recorded as described elsewhere (51-52). Briefly, a ramped-cross-polarization (ramp-CP) sequence with a contact time of 3 ms was used to record the 1D ^{13}C chemical shift spectra under

FLOPSY-8 proton decoupling. 2D PDLF spectra were obtained using 70 t_1 increments, a 5 s recycling delay, and a 25 kHz ^{1}H decoupling. The observed dipolar couplings were converted into order parameters using the relation:

$$S_{CH} = \frac{2kD_{Obs}}{D_0(3\cos^2\theta - 1)} \quad [2.1]$$

where D_{obs} is the observed dipolar coupling, D_0 is the dipolar coupling in the absence of motional averaging (~21.5 kHz), θ is the angle between the membrane and the magnetic field (90º), and k is a scaling factor dependent on the homonuclear decoupling sequence employed during the t_1 period (0.84 for the BLEW-8 sequence). All measurements were performed at 30°C.

2.3.4 Differential scanning calorimetry

The peptide stock solution and DiPoPE in choloroform were co-dissolved and the solution was dried under a stream of nitrogen. The peptide/lipid film was then further dried under high vacuum for several hours to remove residual solvent. Buffer (10 mM Tris/HCl, 100 mM NaCl, 1 mM EDTA, 0.002 % w/v NaN_3, pH 7.4) was added to each sample to produce a 10 mg/ml lipid solution, which was briefly vortexed and then degassed without freeze thawing. The liquid crystalline (L_α) to inverted hexagonal phase (H_{II}) transition temperature was measured with a CSC 6100 Nano II differential scanning calorimeter (Calorimetry Sciences Corp., Provo, UT). The change in C_p was recorded from 10- 60°C with a heating rate of 1°C/min.

2.4 Results of experiments examining curvature induction

The ability of a peptide to induce curvature in a membrane can be measured by shifts in liquid crystalline (L_α) to the inverted hexagonal phase transition (H_{II}) of DiPoPE lipids (53-57). Membranes in the inverted hexagonal phase resemble inverted (with the polar headgroup facing the center) lipid cylinders with a highly curved surface. Peptides that promote negative curvature in the membrane tend to promote this phase and accordingly decrease the phase transition temperature expected for the transition (58).

Adding toxic IAPP peptides or peptide fragments to suspensions of DiPoPE reduces the lamellar liquid crystalline (L_α) to inverted hexagonal (H_{II}) phase transition of DiPoPE (see Table 1). This reduction of the L_α to H_{II} transition temperature indicates that these peptides induce negative curvature strain in phospholipid membranes. Human $IAPP_{1-37}$ stabilized the negative curvature of the H_{II} phase to the greatest extent, while the non-amyloidogenic $rIAPP_{1-19}$ and $hIAPP_{1-19}$ fragments did so to a lesser extent. Non-toxic $rIAPP_{1-37}$ only negligibly stabilized the negative curvature strain of H_{II} phase. The cooperativity of the L_α to H_{II} transition is also greatly reduced when either $rIAPP_{1-19}$ or $hIAPP_{1-37}$ is added to the DiPoPE vesicle suspension (Figure 2.2).

NMR experiments show that IAPP peptide fragments binds to regions of high curvature in bicelles: The DSC experiments indicate toxic forms of IAPP have an affinity for curved membrane surfaces. To create membranes with flat lamellar surfaces and regions of high positive and negative curvature, we used a mixture of short (DHPC) and long (DMPC and DMPG) chain phospholipids in the form of bicelles (59-61). At the ratio of short to long chain lipids used here, bicelles form perforated lamellar bilayers that align spontaneously in the presence of an external magnetic field (see Figure 2.3) (62-

63). The perforations are lined with DHPC molecules and are toroidally shaped with two types of curvature: negative (concave) curvature in the plane of the bilayer and positive (convex) perpendicular to the membrane surface. The sheet like structure of the bicelles causes them to spontaneously align in a magnetic field. The spontaneous alignment results in sharply resolved peaks in the NMR spectrum of bicelles, facilitating high resolution studies by NMR.

Bicelles containing $hIAPP_{1-19}$, formed a relatively opaque phase, did not align in the magnetic field (see appendix A). While this peptide-induced unalignment of bicelles did not allow us to carry out high resolution solid-state NMR experiments, it indicates that $hIAPP_{1-19}$ has a large effect on the phase structure of bicelles. Human $IAPP_{1-37}$ fibrillizes rapidly in a membrane environment on the time-scale of the NMR experiment. Therefore, we used bicelles mixed with $rIAPP_{1-19}$ or $rIAPP_{1-37}$ as model systems of toxic or non-toxic IAPP variants, respectively (50).

^{31}P NMR of bicelles shows that the $rIAPP_{1-19}$ peptide fragment has a greater affinity for the highly curved perforations of bicelles, than $rIAPP_{1-37}$ peptide (Figure 2.3). This is evident from the -0.7 ppm shift in the ^{31}P peak of DHPC of bicelles containing $rIAPP_{1-19}$ relative to the control sample. On the other hand, the DHPC peak is unshifted for bicelles containing $rIAPP_{1-37}$, indicating $rIAPP_{1-37}$ has little preference for the curved perforations of the bicelle. In contrast, $rIAPP_{1-37}$ has a greater affinity than $rIAPP_{1-19}$ for the long-chain phospholipid in the flat lamellae of bicelles. The ^{31}P peaks of DMPG and DMPC in the $rIAPP_{1-37}$ bicelle both show a shift relative to the control sample (-0.5 ppm for DMPC and -0.2 ppm for DMPG), while there is no detectable shift for the corresponding bicelle sample containing $rIAPP_{1-19}$. Another important observation is the

absence of an isotropic peak in the ^{31}P chemical shift spectra of bicelles, indicating that $rIAPP_{1-37}$ and $rIAPP_{1-19}$ did not fragment the lipid bilayer.

NMR of full-length $rIAPP_{1-37}$ shows a strong interaction between the peptide and the surface of the bilayer but not between the peptide and the bilayer hydrophobic core: The 1D ^{13}C chemical shift spectrum was used to monitor the effects of $rIAPP_{1-37}$ and $rIAPP_{1-19}$ on the ^{13}C nuclei of the DMPC and DMPG lipids. The ^{13}C nuclei of DHPC are not detectable in these spectra because the mobility of DHPC in bicelle mixtures prevents magnetization transfer from ^{1}H nuclei to ^{13}C nuclei during the cross-polarization period of the pulse sequence. DMPG has two glycerol moieties which produce peaks that are indistinguishable in 1D ^{13}C NMR spectra. It is apparent from the one-dimensional ^{13}C spectrum of the bicelle sample shown in Figure 2.4 that full-length $rIAPP_{1-37}$ binds near the glycerol and headgroup regions of the long-chain lipids (DMPG and DMPC). This can be seen from the change in chemical shifts of these peaks relative to the pure lipid bicelle ^{13}C spectrum. By contrast, the one-dimensional ^{13}C spectrum of $rIAPP_{1-19}$ does not show a change in the chemical shifts of the glycerol or headgroup peaks originating from long-chain lipids. This can be expected in the context of the other NMR data presented above, which indicated that $rIAPP_{1-19}$ does not bind bicelles at their planar surfaces (that is the long-chain lipid region), but rather at their highly curved perforations (see Figure 2.3B).

The flexibility of lipid acyl chain tails are more drastically affected by $rIAPP_{1-19}$ than by full-length $rIAPP_{1-37}$: While $rIAPP_{1-19}$ does not bind directly to the long chains lipids in the flat lamellae, ^{1}H-^{13}C PDLF spectra show that $rIAPP_{1-19}$ has an effect on their flexibility. Most of the observed C-H dipolar couplings are similar to the control sample,

however the very end of the acyl chain (carbons 13 and 14 of DMPC/DMPG) has two vicinal dipolar couplings associated with each carbon (Figures 2.5E and 2.6). The first vicinal dipolar coupling is very close to the dipolar coupling associated with the control sample, while the second vicinal dipolar coupling is much larger indicating a much stronger degree of order due to the interaction of the peptide with the lipid.

Rat $IAPP_{1-37}$ has only a small effect on the flexibility of the acyl chains (Figures 2.5 and 2.6). For most of the ^{1}H-^{13}C bonds investigated, the effect of $rIAPP_{1-37}$ on $|S_{CH}|$, a measure of the rigidity of ^{1}H-^{13}C bonds, is not significant. Nevertheless, $rIAPP_{1-37}$ does exert an effect on the flexibility of the long-chain lipid glycerol and headgroup ^{1}H-^{13}C bonds, as would be expected from the change in ^{13}C chemical shifts observed in this region. Overall, the effect observed is a slight decrease in $|S_{CH}|$ for the ^{1}H-^{13}C bonds of the lipid headgroup, except for those ^{1}H-^{13}C bonds directly associated with the phosphate or trimethyl ammonium moieties. For this sample, the decreased flexibility of ^{1}H-^{13}C bonds in the vicinity of the phosphate moiety of DMPC may be interpreted as the disruption of inter-lipid charge-charge associations between the negatively charged phosphate group and the positively charged choline group due to $rIAPP_{1-37}$ interaction with lipids. ^{14}N NMR confirms this hypothesis by showing a reduced qudrupole splitting, ν_Q, suggesting a change in the orientation of the DMPC headgroup as a result of full-length $rIAPP_{1-37}$ changing the electrostatic environment surrounding PC lipid headgroups (see Figure 2.7) (64-68).

2.5 Discussion of experiments examining curvature induction

Misfolding of amyloid-fibril forming peptides is implicated in devastating aging-related diseases. Recent studies have shown that the ability of an amyloid peptide to bind

to the cell membrane and induce disruption of lipid bilayer structure are key properties correlated with the cell toxicity of amyloid peptides (12, 69). Studies on model membranes have shown that the toxicity of amyloid peptides is highly dependent on the lipid composition of the membrane (14-15, 70-71). Therefore, it is important to investigate lipid-peptide interactions to understand the mechanism by which amyloid peptides disrupt lipid bilayer structure and kill cells. In this study, we have investigated the mechanism by which amylin peptides disrupt lipid bilayers using solid-state NMR and DSC experiments. We believe that the results reported in this study can be used to develop compounds to suppress the cell-toxicity of amylin, and also could be extended towards the understanding of the role of lipids on the misfolding pathway of amyloid peptides in general.

We have made key observations regarding the interaction of IAPP peptides with lipid membranes: (i) Both amyloidogenic ($hIAPP_{1-37}$) and largely non-amyloidogenic ($hIAPP_{1-19}$ and $rIAPP_{1-19}$) toxic versions of the peptide strongly favor the formation of negative curvature strain on lipid bilayers. The non-toxic and non-amyloidogenic $rIAPP_{1-37}$ induces only a very small amount of negative curvature with the amount of negative curvature induced decreasing as the peptide concentration is increased. (ii) In a bicelle environment which has regions of short chain lipids with high curvature and long chain lipids with low curvature, toxic $rIAPP_{1-19}$ binds to the short-chain lipids present in regions of high curvature while non-toxic $rIAPP_{1-37}$ binds to the long-chain lipids present in regions of low curvature. (iii) Rat $IAPP_{1-37}$ affects the chemical environment of the glycerol and phosphorus regions in the headgroup region of long-chain lipids, but does not detectably affect the chemical environment of the aliphatic carbons. (iv) Despite

binding to the short chain lipids, $rIAPP_{1-19}$ also significantly perturbs the motions of the aliphatic carbons of long-chain lipid's fatty acid tails.

All of the IAPP peptides and peptide fragments studied lowered the transition temperature for the formation of the inverted hexagonal (H_{II}) phase of DiPoPE. The inverted hexagonal phase has a high negative curvature; therefore peptides that induce negative curvature strain stabilize the H_{II} phase and lower the transition temperature for its formation. While all the IAPP variants favored the formation of the highly curved H_{II} phase, the negative curvature induced by non-toxic full-length $rIAPP_{1-37}$ was small in comparison to the other toxic IAPP peptides and decreased at higher concentrations. The significantly higher degree of curvature induced by toxic variants of IAPP compared to the non-toxic $rIAPP_{1-37}$ suggests a correlation between the peptide's ability to induce curvature strain and its toxicity. The ability to induce negative curvature strain is apparently not related to the presence of amyloid fibers, the fiber formation process, or a propensity for a β-sheet conformation, as the 1-19 fragments of IAPP remains stable in α-helical conformation when bound to lipid bilayers (48).

The induction of negative curvature strain by toxic versions of IAPP may explain the fragmention of bilayers by hIAPP. (30-33) When hIAPP is added to planar bilayers, lipids are initially extruded out of the plain of the bilayer to form long tubular structures lined by closed bilayers with an aqueous core (30). The lipid tubules disappeared from the surface of the membrane over time as they were either sheared off the surface by mechanical stress or incorporated into amyloid fibers on the membrane surface causing severe disruption of the integrity of the membrane. The tendency of the peptide to cause curvature in the membrane may be linked to this process. The formation of lipid tubules

can occur by a heterogeneous distribution of peptide with high concentrations of peptide at the tubule base, where negative curvature is highest, and low concentrations of peptide at the tubule tip (72). DSC experiments confirm that $rIAPP_{1-19}$ is inhomogenously distributed throughout the membrane (50). Similar inhomogenous distributions have also been seen for $hIAPP_{1-37}$, but not $rIAPP_{1-37}$, in the presence of calcium (73). Notably, this process does not depend on the attachment of the membrane to a rigid amyloid fiber.

The degree and type of membrane curvature induced by a peptide is dependent on how it affects the geometry of the lipid-peptide complex, in particular the relative cross-sectional area of the lipid headgroup region near the membrane-water interface and the acyl chain region in the interior of the bilayer. In order for the membrane to remain in a flat lamellar phase, the overall shape of the peptide-lipid complex must be cylindrical with the size of the two regions matching. A cone-shaped peptide-lipid complex with a mismatch between the sizes of these two regions will induce curvature strain in the bilayer, positive curvature strain if the effective size of the head group is larger than the acyl-chain region and negative curvature strain if it is smaller. It can be seen from these considerations that binding of an amphipathic helix like IAPP at the interface between the hydrophilic headgoup region and the hydrophobic acyl chain region will induce positive curvature strain. Conversely, inserting the peptide deeply into the hydrophobic core will induce negative curvature strain.

The degree of insertion of IAPP into the membrane can be inferred by the relative perturbation of the NMR signal at each site. Rat $IAPP_{1-37}$ has little effect on the order of both the acyl chains and the lipid headgroup, as determined by the site-specific order parameter plot generated by the 2D PDLF experiment. This is a strong indication that the

peptide binds superficially to the very top of the lipid bilayer by an electrostatic interaction with the lipid headgroup. Peptides that bind atmospherically to the membrane in this manner without penetration into the bilayer typically do not induce either positive or negative curvature strain, as demonstrated by mutations of the ENTH domain of epsin (74-75). It could also be the case that the majority of the peptide is not bound to the membrane, however this possibility is contradicted by the ^{14}N and ^{31}P spectra. The ^{14}N spectra shows a small but detectable decrease in the ^{14}N quadrupolar splitting; which is indicative of an electrostatic interaction of $rIAPP_{1-37}$ with the phosphate groups of the bilayer.

Unlike $rIAPP_{1-37}$, $rIAPP_{1-19}$ has a strong preference for the DHPC molecules lining the perforations of the bicelle lamellae rather than the bicelle's planar surface, as shown by the strong perturbation of the ^{31}P peak corresponding to DHPC (Figure 2.3D) and the negligible perturbations of the 13C chemical shifts in the DMPC/DMPG headgroup region (Figure 2.4C). This preference for the perforations of the bilayer is similarly reflected in the ^{14}N spectra, $rIAPP_{1-19}$ induces only a slight increase in the quadrupolar coupling of the long chain lipids but a relatively large increase in the quadrupolar coupling of DHPC (Figure 2.7B).

Rat $IAPP_{1-19}$ has an unusual and significant effect on the aliphatic carbons of both DMPC and DMPG's acyl chains in the NMR experiments. At the very end of the acyl chain (carbons 13 and 14) two vicinal dipolar couplings can be detected for each carbon. The first vicinal dipolar coupling has an order very similar to the control bicelle without peptide. The second vicinal dipolar coupling is significantly larger, indicating a region of the membrane where the terminus of the acyl chain is substantially more ordered in the

presence of $rIAPP_{1-19}$. This set of dipolar couplings most likely corresponds to the annulus of DMPC/DMPG lipids surrounding the bicelle perforation. An increase in order may be due to either bulky residues interfering sterically with the lipid tails of nearby long-chain lipids or interdigitation of the acyl chain termini into the adjoining leaflet due to the compression of the bilayer around the region of the perforation.

The perforations in the bicelle possess regions of both positive curvature (parallel to the membrane normal) and negative curvature (perpendicular to the membrane normal). As such, they serve as models for the toroidal pores produced by certain antimicrobial peptides (39, 53-54), which recent studies have noted distinct similarities to amyloidogenic proteins (30, 76-81). The toroidal pore is formed by a transient high local concentration of peptide that induces enough curvature in the membrane to form a metastable pore lined by the headgroups of phospholipids, rather than by protein as in most pore models. Although most antimicrobial peptides form toroidal pores by stabilizing positive curvature, some antimicrobials form toroidal pores by stabilizing negative curvature instead (82-84). The creation of toroidal pores as a result of the induction of negative curvature may be a novel mechanism for amyloid-induced peptide disruption.

Although the results presented here are for IAPP peptides, the induction of negative curvature strain may be a general mechanism of membrane disruption by amyloidogenic peptides. Solid-state NMR has shown a preferential interaction with the headgroups of PE for $A\beta_{29-42}$ in POPC/POPE membranes, even at a low (10%) percentage of POPE (85). PE lipids have a high propensity for negative spontaneous curvature due to the small size of the headgroup relative to the hydrophobic core. The preferential binding

of $A\beta_{29-42}$ to PE lipids may reflect the similar preference of IAPP to bind to regions of high curvature shown in this study. Furthermore, $A\beta_{1-40}$ has been shown to dehydrate membranes, which reduces the effective headgroup size and will likely lead to negative curvature (86). Alpha-synuclein, another neurotoxic peptide implicated in Parkinson's disease, also has a strong preference for PE lipids over the identically charged PC lipids, suggesting lipid intrinsic curvature is an important determinant of lipid binding specificity for amyloidogenic proteins (11, 87). The preference of amyloidogenic peptides for lipids with a high negative curvature is expected to enhance membrane fusion, as membrane fusion proceeds through a high energy intermediate similar in structure to the inverted hexagonal phase (58, 88). Indeed, the amyloidogenic peptides α-synuclein, Aβ, and some prion fragments have been shown to be fusogenic (85, 89-94).

2.6 Acknowledgements

This research was supported by the research funds from National Institutes of Health (AI054515) and Michigan Diabetes Research Training Center at the University of Michigan. We acknowledge Dr. Lindsey Gottler for help with the DSC experiments. We also thank Dr. Jiadi Xu, Kazutoshi Yamamoto, and Kevin Hartman for helpful discussion.

Table 2.1 The effects of IAPP peptides and peptide fragments on the L_α to H_{II} transition temperature of DiPoPE. The L_α to H_{II} transition temperatures were determined from the third DSC thermogram of the sample (for pure DiPoPE, this temperature was determined to be 45.5 °C)

Peptide or peptide fragment	0.1 mol % peptide	0.5 mol % peptide
DiPoPE containing $rIAPP_{1-37}$	43.6°C	44.3°C
DiPoPE containing $rIAPP_{1-19}$	42.3°C	38.7°C
DiPoPE containing $hIAPP_{1-37}$	39.1°C	~40°C
DiPoPE containing $hIAPP_{1-19}$	43.3°C	40.9°C

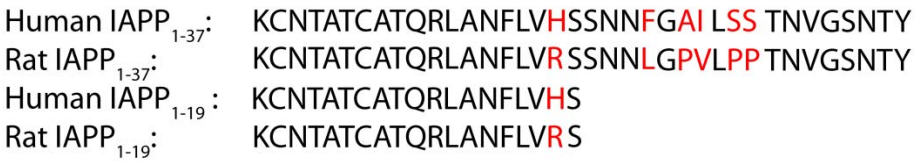

Figure 2.1 Amino acid sequences of the rat and human IAPP peptide analogues used in this study. The differences between the rat and human sequences are shown in red. There are disulfide bonds between residues 2 and 8 and the C-termini of the peptides are amidated like the physiologically expressed peptide.

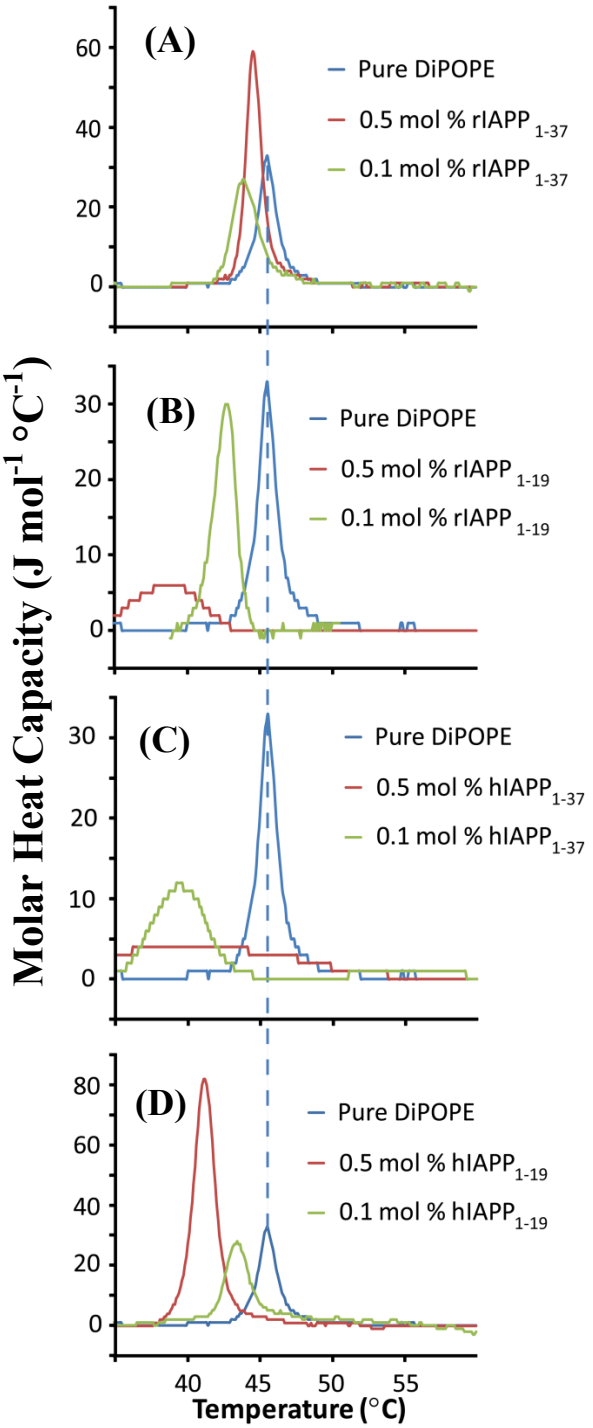

Figure 2.2 Toxic islet amyloid polypeptide peptides and peptide fragments induce more negative curvature strain in membranes than non-toxic rIAPP$_{1-37}$. The third DSC heating scan of IAPP peptides and peptide fragments in DiPoPE at the listed molar percentage of peptide. (A) rIAPP$_{1-37}$ in DiPoPE; (B) rIAPP$_{1-19}$ in DiPoPE; (C) hIAPP$_{1-37}$ in DiPOPE; (D) hIAPP$_{1-19}$ in DiPoPE.

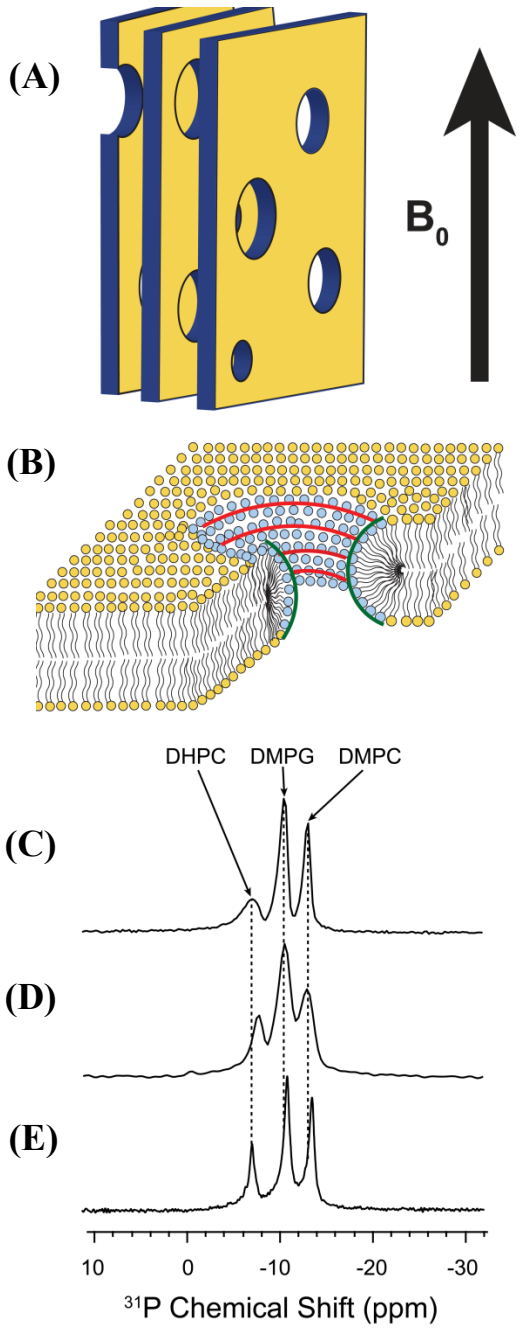

Figure 2.3 ^{31}P NMR shows that rIAPP$_{1-19}$ binds short-chain phospholipids in bicelles whereas rIAPP$_{1-37}$ binds the long-chain phospholipids. (A) A cartoon depiction of magnetically-aligned bicelles in the lamellar phase showing the parallel bicelle lamellae composed of DMPC and DMPG and the perforations composed of DHPC. The large, static magnetic field of the NMR spectrometer is indicated. (B) Zoomed in cartoon depiction of the bicelles, showing the regions of positive and negative curvature. (C) The ^{31}P NMR spectrum of the pure bicelle sample. (D) The ^{31}P NMR spectrum of the rIAPP$_{1-19}$ bicelle sample. (E) The ^{31}P NMR spectrum of the rIAPP$_{1-37}$ bicelle sample.

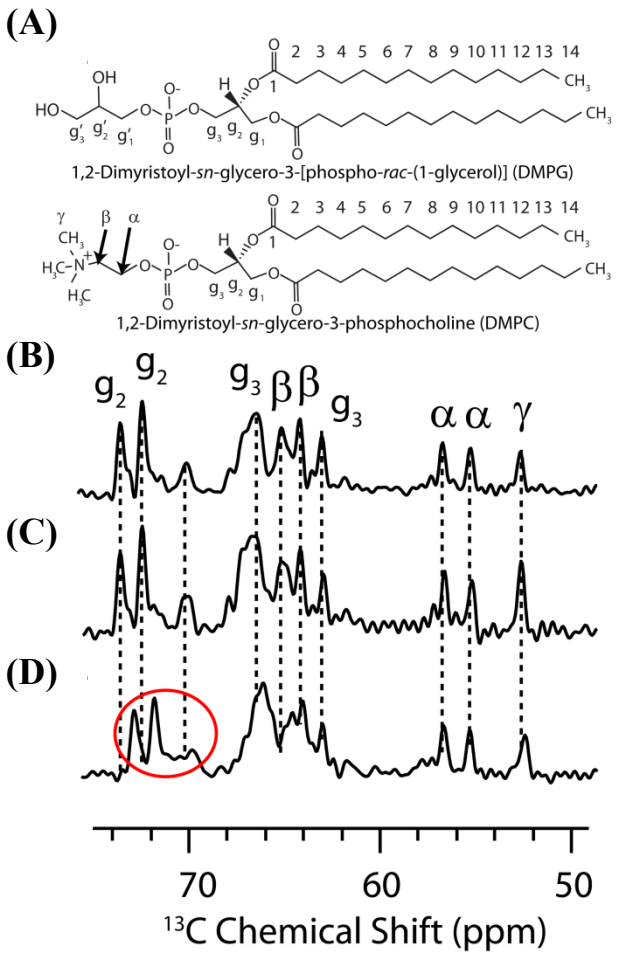

Figure 2.4 The ^{13}C chemical shift spectra show that in bicelles, rIAPP$_{1-37}$ binds DMPC and DMPG at their glycerol regions. (A) Structures of the long-chain phospholipids (DMPG and DMPC) indicating the labeling convention. (B) ^{13}C spectrum of the headgroup region of the pure bicelle sample, (C) rIAPP$_{1-19}$ bicelle sample and (D) rIAPP$_{1-37}$ bicelle sample. The glycerol peaks which are shifted relative to the pure bicelle peaks are circled in red.

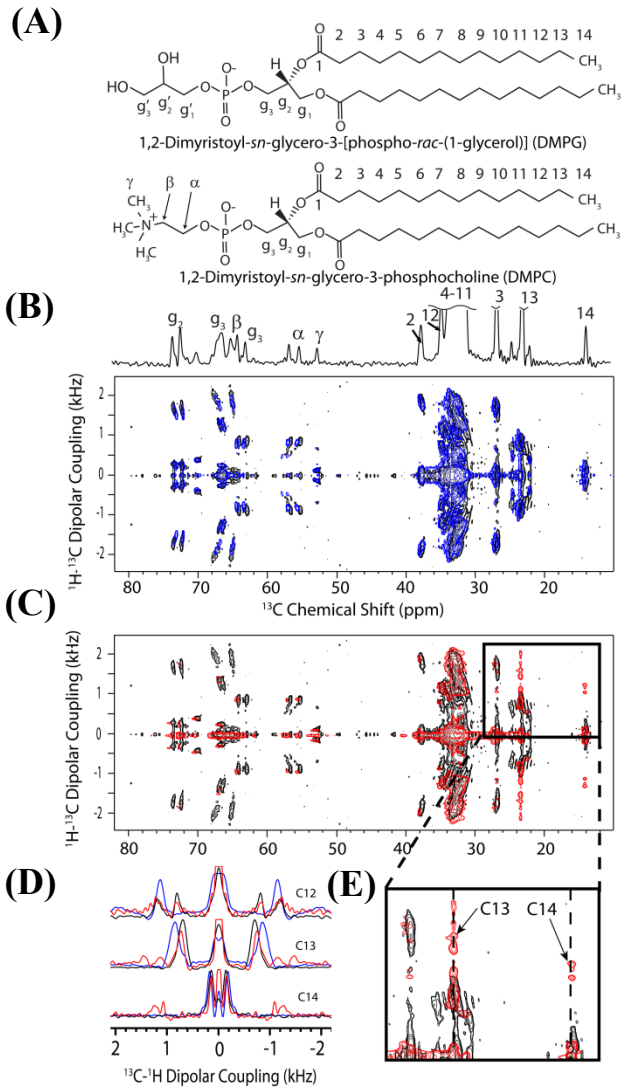

Figure 2.5 2D PDLF NMR experiments show that rIAPP$_{1-19}$ disturbs the aliphatic fatty acid chains of the long-chain phospholipids in bicelles, even though it does not affect their headgroups. (A) The long-chain phospholipids of the bicelle samples (DMPG and DMPC) indicating the labeling convention used. Also shown is the 1D ^{13}C chemical shift spectrum, indicating the frequency of ^{13}C peaks in the horizontal dimension of the PDLF spectra. (B) The 2D ^{1}H-^{13}C PDLF spectrum of bicelles containing rIAPP$_{1-37}$ (blue) superimposed upon the pure bicelle spectrum (black). (C) The 2D ^{1}H-^{13}C PDLF spectrum of bicelles containing rIAPP$_{1-19}$ (red) superimposed upon the pure bicelle spectrum (black). (D) The ^{13}C-^{1}H dipolar coupling slices corresponding to carbons 12, 13, and 14 of the aliphatic fatty acid chains of DMPG and DMPC. Slices corresponding to the pure bicelle sample are shown in black; bicelles containing rIAPP$_{1-37}$, blue; and bicelles containing rIAPP$_{1-19}$, red. (E) A zoomed in area of the PDLF spectrum showing the significant change in the dipolar couplings associated with carbons 13 and 14 of DMPG and DMPC induced by rIAPP$_{1-19}$.

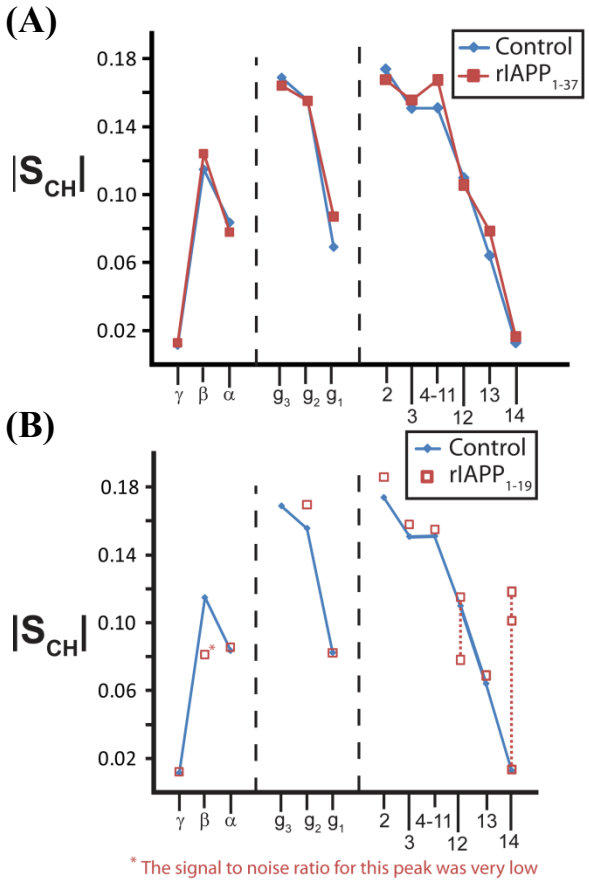

Figure 2.6 The order parameter plots associated with bicelles containing either rIAPP$_{1-37}$ or rIAPP$_{1-19}$. (A) is the order parameter plot for the sample associated with rIAPP$_{1-37}$ and (B) is for the sample associated with rIAPP$_{1-19}$. The order parameter plots are derived from their associated PDLF spectra as described in the methods section. The order parameter plot of pure bicelles is given in blue. Note that one $|S_{CH}|$ value for carbons 12, 13, and 14 of bicelles containing rIAPP$_{1-19}$ is nearly identical to the corresponding value for the pure bicelle sample, indicating some lipids in the sample are unaffected by rIAPP$_{1-19}$.

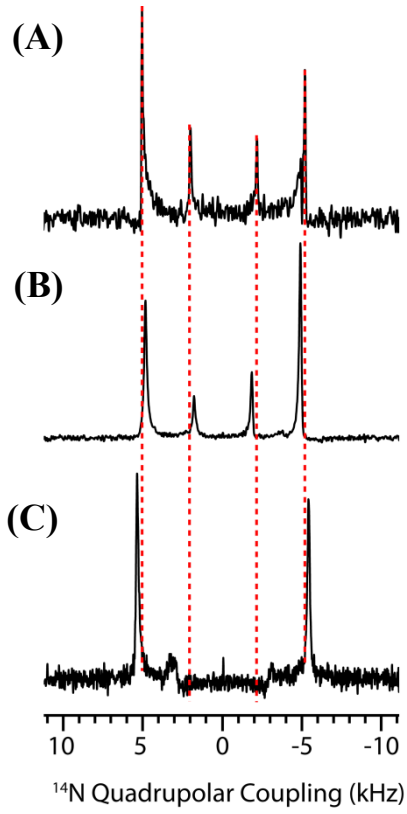

Figure 2.7 ^{14}N NMR shows that rIAPP$_{1-19}$ binds short-chain phospholipids in bicelle phospholipid mixtures whereas rIAPP$_{1-37}$ binds the long-chain phospholipids. (A) The ^{14}N quadrupolar NMR spectrum of the pure bicelle sample. The quadrupolar coupling constant (ν_Q) associated with DMPC is 10.2 kHz, and the ν_Q associated with DHPC is 4.2 kHz. DMPG does not have a ^{14}N nucleus, and therefore there are peaks corresponding to DMPG are absent in the ^{14}N spectrum. (B) The ^{14}N spectrum of the rIAPP$_{1-37}$ bicelle sample. The ν_Q associated with DMPC is 9.8 kHz and ν_Q associated with DHPC is 3.6 kHz. (C) The ^{14}N NMR spectrum of the rIAPP$_{1-19}$ bicelle sample. The ν_Q associated with DMPC is 10.8 kHz and ν_Q associated with DHPC is 6.4 kHz.

2.7 References

1. Haataja, L., T. Gurlo, C. J. Huang, and P. C. Butler. 2008. Islet Amyloid in Type 2 Diabetes, and the Toxic Oligomer Hypothesis. Endocr. Rev. 29:302-316.

2. Ferreira, S. T., M. N. N. Vieira, and F. G. De Felice. 2007. Soluble protein oligomers as emerging toxins in Alzheimer's and other amyloid diseases. Iubmb Life 59:332-345.

3. Chimon, S., M. A. Shaibat, C. R. Jones, D. C. Calero, B. Aizezi, and Y. Ishii. 2007. Evidence of fibril-like beta-sheet structures in a neurotoxic amyloid intermediate of Alzheimer's beta-amyloid. Nature Structural & Molecular Biology 14:1157-1164.

4. Chimon, S., and Y. Ishii. 2005. Capturing intermediate structures of Alzheimer's beta-amyloid, A beta(1-40), by solid-state NMR spectroscopy. J. Am. Chem. Soc. 127:13472-13473.

5. Uversky, V. N. 2008. alpha-Synuclein Misfolding and Neurodegenerative Diseases. Curr. Protein Pept. Sci. 9:507-540.

6. Heise, H., W. Hoyer, S. Becker, O. C. Andronesi, D. Riedel, and M. Baldus. 2005. Molecular-level secondary structure, polymorphism, and dynamics of full-length alpha-synuclein fibrils studied by solid-state NMR. Proc. Natl. Acad. Sci. U. S. A. 102:15871-15876.

7. Temussi, P. A., L. Masino, and A. Pastore. 2003. From Alzheimer to Huntington: why is a structural understanding so difficult? EMBO J. 22:355-361.

8. Caughey, B., and G. S. Baron. 2006. Prions and their partners in crime. Nature 443:803-810.

9. Khemtemourian, L., J. A. Killian, J. W. Hoppener, and M. F. Engel. 2008. Recent insights in islet amyloid polypeptide-induced membrane disruption and its role in beta-cell death in type 2 diabetes mellitus. Experimental diabetes research 2008:421287.

10. Jayasinghe, S. A., and R. Langen. 2007. Membrane interaction of islet amyloid polypeptide. Biochim. Biophys. Acta 1768:2002-2009.

11. Jo, E. J., J. McLaurin, C. M. Yip, P. St George-Hyslop, and P. E. Fraser. 2000. alpha-synuclein membrane interactions and lipid specificity. J. Biol. Chem. 275:34328-34334.

12. Beyer, K. 2007. Mechanistic aspects of Parkinson's disease: alpha-synuclein and the biomembrane. Cell Biochem. Biophys. 47:285-299.

13. Knight, J. D., J. A. Hebda, and A. D. Miranker. 2006. Conserved and cooperative assembly of membrane-bound alpha-helical states of islet amyloid polypeptide. Biochemistry 45:9496-9508.

14. Knight, J. D., and A. D. Miranker. 2004. Phospholipid catalysis of diabetic amyloid assembly. J. Mol. Biol. 341:1175-1187.

15. Jayasinghe, S. A., and R. Langen. 2005. Lipid membranes modulate the structure of islet amyloid polypeptide. Biochemistry 44:12113-12119.

16. Apostolidou, M., S. A. Jayasinghe, and R. Langen. 2008. Structure of alpha - Helical membrane-bound hIAPP and its implications for membrane-mediated misfolding. J. Biol. Chem. 283:17205-17210.

17. Davidson, W. S., A. Jonas, D. F. Clayton, and J. M. George. 1998. Stabilization of alpha-synuclein secondary structure upon binding to synthetic membranes. J. Biol. Chem. 273:9443-9449.

18. Accili, D. 2008. Mechanisms of beta cell failure in the pathogenesis of type 2 diabetes. Drug Dev. Res. 69:111-115.

19. Sladek, R., G. Rocheleau, J. Rung, C. Dina, L. Shen, D. Serre, P. Boutin, D. Vincent, A. Belisle, S. Hadjadj, B. Balkau, B. Heude, G. Charpentier, T. J. Hudson, A. Montpetit, A. V. Pshezhetsky, M. Prentki, B. I. Posner, D. J. Balding, D. Meyre, C. Polychronakos, and P. Froguel. 2007. A genome-wide association study identifies novel risk loci for type 2 diabetes. Nature 445:881-885.

20. Kahn, S. E. 2003. The relative contributions of insulin resistance and beta-cell dysfunction to the pathophysiology of Type 2 diabetes. Diabetologia 46:3-19.

21. Levy, J., A. B. Atkinson, P. M. Bell, D. R. McCance, and D. R. Hadden. 1998. Beta-cell deterioration determines the onset and rate of progression of secondary dietary failure in type 2 diabetes mellitus: the 10-year follow-up of the Belfast Diet Study. Diabetic Med. 15:290-296.

22. Luca, S., W. M. Yau, R. Leapman, and R. Tycko. 2007. Peptide conformation and supramolecular organization in amylin fibrils: Constraints from solid-state NMR. Biochemistry 46:13505-13522.

23. Kayed, R., Y. Sokolov, B. Edmonds, T. M. McIntire, S. C. Milton, J. E. Hall, and C. G. Glabe. 2004. Permeabilization of lipid bilayers is a common conformation-dependent activity of soluble amyloid oligomers in protein misfolding diseases. J. Biol. Chem. 279:46363-46366.

24. Mirzabekov, T. A., M. C. Lin, and B. L. Kagan. 1996. Pore formation by the cytotoxic islet amyloid peptide amylin. J. Biol. Chem. 271:1988-1992.

25. Demuro, A., E. Mina, R. Kayed, S. C. Milton, I. Parker, and C. G. Glabe. 2005. Calcium dysregulation and membrane disruption as a ubiquitous neurotoxic mechanism of soluble amyloid oligomers. J. Biol. Chem. 280:17294-17300.

26. Mattson, M. P., and Y. Goodman. 1995. Different Amyloidogenic Peptides Share a Similar Mechanism of Neurotoxicity Involving Reactive Oxygen Species and Calcium. Brain Res. 676:219-224.

27. Mattson, M. P., and S. L. Chan. 2003. Calcium orchestrates apoptosis. Nat. Cell Biol. 5:1041-1043.

28. Lastra, G., and C. Manrique. 2007. The expanding role of oxidative stress, renin angiotensin system, and beta-cell dysfunction in the cardiometabolic syndrome and type 2 diabetes mellitus. Antioxidants & Redox Signaling 9:943-954.

29. Ritzel, R. A., J. J. Meier, C. Y. Lin, J. D. Veldhuis, and P. C. Butler. 2007. Human islet amyloid polypeptide oligomers disrupt cell coupling, induce apoptosis, and impair insulin secretion in isolated human islets. Diabetes 56:65-71.

30. Domanov, Y. A., and P. K. J. Kinnunen. 2008. Islet amyloid polypeptide forms rigid lipid-protein amyloid fibrils on supported phospholipid bilayers. J. Mol. Biol. 376:42-54.

31. Sparr, E., M. F. M. Engel, D. V. Sakharov, M. Sprong, J. Jacobs, B. de Kruijff, J. W. M. Hoppener, and J. A. Killian. 2004. Islet amyloid polypeptide-induced membrane leakage involves uptake of lipids by forming amyloid fibers. FEBS Lett. 577:117-120.

32. Engel, M. F., L. Khemtemourian, C. C. Kleijer, H. J. Meeldijk, J. Jacobs, A. J. Verkleij, B. de Kruijff, J. A. Killian, and J. W. Hoppener. 2008. Membrane damage by human islet amyloid polypeptide through fibril growth at the membrane. Proc. Natl. Acad. Sci. U. S. A. 105:6033-6038.

33. Brender, J. R., U. H. N. Durr, D. Heyl, M. B. Budarapu, and A. Ramamoorthy. 2007. Membrane fragmentation by an amyloidogenic fragment of human Islet Amyloid Polypeptide detected by solid-state NMR spectroscopy of membrane nanotubes. Biochim. Biophys. Acta 1768:2026-2029.

34. Green, J. D., L. Kreplak, C. Goldsbury, X. L. Blatter, M. Stolz, G. S. Cooper, A. Seelig, J. Kist-Ler, and U. Aebi. 2004. Atomic force microscopy reveals defects within mica supported lipid bilayers induced by the amyloidogenic human amylin peptide. J. Mol. Biol. 342:877-887.

35. Casas, S., A. Novials, F. Reimann, R. Gomis, and F. M. Gribble. 2008. Calcium elevation in mouse pancreatic beta cells evoked by extracellular human islet amyloid polypeptide involves activation of the mechanosensitive ion channel TRPV4. Diabetologia 51:2252-2262.

36. Epand, R. M., Y. C. Shai, J. P. Segrest, and G. M. Anantharamaiah. 1995. Mechanisms for the Modulation of Membrane Bilayer Properties by Amphipathic Helical Peptides. Biopolymers 37:319-338.

37. Botelho, A. V., T. Huber, T. P. Sakmar, and M. F. Brown. 2006. Curvature and hydrophobic forces drive oligomerization and modulate activity of rhodopsin in membranes. Biophys. J. 91:4464-4477.

38. Domanov, Y. A., and P. K. J. Kinnunen. 2006. Antimicrobial peptides temporins B and L induce formation of tubular lipid protrusions from supported phospholipid bilayers. Biophys. J. 91:4427-4439.

39. Ramamoorthy, A., S. Thennarasu, D. K. Lee, A. M. Tan, and L. Maloy. 2006. Solid-state NMR investigation of the membrane-disrupting mechanism of antimicrobial peptides MSI-78 and MSI-594 derived from magainin 2 and melittin. Biophys. J. 91:206-216.

40. Hallock, K. J., D. K. Lee, J. Omnaas, H. I. Mosberg, and A. Ramamoorthy. 2002. Membrane composition determines pardaxin's mechanism of lipid bilayer disruption. Biophys. J. 83:1004-1013.

41. Henzler-Wildman, K. A., G. V. Martinez, M. F. Brown, and A. Ramamoorthy. 2004. Perturbation of the hydrophobic core of lipid bilayers by the human antimicrobial peptide LL-37. Biochemistry 43:8459-8469.

42. Janson, J., R. H. Ashley, D. Harrison, S. McIntyre, and P. C. Butler. 1999. The mechanism of islet amyloid polypeptide toxicity is membrane disruption by intermediate-sized toxic amyloid particles. Diabetes 48:491-498.

43. Konarkowska, B., J. F. Aitken, J. Kistler, S. P. Zhang, and G. J. S. Cooper. 2006. The aggregation potential of human amylin determines its cytotoxicity towards islet beta-cells. FEBS Journal 273:3614-3624.

44. Meier, J. J., R. Kayed, C. Y. Lin, T. Gurlo, L. Haataja, S. Jayasinghe, R. Langen, C. G. Glabe, and P. C. Butler. 2006. Inhibition of human IAPP fibril formation does not prevent beta-cell death: evidence for distinct actions of oligomers and fibrils of human IAPP. Am. J. Physiol. 291:E1317-E1324.

45. Anguiano, M., R. J. Nowak, and P. T. Lansbury. 2002. Protofibrillar islet amyloid polypeptide permeabilizes synthetic vesicles by a pore-like mechanism that may be relevant to type II diabetes. Biochemistry 41:11338-11343.

46. Lin, C. Y., T. Gurlo, R. Kayed, A. E. Butler, L. Haataja, C. G. Glabe, and P. C. Butler. 2007. Toxic human islet amyloid polypeptide (h-IAPP) oligomers are intracellular, and vaccination to induce anti-toxic oligomer antibodies does not prevent h-IAPP-induced beta-cell apoptosis in h-IAPP transgenic mice. Diabetes 56:1324-1332.

47. Westermark, P., U. Engstrom, K. H. Johnson, G. T. Westermark, and C. Betsholtz. 1990. Islet Amyloid Polypeptide - Pinpointing Amino-Acid-Residues Linked to Amyloid Fibril Formation. Proc. Natl. Acad. Sci. U. S. A. 87:5036-5040.

48. Brender, J. R., E. L. Lee, M. A. Cavitt, A. Gafni, D. G. Steel, and A. Ramamoorthy. 2008. Amyloid Fiber Formation and Membrane Disruption are Separate Processes Localized in Two Distinct Regions of IAPP, the Type-2-Diabetes-Related Peptide. J. Am. Chem. Soc. 130:6424-6429.

49. Radovan, D., V. Smirnovas, and R. Winter. 2008. Effect of Pressure on Islet Amyloid Polypeptide Aggregation: Revealing the Polymorphic Nature of the Fibrillation Process. Biochemistry In Press.

50. Brender, J. R., K. Hartman, K. R. Reid, R. T. Kennedy, and A. Ramamoorthy. 2008. A Single Mutation in the Non-Amyloidogenic Region of IAPP Greatly Reduces Toxicity Biochemistry In press.

51. Dvinskikh, S. V., U. H. N. Durr, K. Yamamoto, and A. Ramamoorthy. 2007. High-resolution 2D NMR spectroscopy of bicelles to measure the membrane interaction of ligands. J. Am. Chem. Soc. 129:794-802.

52. Dvinskikh, S., U. Durr, K. Yamamoto, and A. Ramamoorthy. 2006. A high-resolution solid-state NMR approach for the structural studies of bicelles. J. Am. Chem. Soc. 128:6326-6327.

53. Hallock, K. J., D. K. Lee, and A. Ramamoorthy. 2003. MSI-78, an analogue of the magainin antimicrobial peptides, disrupts lipid bilayer structure via positive curvature strain. Biophys. J. 84:3052-3060.

54. Wildman, K. A. H., D. K. Lee, and A. Ramamoorthy. 2003. Mechanism of lipid bilayer disruption by the human antimicrobial peptide, LL-37. Biochemistry 42:6545-6558.

55. Epand, R. F., I. Martin, J. M. Ruysschaert, and R. M. Epand. 1994. Membrane Orientation of the Siv Fusion Peptide Determines Its Effect on Bilayer Stability and Ability to Promote Membrane-Fusion. Biochem. Biophys. Res. Commun. 205:1938-1943.

56. Siegel, D. P., and R. M. Epand. 2000. Effect of influenza hemagglutinin fusion peptide on lamellar/inverted phase transitions in dipalmitoleoylphosphatidylethanolamine: implications for membrane fusion mechanisms. Biochim. Biophys. Acta-Biomembr. 1468:87-98.

57. Epand, R. M., and R. F. Epand. 1994. Relationship between the Infectivity of Influenza-Virus and the Ability of Its Fusion Peptide to Perturb Bilayers. Biochem. Biophys. Res. Commun. 202:1420-1425.

58. Epand, R. M. 1998. Lipid polymorphism and protein-lipid interactions. Biochim. Biophys. Acta-Rev. Biomembr. 1376:353-368.

59. Sanders, C. R., B. J. Hare, K. P. Howard, and J. H. Prestegard. 1994. Magnetically-Oriented Phospholipid Micelles as a Tool for the Study of Membrane-Associated Molecules. Prog. Nucl. Magn. Reson. Spectrosc. 26:421-444.

60. Prosser, R. S., F. Evanics, J. L. Kitevski, and M. S. Al-Abdul-Wahid. 2006. Current applications of bicelles in NMR studies of membrane-associated amphiphiles and proteins. Biochemistry 45:8453-8465.

61. De Angelis, A. A., and S. J. Opella. 2007. Bicelle samples for solid-state NMR of membrane proteins. Nat. Protoc. 2:2332-2338.

62. Gaemers, S., and A. Bax. 2001. Morphology of Three Lyotropic Liquid Crystalline Biological NMR Media Studied by Translational Diffusion Anisotropy. J. Am. Chem. Soc. 123:12343-12352.

63. Harroun, T. A., M. Koslowsky, M. P. Nieh, C. F. de Lannoy, V. A. Raghunathan, and J. Katsaras. 2005. Comprehensive Examination of Mesophases Formed by DMPC and DHPC Mixtures. Langmuir 21:5356-5361.

64. Ramamoorthy, A., D. K. Lee, J. S. Santos, and K. A. Henzler-Wildman. 2008. Nitrogen-14 solid-state NMR spectroscopy of aligned phospholipid bilayers to probe peptide-lipid interaction and oligomerization of membrane associated peptides. J. Am. Chem. Soc. 130:11023-11029.

65. Semchyschyn, D. J., and P. M. Macdonald. 2004. Conformational response of the phosphatidylcholine headgroup to bilayer surface charge: torsion angle constraints from dipolar and quadrupolar couplings in bicelles. Magn. Reson. Chem. 42:89-104.

66. Santos, J. S., D. K. Lee, and A. Ramamoorthy. 2004. Effects of antidepressants on the conformation of phospholipid headgroups studied by solid-state NMR. Magn. Reson. Chem. 42:105-114.

67. Scherer, P. G., and J. Seelig. 1989. Electric Charge Effects on Phospholipid Headgroups - Phosphatidylcholine in Mixtures with Cationic and Anionic Amphiphiles. Biochemistry 28:7720-7728.

68. Lindstrom, F., M. Bokvist, T. Sparrman, and G. Grobner. 2002. Association of amyloid-beta peptide with membrane surfaces monitored by solid state NMR. In Annual Meeting of the Deutsche-Bunsen-Gesellschaft-fur-Physikalische-Chemie. Royal Soc Chemistry, Potsdam, Germany. 5524-5530.

69. Ulmer, T. S., A. Bax, N. B. Cole, and R. L. Nussbaum. 2005. Structure and dynamics of micelle-bound human alpha-synuclein. J. Biol. Chem. 280:9595-9603.

70. Lau, T. L., J. D. Gehman, J. D. Wade, C. L. Masters, K. J. Barnham, and F. Separovic. 2007. Cholesterol and Clioquinol modulation of A beta(1-42) interaction with phospholipid bilayers and metals. Biochim. Biophys. Acta 1768:3135-3144.

71. Grudzielanek, S., V. Smirnovas, and R. Winter. 2007. The effects of various membrane physical-chemical properties on the aggregation kinetics of insulin. Chem. Phys. Lipids 149:28-39.

72. Campelo, F., H. T. McMahon, and M. M. Kozlov. 2008. The hydrophobic insertion mechanism of membrane curvature generation by proteins. Biophys. J. 95:2325-2339.

73. Sciacca, M. F. M., M. Pappalardo, D. Milardi, D. M. Grasso, and C. La Rosa. 2008. Calcium-activated membrane interaction of the islet amyloid polypeptide: Implications in the pathogenesis of type II diabetes mellitus. Arch. Biochem. Biophys. 477:291-298.

74. Ford, M. G. J., I. G. Mills, B. J. Peter, Y. Vallis, G. J. K. Praefcke, P. R. Evans, and H. T. McMahon. 2002. Curvature of clathrin-coated pits driven by epsin. Nature 419:361-366.

75. Farsad, K., and P. De Camilli. 2003. Mechanisms of membrane deformation. Curr. Opin. Cell Biol. 15:372-381.

76. Sood, R., Y. Domanov, and P. K. J. Kinnunen. 2007. Fluorescent temporin B derivative and its binding to liposomes. J. Fluoresc. 17:223-234.

77. Domanov, Y. A., and P. K. J. Kinnunen. 2006. Antimicrobial peptides temporins B and L induce formation of tubular lipid protrusions from supported phospholipid bilayers. Biophys. J. 91:4427-4439.

78. Zhao, H., R. Sood, A. Jutila, S. Bose, G. Fimland, J. Nissen-Meyer, and P. K. J. Kinnunen. 2006. Interaction of the antimicrobial peptide pheromone Plantaricin A with model membranes: Implications for a novel mechanism of action. Biochim. Biophys. Acta 1758:1461-1474.

79. Sood, R., Y. Domanov, M. Pietiainen, V. P. Kontinen, and P. K. J. Kinnunen. 2008. Binding of LL-37 to model biomembranes: Insight into target vs host cell recognition. Biochim. Biophys. Acta 1778:983-996.

80. Jang, H., B. Ma, R. Lal, and R. Nussinov. 2008. Models of toxic beta-sheet channels of protegrin-1 suggest a common subunit organization motif shared with toxic alzheimer beta-amyloid ion channels. Biophysical journal 95:4631-4642.

81. Jang, H., J. Zheng, R. Lal, and R. Nussinov. 2008. New structures help the modeling of toxic amyloidbeta ion channels. Trends in biochemical sciences 33:91-100.

82. Epand, R. F., T. L. Raguse, S. H. Gellman, and R. M. Epand. 2004. Antimicrobial 14-helical beta-peptides: potent bilayer disrupting agents. Biochemistry 43:9527-9535.

83. Imura, Y., M. Nishida, Y. Ogawa, Y. Takakura, and K. Matsuzaki. 2007. Action mechanism of tachyplesin I and effects of PEGylation. Biochim. Biophys. Acta 1768:1160-1169.

84. Timothy, D. A., A. J. Waring, and M. Hong. 2006. Peptide-lipid interactions of the beta-hairpin antimicrobial peptide tachyplesin and its linear derivatives from solid-state NMR. Biochim. Biophys. Acta 1758:1285-1291.

85. Ravault, S., O. Soubias, O. Saurel, A. Thomas, R. Brasseur, and A. Milon. 2005. Fusogenic Alzheimer's peptide fragment A beta (29-42) in interaction with lipid bilayers: Secondary structure, dynamics, and specific interaction with phosphatidyl ethanolamine polar heads as revealed by solid-state NMR. Protein Sci. 14:1181-1189.

86. Matsuzaki, K., and C. Horikiri. 1999. Interactions of amyloid beta-peptide (1-40) with ganglioside-containing membranes. Biochemistry 38:4137-4142.

87. Rhoades, E., T. F. Ramlall, W. W. Webb, and D. Eliezer. 2006. Quantification of alpha-synuclein binding to lipid vesicles using fluorescence correlation spectroscopy. Biophys. J. 90:4692-4700.

88. Epand, R. M. 2003. Fusion peptides and the mechanism of viral fusion. Biochim. Biophys. Acta 1614:116-121.

89. Dante, S., T. Hauss, A. Brandt, and N. A. Dencher. 2008. Membrane fusogenic activity of the Alzheimer's peptide A beta(1-42) demonstrated by small-angle neutron scattering. J. Mol. Biol. 376:393-404.

90. Dupiereux, I., W. Zorzi, L. Lins, R. Brasseur, P. Colson, E. Heinen, and B. Elmoualij. 2005. Interaction of the 106-126 prion peptide with lipid membranes and potential implication for neurotoxicity. Biochem. Biophys. Res. Commun. 331:894-901.

91. Mingeot-Leclercq, M. P., L. Lins, M. Bensliman, F. Van Bambeke, P. Van der Smissen, J. Peuvot, A. Schanck, and R. Brasseur. 2002. Membrane destabilization induced by beta-amyloid peptide 29-42: Importance of the amino-terminus. Chem. Phys. Lipids 120:57-74.

92. Pillot, T., B. Drouet, R. L. Pincon-Raymond, J. Vandekerckhove, T. Rosseneu, and J. Chambaz. 2000. A nonfibrillar form of the fusogenic prion protein

fragment [118-135] induces apoptotic cell death in rat cortical neurons. J. Neurochem. 75:2298-2308.

93. Pillot, T., B. Drouet, S. Queille, C. Labeur, J. Vandekerckhove, M. Rosseneu, M. Pincon-Raymond, and J. Chambaz. 1999. The nonfibrillar amyloid beta-peptide induces apoptotic neuronal cell death: Involvement of its C-terminal fusogenic domain. J. Neurochem. 73:1626-1634.

94. Pillot, T., M. Goethals, B. Vanloo, C. Talussot, R. Brasseur, J. Vandekerckhove, M. Rosseneu, and L. Lins. 1996. Fusogenic properties of the C-terminal domain of the Alzheimer beta-amyloid peptide. J. Biol. Chem. 271:28757-28765.

CHAPTER 3

THE LOCALIZATION OF DENDRIMERS INSIDE THE HYDROPHOBIC CORE OF LIPID BILAYERS*

3.1 Summary

Poly(amidoamine) (PAMAM) dendrimer nanobiotechnology shows great promise in targeted drug delivery and gene therapy. Because of the involvement of cell membrane lipids with the pharmacological activity of dendrimer nanomedicines, the interactions between dendrimers and lipids are of particular relevance to the pharmaceutical applications of dendrimers. In this study, solid-state NMR was used to obtain a molecular image of the complex of generation 5 PAMAM dendrimer with the lipid bilayer. Using ^{1}H radio frequency driven dipolar recoupling (RFDR) and ^{1}H magic angle spinning (MAS) nuclear Overhauser effect spectroscopy (NOESY) techniques, we show that dendrimers are thermodynamically stable when inserted into zwitterionic lipid bilayers. ^{14}N and ^{31}P NMR experiments on static samples and measurements of the mobility of C-H bonds using a 2D proton detected local field protocol under MAS corroborate these results. The localization of dendrimers in the hydrophobic core of lipid bilayers restricts the motion of bilayer lipid tails, with the smaller G5 dendrimer having more of an effect than the larger G7 dendrimer. Fragmentation of the membrane does not occur at low dendrimer concentrations in zwitterionic membranes. Because these results show that the amphipathic dendrimer molecule can be stably incorporated in the interior of the bilayer (as opposed to electrostatic binding at the surface), they are expected to be useful in the design of dendrimer-based nanobiotechnologies.

3.2 Introduction

Poly(amidoamine) (PAMAM) dendrimers are hyperbranched polymers that adopt a spherical architecture in aqueous environments with the potential to greatly extend the capabilities of modern therapeutics (1-3). The "branches" of dendrimers are composed of ethylenediamine repeat units and natively terminated with amine groups but may be chemically modified to alter the molecular properties of dendrimers in a well-defined manner (4-6). The sheer range of compounds that might be used to terminate dendrimers makes these polymers versatile for nanotherapeutic applications (4-6).

Because of their potential as nanotherapeutics, interactions between PAMAM dendrimers and biomaterials relevant to these dendrimers' *in vivo* behavior are of great interest. Amine-terminated PAMAM dendrimers are known to interact with lipid membranes and are therefore not biologically inert (7-11). These PAMAM dendrimer-biomembrane interactions may aid in certain medicinal applications, drawing these polycationic compounds closer to bacterial and cancer cells whose outer membranes generally carry negative charge, but may interfere with other applications, such as the specific binding of dendrimers to their targeted receptors in targeted drug delivery applications (10, 12-13). Therefore, understanding PAMAM dendrimers' interactions with membranes will aid the development of more effective dendrimer-based therapeutic nanodevices.

Some features of the PAMAM dendrimer-biomembrane interaction have been characterized despite the difficulty inherent in structural studies on membrane and polymer systems (7-9, 11, 14-19). Earlier, we have shown that suspending a dendrimer solution over a lipid bilayer supported on a mica surface results in both the expansion of bilayer defects as well as the formation of new defects (11). ^{31}P NMR has previously

shown that at high concentrations, PAMAM dendrimers fragment the lipid bilayer, producing a soluble lipid-containing component that tumbles isotropically in solution (11). The size of the new defects in supported lipid bilayers induced by dendrimers is reported to be within the range of what would be expected if dendrimer-filled lipid vesicles were abstracted from the supported lipid bilayer, suggesting that the formation of new defects might be the result of abstraction of dendrimer-filled lipid vesicles from the supported lipid bilayer (7). Thermodynamic arguments suggested abstraction occurs as the result of the formation of lipid-dendrimer aggregates composed of a central dendrimer core surrounded by a phospholipid bilayer (11, 15, 20). Recently, Kelly et al. investigated the mechanism whereby PAMAM dendrimers interact with fluid phase lipids (7). They concluded that when PAMAM dendrimers interact with negatively charged lipids, dendrimer-filled lipid vesicles form at higher concentration of dendrimers. However, they detected no heat release upon PAMAM dendrimers' addition to fluid phase zwitterionic lipids and were therefore unable to definitively characterize the mechanism whereby these dendrimers disrupt zwitterionic lipid membranes. Notably, it has been shown that PAMAM dendrimers interact with zwitterionic lipids by experimental techniques such as vesicle leakage (21-22), whole-cell leakage (14, 23), differential scanning calorimetry (24-26), electron paramagnetic resonance (27-28), and Raman spectroscopy (25).

Experimental atomic-resolution structural information on the dendrimer-zwitterionic lipid complex remains elusive, but molecular dynamics (MD) simulations have suggested that dendrimers with charged terminal groups flatten when interacting with biomembranes in order to maximize the number of favorable dendrimer-lipid

interactions (9). Mesoscopic dynamics simulations further show that dendrimers do not flatten completely and may therefore force membranes to pucker to adapt to their natural curvature. This curvature strain may be relieved by the formation of toroidal pores, or pores that have a worm hole-like structure (29-30). It has been shown that toroidal pores will form in lipid bilayers in response to the curvature strain induced by antimicrobial peptides such as magainin2 and pexiganan (MSI-78) (29-30). The induction of curvature strain in lipid bilayers is an important phenomenon in the pathology of various amyloid peptides (31-32). Coarse grained molecular dynamics simulations have also suggested that it may be possible for dendrimers to insert into lipid bilayers without forming pores (17-18).

In this study, we use solid-state NMR spectroscopy to gain atomic-level insights into the structure of the zwitterionic lipid bilayer-dendrimer complex. This approach reveals details of this non-soluble, non-crystalline supramolecular structure at an unprecedented atomistic resolution. Furthermore, the impact of dendrimer size on the dendrimer-lipid bilayer interaction is also studied. Multilamellar vesicles (MLVs), which mimic the natural curvature of cell and organelle membranes, are used as a model membrane to examine the membrane interactions of generation-5 and generation-7 dendrimers (see the molecular structures of dendrimers given in Figure 3.1). ^{31}P and ^{14}N NMR experiments are used under static conditions and R-PDLF, NOESY, RFDR, and ^{1}H NMR are used under MAS to elucidate the structural and dynamical properties of a model lipid biomembrane in the presence of dendrimers. Our results indicate that dendrimers localize in the interior of lipid bilayers in our samples enabling the intercalation of lipid acyl chains into the dendrimer interior, in agreement with previous

electron paramagnetic resonance (EPR) studies that have shown that PAMAM dendrimers are likely to insert in zwitterionic lipid bilayers (28). We expect that these results will aid in the development of new and powerful nanomedicinal treatments for a wide variety of diseases, specifically advanced dendrimer-based nanocarriers that encapsulate hydrophobic drugs and deliver them to the interior of biomembranes.

3.3 Experimental methods

All lipids were purchased from Avanti Polar Lipids (Alabaster, AL). Chloroform and methanol were procured from Aldrich Chemical Inc. (Milwaukee, WI). All the chemicals, unless noted otherwise, were used without further purification.

3.3.1 Preparation of PAMAM dendrimers

Generation 5 and 7 PAMAM dendrimers were purchased from Dendritech Inc. To remove lower molecular weight impurities and trailing generations, the dendrimers were dialyzed with a 10,000 MWCO membrane (generation 5) or 50,000 MWCO membrane (generation 7) against deionized water for two days with four water exchanges. The purified dendrimer was lyophilized for three days, resulting in a white solid. The number average molecular weight and polydispersity index were determined by gel permeation chromatography (28,460 g/mol and 1.011 ± 0.010 respectively for generation 5 and 105,600 g/mol and 1.053 ± 0.012 for generation 7). The mean number of terminal primary amines per dendrimer (112 for generation 5 and 486 for generation 7) were determined from the number average molecular weight by potentiometric titration as described by Majoros et al. (33) An illustration of the branched structure of the dendrimer along with the labeling convention used in this study is provided in Figure 3.1.

3.3.2 Preparation of samples for R-PDLF and ^{14}N NMR

For the R-PDLF and ^{14}N experiments, partially hydrated lipid and PAMAM dendrimer samples were prepared (approximately 10 water molecules per lipid). Drier samples were used as the dipolar couplings are larger in drier samples and therefore the differences between the dipolar couplings are larger which improves the resolution of our 2D SLF experiments in the indirect dimension. Therefore DMPC and dendrimer samples prepared at low hydration levels by first dissolving 70 mg of DMPC powder in methanol with 3 wt % PAMAM dendrimer (either G7-amine, also referred to as sample A3, or G5-amine, also referred to as sample A2) in a culture tube. The sample was then dried under a stream of N_2 and placed under vacuum overnight. The sample was then placed under 95% humidity at 37 °C and hydrated until approximately 10 water molecules per lipid molecule were present as established by comparing the lipid γ carbon's protons' peak area with that of the water protons' in a ^{1}H MAS NMR experiment (see appendix B). A litmus test indicated that our sample was at approximately neutral pH, indicating that the terminal amines are protonated but the interior tertiary amine groups are not. (34) A control sample of DMPC without dendrimer was also prepared (also referred to as sample A1). The contents were then transferred to a 4 mm diameter NMR rotor.

3.3.3 R-PDLF and ^{14}N NMR experiments on the indirectly hydrated sample

The dynamics of the lipid molecules and G5 and G7 dendrimers were probed using a combination of a 2D MAS technique, R-PDLF, which correlates ^{13}C chemical shifts to their associated ^{13}C-^{1}H dipolar couplings, and static ^{14}N NMR spectroscopy. In the R-PDLF experiment, the intrinsic lipid ^{13}C-^{1}H dipolar couplings are motionally averaged by the flexibility of the acyl chains within the bilayer. The observed dipolar

couplings therefore reflect the local order $S_{|CH|}$ associated with different regions of the phospholipid molecules. The local order parameter is defined as the observed dipolar coupling divided by the scaling factor for the rotor-synchronized C-H recoupling sequence, 0.315 (35), and the rigid lattice directly binded C-H dipolar coupling, 21.5 kHz (for a bond length of ~1.1 Å).

R-PDLF spectroscopy incorporates R-type recoupling (35) into the proton detected local field (PDLF) protocol (36). Since the refocused-INEPT pulse sequence renders high spin pair selectivity (37), it was used for the ^{1}H to ^{13}C polarization transfer. The ^{1}H field strengths during dipolar recoupling and heteronuclear decoupling were typically 45 and 28 kHz, respectively. The 2D spectra were acquired using typically 128 scans and 200 increments in the t_1-dimension. A 5 s recycling delay was employed with magic angle spinning (MAS) at 5.15 kHz stabilized to ± 2 Hz accuracy. Further details of the R-PDLF method can be found elsewhere (38-39).

The R-PDLF and ^{14}N NMR experiments were performed on a Chemagnetics/Varian Infinity 400 MHz solid-state NMR spectrometer. Each sample was equilibrated at 37 °C for at least 30 minutes before starting the experiment. The ^{14}N spectra were obtained with a recycle delay of 3 s and 50 kHz of spectral width. The recoupled C-H dipolar coupling is sensitive to the molecular conformation of the lipid phosphatidyl choline (PC) headgroup as follows:

$$S_{|CH|} = \left| \frac{1}{2} (3\cos^2\eta - 1) S_f \right| \qquad [3.1]$$

where η is the angle between the C-H bond and the motional axis (the long axis of the lipid molecule) and S_f is an order parameter representing wobbling motions about the membrane long axis (40).

To study the PC headgroup tilt, the angle ($\theta_{P—N}$) that the vector originating at the phosphorus nucleus of DMPC and pointing to the nitrogen nucleus of DMPC (the P-N vector) makes with the membrane normal is assessed. According to previous studies, $\theta_{P—N}$ can be approximated from η according to the equation:

$$\cos\eta = 0.784\cos\theta_{P\text{-}N} \qquad [3.2]$$

Based on the hydration level of our pure lipid (DMPC) sample (n_w~10, see appendix B) and the results of Ulrich et al. (41), we estimate $\theta_{P—N}$ to be ~62° for our pure DMPC sample (41-43). We calculated S_f to be ~ 0.44 after solving for η using equation 3.2 and substituting our experimental results for S_{CH} into equation 3.1. Using this information, we were able to calculate $\theta_{P—N}$ and estimate how the addition of dendrimers to lipid bilayers changes molecular headgroup tilt of DMPC, which is associated with changes in the lipid bilayer electrostatics. When calculating the DMPC molecular headgroup tilt, tilts were calculated using the average of the experimentally determined C_α-H and C_β-H dipolar couplings.

3.3.4 Preparation of fully-hydrated DMPC multilamellar vesicle (MLV) samples for NOESY and RFDR experiments

For the ^{1}H MAS NOESY and ^{1}H RFDR experiments, 35 mg of DMPC powder was dissolved in methanol with 1.7 mg of G5 PAMAM diagnostic grade dendrimer in methanol solution purchased from Sigma-Aldrich in a culture tube (also referred to as

sample B2). The sample was dried under a stream of N_2 and then placed under vacuum overnight. 30 μL 10 mM of sodium phosphate buffer at pH 7.3 was added to the mixture and 5 μL D_2O was added for sample referencing. The pH of the sample prepared for NOESY and RFDR experiments was 8-9.5 (tested using litmus paper). Approximately 25-89% of the dendrimer terminal groups are protonated at these pH levels. By inspection of the titration curves provided in figure 2 of reference 43, upper and lower bound estimates of the fraction of protonated terminal groups could be obtained. At physiological pH (7.4) all of the terminal amine groups are expected to be protonated. None of the tertiary amine groups were protonated at either pH level (7.4 or 8-9.5). (34) The mixture was freeze-thawed three times before being transferred to a 3.2 mm (~50 μL volume) NMR rotor for NMR experiments using a Nanoprobe™. A control sample of fully hydrated pure DMPC lipid MLVs without dendrimer was also prepared (also referred to as sample B1).

3.3.5 NOESY and RFDR experiments on the fully-hydrated DMPC multilamellar vesicles sample

The ^{1}H RFDR and ^{1}H MAS NOESY experiments were performed on a Varian UNITY INOVA 600 MHz spectrometer. A 3.2 mm Nanoprobe™ was used for these experiments. Each sample was equilibrated at 37 °C for at least 30 minutes before starting the experiment. MAS at 2.5 kHz stabilized to ± 1 Hz was employed for the ^{1}H MAS NOESY and ^{1}H RFDR experiments; other experimental details of these techniques can be found elsewhere (44). An 8 kHz pulse on the water ^{1}H resonance was applied for 1.5 s during the recycle delay, 128 t_1 increments were acquired, with a spectral width of 6 kHz in the indirect dimension. Typical RF power used was 25 kHz. ^{1}H MAS NOESY and

^{1}H RFDR spectra of similarly prepared (same hydration level, buffer, pH) pure dendrimer and pure lipid samples were also similarly obtained.

^{31}P NMR spectra of the G5 dendrimer and DMPC lipid and the pure DMPC lipid samples were obtained under 10 kHz magic angle spinning (MAS) using a spin-echo sequence (90°-τ-180°-τ-acq with τ=100 μs), with a 40 kHz proton decoupling RF field, 50 kHz spectral width, 3.1 μs 90°-pulse length, and a recycle delay of ~4 seconds. A typical spectrum required the co-addition of 100–1000 transients. Chemical shifts were referenced by setting the isotropic chemical shift peak of phosphoric acid to 0 ppm. In the resulting pure lipid sample and G5 dendrimer sample spectra, the buffer ^{31}P NMR peak overlapped with the ^{31}P NMR peaks originating from the DMPC lipids. Static ^{31}P NMR spectra were obtained in a water mixture (as opposed to using buffer). We expect the conditions for this sample to be comparable to the conditions under which dendrimers to be similar to the conditions under which other atomic force microscopy (AFM) experimental results were obtained earlier. Static spectra were acquired for G7 dendrimer and lipid, G5 dendrimer and lipid, and pure DMPC lipid samples. All experimental data were processed using the Spinsight (Chemagnetics/Varian) software on a Sun Sparc workstation.

3.4 Results of solid state NMR investigations of the dendrimer-zwitterionic lipid interaction

3.4.1 ^{1}H-^{1}H MAS NOESY and ^{1}H RFDR show that generation 5 PAMAM dendrimers are thermodynamically stable when inserted into lipid bilayers

To determine the location of the dendrimer on the bilayer, we probed the contacts between the dendrimer and the bilayer at Å-level resolution by ^{1}H-^{1}H chemical shift

correlation NMR experiments experiments on G5 dendrimers. In these experiments, the crosspeak intensity, which is a function of the amounts of magnetization transferred between pairs of ^{1}H nuclei, is monitored. Under certain conditions, this information can then be translated into estimates of the distances between pairs of ^{1}H nuclei. However, this interpretation can be complicated by the dependence of the magnetization transfer on the motions of the ^{1}H nuclear pairs. To overcome this complication, two complementary experiments (^{1}H MAS NOESY and ^{1}H RFDR NMR) with different magnetization transfer steps and different time dependencies were used. In an RFDR experiment, magnetization is transferred via ^{1}H-^{1}H dipolar coupling, which is reduced by motions occurring on a timescale faster than a few milliseconds. On the other hand, the magnetization transfer in a NOESY experiment is mediated by NOE cross-relaxation which in this system is predominantly caused by lipid lateral diffusive motions occurring on a timescale of ~170 ns in an unperturbed lipid bilayer (45-46). A concurrence between NOESY and RFDR results is therefore a strong indication that distance, and not the molecular motion of either the dendrimer or the bilayer, is responsible for the observed effect.

Generally, the crosspeaks between the lipid tails and the dendrimer interior are more intense than those of between the lipid headgroup and the dendrimer interior in both the NOESY and RFDR spectra as shown in Figure 3.2. For example, in both the NOESY and RFDR spectra, the *c/14* crosspeaks are more intense than the *c/α* crosspeaks. This is an indication that the dendrimer interior is closer to the interior of the bilayer than the surface of the bilayer. This conclusion is strengthened by the agreement of RFDR and NOESY results, because it appears that regardless of the dependence of magnetization

transfer on the motions of the ^{1}H-^{1}H spin pair, the intensity of crosspeaks between ^{1}H nuclei in the dendrimer interior and the lipid tail is higher than that of between ^{1}H nuclei in the dendrimer's interior and the lipid's headgroups. Since the same result was obtained with both methods, it is likely that the G5 dendrimer is located in the hydrophobic interior of the zwitterionic DMPC lipid bilayer as opposed to lying on the surface under these experimental conditions. Note that insertion here refers to the proximity of the dendrimer to the hydrophobic core of the bilayer, actual intercalation of the lipid tails into the interior of the dendrimer cannot be determined from these results.

3.4.2 Dendrimers are immobilized in a membrane environment

Although the lipid-dendrimer crosspeak intensities give information on the location of the dendrimer within the bilayer, the dendrimer-dendrimer cross-peaks by contrast give information on the dynamics and conformation of the dendrimer. In the pure G5 dendrimer sample, the ^{1}H-^{1}H dipolar couplings were motionally averaged to the point of making a ^{1}H RFDR experiment impossible, suggesting that dendrimers are less mobile in a membrane environment than in an aqueous environment. A comparison of the ^{1}H MAS NOESY spectrum shows that the intramolecular crosspeaks are more numerous and intense while the diagonal peaks are less intense in a G5 dendrimer sample without lipid when compared to a similar sample with DMPC (see Figure 3.3). This corroborates the RFDR results, suggesting that the internal motion of the dendrimer is restricted when bound to the lipid and/or the dendrimer is more compact when bound to the lipid.

3.4.3 Dendrimers rigidify the lipid tails, increasing order in the interior of zwitterionic lipid bilayer

The dynamics of the C-H bonds in DMPC were probed with a 2D MAS technique, R-PDLF, which correlates ^{13}C chemical shifts to their associated ^{13}C-^{1}H dipolar couplings (see Figures 3.4 and 3.5). Segmental order parameters ($S_{|CH|}$) were extracted from the motionally averaged dipolar couplings as described in the Materials and Methods section (see Figure 3.6). While the resolution within the central part of the hydrophobic core of the membrane (carbons 4-11) was poor and the corresponding dipolar couplings could not be accurately measured, the splittings at carbons 3, 12 and 14 were well-resolved and therefore unambiguous assignment was possible for these carbons. At all of these sites the $S_{|CH|}$ values were increased when either G7 or G5 dendrimers are added to the DMPC mixture, indicating dendrimer binding decreases the flexibility of the acyl chains of the membrane. Furthermore, the effect was dependent on the size of the dendrimer with the $S_{|CH|}$ values of the G7 dendrimer sample being lower than those of the G5 dendrimer sample. While both the G7 and G5 dendrimer decrease the flexibility, the $S_{|CH|}$ values associated with the G5 dendrimer sample were higher than those of the G7 sample indicating the G5 dendrimer has a greater impact on the dynamics of the interior of the bilayer.

R-PDLF shows the dipolar couplings associated with α, β, and g_2 carbons in the headgroup region of the DMPC molecule increased for both the G7 and G5 dendrimers samples. The dipolar coupling is decreased for the g_1 carbon in the G7 dendrimer sample but increased in the G5 sample. The correspondence between the measured dipolar coupling and the dynamics in this region is not as direct as it is for the acyl chain carbons, as the headgroup may tilt in response to ligand binding and alter the axis of motional

averaging. The change in dipolar coupling could therefore be either due to a restriction of motions of the lipid tails and a slight increase in headgroup motions relative to the lipid tail for which the g_1 carbon acts as a hinge.

3.4.4 ^{14}N and ^{31}P NMR show that the surface of the lipid bilayer is relatively unaffected by PAMAM dendrimer

The ^{14}N spectra are nearly unaffected by the presence of either G5 or G7 dendrimers, with a slight increase in the ^{14}N quadrupolar splitting evident in the G5 dendrimer sample and a negligible effect evident in the G7 sample (see Figure 3.7). This is an indication that the electric field in the proximity of the choline group is unaltered by the presence of either dendrimer. While such a finding is not unexpected on purely electrostatic considerations for the positively charged dendrimer, it is also an indication that the tilt of the lipid headgroup relative to the surface of the membrane is not affected strongly by either dendrimer since the electric field is a function of the distance from the membrane surface. This observation argues against a strong interaction of either dendrimer with the phosphate group, as an electrostatic interaction of the dendrimer with the phosphate group would induce a torque on the P^-—N^+ dipole causing the headgroup to tilt away from the membrane surface relative to the control ("the molecular voltmeter effect"). The R-PDLF results corroborate the results from ^{14}N NMR. The changes in the ^{13}C-^{1}H dipolar couplings of the lipid headgroups correspond to an estimated change in the tilt of the lipid headgroup tilt by ~1.7° for the G5 sample and ~2.9° for the G7 sample (see the methods and materials section for further details). These changes in lipid headgroup conformation do not correspond to a significant change in bilayer electrostatic properties. A significant increase in the bilayer surface charge is expected to change the

lipid headgroup tilt by >10°, as observed when mixing cationic didodecyldimethylammonium bromide (DDAB) with DMPC lipid bilayers (40).

Further confirmation of an absence of strong electrostatic effects of the dendrimer on the phosphate group can be seen in the ^{31}P NMR spectra (see Figure 3.8). Only minimal changes (<0.1 ppm) in the isotropic chemical shift obtained under MAS are apparent for the G5 sample when compared to the pure lipid DMPC sample, indicating G5 dendrimers have minimal influence on the electrostatic environment of the ^{31}P nucleus. The influence of dendrimers on the phosphodiester moiety was studied in further detail through the use of static ^{31}P experiments. Figure 3.8A shows the control DMPC lipid ^{31}P NMR spectrum, which features a CSA powder pattern lineshape typical for unoriented lipid samples. The binding of both the G5 and G7 dendrimers has only a minor impact on the ^{31}P lineshape: G5 dendrimer binding having virtually no effect and only a slight decrease in the CSA span being evident in the G7 sample. The observed CSA is a function of both the ^{31}P CSA tensor and an order parameter reflecting the motional averaging undergone by the phosphodiester moiety in the lipid headgroup. Since the isotropic chemical shift is unaltered by the presence of either dendrimer, it is reasonable to assign changes in the CSA lineshape to either alterations in the dynamics or conformational rearrangements of the phosphate headgroup that modify the motional averaging of the CSA. We can therefore conclude that neither G5 dendrimer nor G7 dendrimer significantly impact the conformation of the lipid headgroup.

3.5 Discussion of solid state NMR investigations of the dendrimer-zwitterionic lipid interaction

Several lines of evidence suggest that in zwitterionic lipid bilayers prepared for our samples both G5 and G7 dendrimers are localized deep within the interior of the

bilayer and are not merely associated with the surface of the membrane. Note that in both the ^{1}H RFDR and the ^{1}H MAS NOESY spectra of G5 dendrimer–DMPC samples (shown in Figure 3.2) the crosspeaks between the lipid acyl chains and the dendrimer are stronger than the corresponding crosspeaks between the dendrimer and the lipid headgroup. In particular, the crosspeak between the last carbon of the acyl chain of DMPC and "c" carbon of the dendrimer (marked as c/14 in Figures 3.2C and 3.2F) is more intense than corresponding crosspeaks between the dendrimer and the atoms in the lipid-headgroups (marked as c/α and c/g_1) in both the RFDR and NOESY spectra, indicating a close proximity of the hydrophobic core of the dendrimer with the center of the bilayer. While this result could be explained by differences in the dynamics of the headgroup and tail regions of the lipids if it was only observed in the ^{1}H RFDR or only in the ^{1}H MAS NOESY spectra as the dependence of the cross peak intensity in NEOSY and RFDR experiments on motion are different. Therefore, the similarity of the results with both techniques strongly suggests that G5 dendrimers interact strongly with the acyl chains of the membrane.

Further evidence for localization of G5 and G7 dendrimers inside the hydrophobic core of the lipid bilayer comes from ^{14}N spectroscopy (Figure 3.7), which suggests that neither dendrimer has a significant effect on the electric field surrounding the choline group in the lipid headgroup, since the ^{14}N ν_Q reported for all the samples studied (a pure DMPC lipid mixture, a lipid and G5 PAMAM dendrimer mixture, and a lipid and G7 PAMAM dendrimer mixture) were similar. Since the ^{14}N nucleus is typically affected by ligand interactions with the phosphate group (47-48) this result also suggests neither dendrimer interacts strongly with the phosphate group as well. The absence of a strong

electrostatic interaction of the dendrimer with the phosphate group is further corroborated by ^{31}P NMR as little perturbation of either the isotropic chemical shift under MAS (Figure 3.8) or the static line shape can be detected. Since the MLV samples were hydrated for ~ 2 days before starting experimental measurements, and equilibrate at a chosen temperature for at least 30 minutes prior to each NMR measurement, and NMR experiments typically lasted for few hours (^{31}P or ^{14}N NMR) to a day (2D R-PDLF), the location of dendrimers in the hydrophobic core of lipids bilayers is likely not a kinetic trap. Taken together, these results indicate that both the G5 and G7 dendrimers can occupy a thermodynamically stable position in the interior of zwitterionic lipid bilayer stabilized mainly by hydrophobic interactions. Interactions with the charged headgroups play a less role in membrane binding.

3.5.1 Relevance of our results to the in vivo behavior of dendrimers

It is important to note that the samples in this study were prepared by coincubating the dendrimers and lipid in organic solvent before the formation of the bilayer, rather than adding the dendrimers in aqueous solution after the bilayers have formed. Therefore, our experimental observations do not rule out the possibility of a kinetic barrier to dendrimer's insertion from water phase to the hydrophobic core of bilayers. Nevertheless, both experimental and computational studies have suggested that while dendrimers may initially bind to the surface of the bilayer they eventually deeply insert into the bilayer at equilibrium. Notably, electron paramagnetic resonance (EPR) studies done on samples where dendrimers were not coincubated with dendrimers yield similar results, showing a restriction of lipid tail motions and an insertion of dendrimer particles into zwitterionic vesicle lipid bilayers (27). Successive scans in differential

scanning calorimetry studies on G3 dendrimers show changes in the gel to liquid crystalline phase transition that was linked to the progressive insertion of the dendrimer into the bilayer (26). Similarly, mesoscopic dynamics simulations of dendrimer and lipid systems argue for the eventual insertion of the dendrimer into the bilayer, showing an interaction of the dendrimer with both leaflets of the bilayer (17, 49).

3.5.2 Impact of dendrimer's insertion on Membrane Dynamics

This model is helpful understanding the changes in membrane structure that occur upon dendrimer binding. Both the G5 and G7 dendrimers decreased the flexibility of the acyl chains of DMPC throughout the length of the acyl chain (fig. 6) in agreement with previous EPR studies (28, 50). The insertion of a guest molecule can either create order or disorder in the membrane depending on the depth of insertion and flexibility of the guest molecule. If the guest molecule penetrates only partially into the lipid bilayer, a void space is created beneath the point of insertion. The molecular motions of the acyl chains in this void region are increased because of the loss of the steric interactions with the surrounding phospholipids that suppress the natural rotation about the carbon-carbon bonds that occurs in lipid molecules (51-52). This effect is largely responsible for the increase in membrane disorder in the acyl chain seen with amphipathic molecules, such as most antimicrobial peptides, that penetrate only to the polar glycerol region of the phospholipids (52-53). It is also responsible for the membrane thinning effect commonly seen with these molecules as the bilayer compensates for the creation of the unfavorable void volume by reducing its thickness (54). On the other hand, the areas of the lipid molecule directly contacting the guest molecule are expected to be more ordered than a pure bilayer sample as the guest molecule generally interferes with the motion of the acyl

chains. In our sample, we expect the majority of dendrimers to be fully inserted into the lipid bilayers, so that the rigidifying effect of the dendrimer guest molecule would dominate. Furthermore, it is probable that lipid tails intercalate into the dendrimer molecule, increasing the number of lipid molecules in direct contact with the dendrimer. The effect was dependent on the size of the dendrimer with the $S_{|CH|}$ values of the G5 dendrimer sample consistently higher than those of the G7 dendrimer sample, indicating the G5 dendrimer has a greater impact on the dynamics of the interior of the bilayer, most likely because the congested surface of the G7 dendrimer restricts the intercalation of the acyl chains (De Gennes close packing) (55). It should be noted that the local increase in lipid order that occurs in the vicinity of the dendrimer may be compensated for by a global decrease in membrane thickness in the surrounding areas of the bilayer caused by the mismatch between the thickness of the flattened dendrimer and the lipid bilayer, as frequently observed in AFM studies (8).

From the headgroup order parameters, we conclude that the orientation of the P^-—N^+ dipole moves only slightly closer to the bilayer plane, indicating that the surface charge of the lipid bilayer was not significantly affected by the presence of dendrimer, in agreement with the ^{31}P and ^{14}N results. In an atomistic molecular dynamics study of dendrimers, Kelly et al. compared G3 dendrimers terminated with acetamide functional groups (G3-Ac), G3 dendrimers terminated with carboxylate functional groups (G3-COO^-), and unfunctionalized G3 dendrimers terminated with amine moieties (G3-NH_3^+) (9). They found that G3-NH_3^+ dendrimers were able to penetrate the most deeply into the bilayer and interact with both the glycerol atoms as well as the phosphodiester moiety in the headgroup of the lipid. Since the amine groups of the dendrimer are likely hydrogen

bonded to the glycerol oxygen of the phospholipid, we conclude that changes in the order parameters from the lipid glycerol C-H groups are likely due to changes in the hydrogen bonding pattern between lipids, with hydrogen bonds between dendrimer functional groups and lipids partially replacing lipid-lipid intermolecular hydrogen bonds that occur in pure lipid bilayers.

The increase in acyl chain order throughout the length of the acyl chain therefore argues that both the G5 and G7 dendrimers is inserted deeply into the membrane, in agreement with the RFDR and NOESY results, which suggest the end of the acyl chains are proximate to the interior of the dendrimer, and the ^{31}P and ^{14}N NMR spectroscopy results, which show a lack of significant electrostatic interaction between the dendrimer and the lipid bilayer.

3.5.3 Implications for Dendrimer Induced Membrane Disruption

One of the most significant interactions of dendrimers with the cell membrane is the formation of nanoscale holes in the membrane, which is followed by the fragmentation of the membrane at higher concentrations. Several mechanisms are possible whereby nanoparticles induce membrane disruption as shown in Figure 3.9. Three distinct models of membrane disruption have been proposed based by dynamic light scattering, atomic force microscopy, patch clamping ,and isothermal calorimetry: *(1)* the abstraction of lipid vesicles enclosing dendrimers from the bilayer (as shown in Figure 3.9A) (11, 15), *(2)* the abstraction of micellar lipid and dendrimer structures (as shown in Figure 3.9B) (15, 56), *(3)* or a carpet mechanism of membrane disruption, which eventually leads to the abstraction of lipids and the formation of a toroidal pore or wormhole structure (as shown in Figure 3.9C) (18, 21, 23, 57-58).

The membrane fragmentation products that would be expected to be present according to models 1 and 2 did not occur at the concentrations of dendrimers used at this study, as shown by the absence of an isotropic peak in the ^{31}P spectra of any of the samples (see Figure 3.8). At higher concentrations (3 % molar ratio of dendrimer/lipid or ~90 wt. % dendrimer/lipid), however, ^{31}P NMR spectroscopy and dynamic light scattering membrane do show the fragmentation of the membrane into small vesicle-like structures. In addition, a notable increase order parameters in the lipid tail is observed (see Figures 3.4, 3.5 and 3.6) in the R-PDLF experiments, An increase in the order of the lipid tail ($S_{|CH|}$) would seem to argue for the model where dendrimers produce toroidal pore structures in the lipid bilayer, because of the way lipid tails appear to be crowded in the plane parallel to the bilayer normal (see Figure 3.9C). However, the $S_{|CH|}$ expected from wormhole perforations in the lipid bilayer are not necessarily larger or smaller than the $S_{|CH|}$ observed from lipids in an unperturbed lipid bilayer (59-60). In general, the C-H bonds of lipids in a toroidal pore will either be rigidified or made more flexible depending of a variety of factors including lateral lipid diffusion and the structure of the toroidal pore. However, the effects Wi et al. observed usually involved more of a broadening of the ^{2}H lineshape than changes in the ^{2}H order parameters. On the other hand, we observed a significant rigidification of lipid tails in the presence of dendrimers (59). Furthermore, in mesoscopic dynamics studies on PAMAM dendrimer induced pore formation it was found that dendrimer-induced toroidal pores increased lipid tail flexibility and did not rigidify lipid tails as we observed (49). Based on these considerations, membrane disruption by the formation of toroidal pores (model 3) is less

likely for purely zwitterionic bilayers than membrane disruption by membrane fragmentation (models 1 and 2).

A putative model of dendrimer-mediated membrane disruption at higher dendrimer concentrations in largely zwitterionic lipids can be made based on our results as well as previous experimental and theoretical experiments (fig. 10). The dendrimer first approaches the membrane, deforming in response to the electric potential of the membrane as shown by Kelly et al. (9). The dendrimer then binds the surface of the lipid bilayer and changes its conformation, spreading out into a pancake shape to bind as many lipids as possible (9, 61). As it does this it probably expulses water molecules that are bound inside the dendrimer molecule (2), and hydrogen bonds between the water molecules and the dendrimer are replaced with hydrogen bonds between lipids and the dendrimer. Now that the interior of the dendrimer is exposed to the lipid-water interface, it is more likely that the branches of the dendrimer may penetrate through the membrane and make contact with the opposite leaflet of the bilayer, as has been observed in coarse-grained molecular dynamics simulations by Lee et al (Fig 10A) (17, 49). As more branches of the dendrimer penetrate through the lipid bilayer, the dendrimer will completely insert into the lipid bilayer weakening the lipid-lipid interactions that stabilize the bilayer structure of the membrane. As more lipid-lipid interactions are replaced by dendrimer-lipid interactions, the bilayer weakens and eventually collapses and dendrimer filled lipid micelles are abstracted. Similar dendrimer filled micelle structures have been observed to form upon the addition of dendrimers to the amphipathic detergent sodium dodecyl sulfate (SDS) (56). Note that this model implies that enough dendrimers have to insert into the lipid bilayer to dendrimer-lipid interactions to overpower lipid-lipid

interactions. At the lower concentrations of dendrimers we studied, they interact with lipid bilayers according to the membrane insertion mechanism and not the dendrimer-lipid micelle abstraction mechanism. This means that either high concentrations of PAMAM dendrimers or the gradual build-up of dendrimers in the lipid bilayer over time might result in lipid bilayer disruption (Fig. 10B) (19).

Our results were obtained using with DMPC bilayers, which are zwitterionic like the majority of the lipids in the cell membranes. It is possible that the manner in which dendrimers will interact with lipid bilayer will change as the charge of the membrane is varied. In fact, isothermal titration calorimetry (ITC) studies have suggested that whereas PAMAM dendrimers' interactions with zwitterionic lipid bilayers are entropy driven, their interactions with charged lipid bilayers are driven instead by the favorable enthalpic electrostatic contribution to the binding energy (7, 25-26). In this case the dendrimer-filled vesicle (fig. 9a) and toroidal pore (fig. 9b) models of membrane disruption become more likely as the association of the dendrimer with the lipid headgroup becomes stronger than with the acyl chains.

3.6 Acknowledgements

We acknowledge Drs. Lisa Prevette, Ronald Soong, and Jiadi Xu for helpful discussion. The project was partially funded with federal funds from NIH, R01-EB005028.

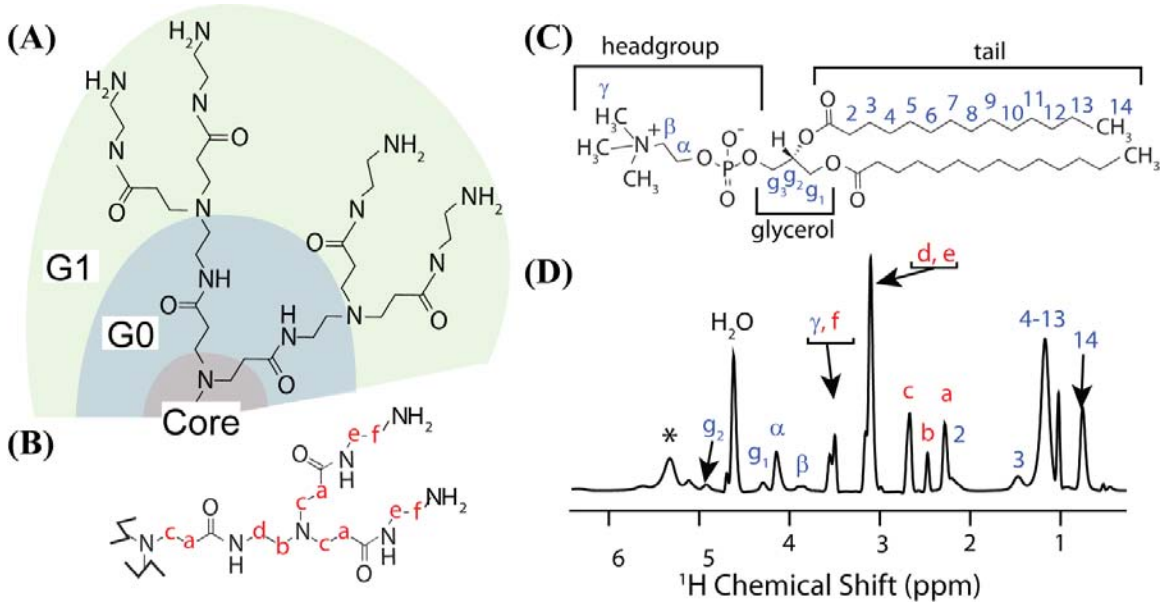

Figure 3.1 The molecular structures of PAMAM dendrimers and DMPC phospholipids. (A) One-half of a G1 PAMAM dendrimer. The generation number may be visually assessed by counting the number of forks per branch of the dendrimer, excluding the fork of the core ethylenediamine molecule. The core, zeroth, and first generation parts of the dendrimer are labeled. (B) A branch of the dendrimer with its carbon atoms labeled in red. (C) A DMPC molecule. (D) A ^{1}H MAS NMR spectrum of DMPC mixed with 0.1 mol % G5 PAMAM dendrimer (sample B2; see methods and materials); spinning sideband is indicated with an asterisk. The mixture was 50 % hydrated by weight. Proton resonances originating from the dendrimer and lipid are labeled in red and blue respectively; resonances were assigned based on previous NMR studies (39, 62).

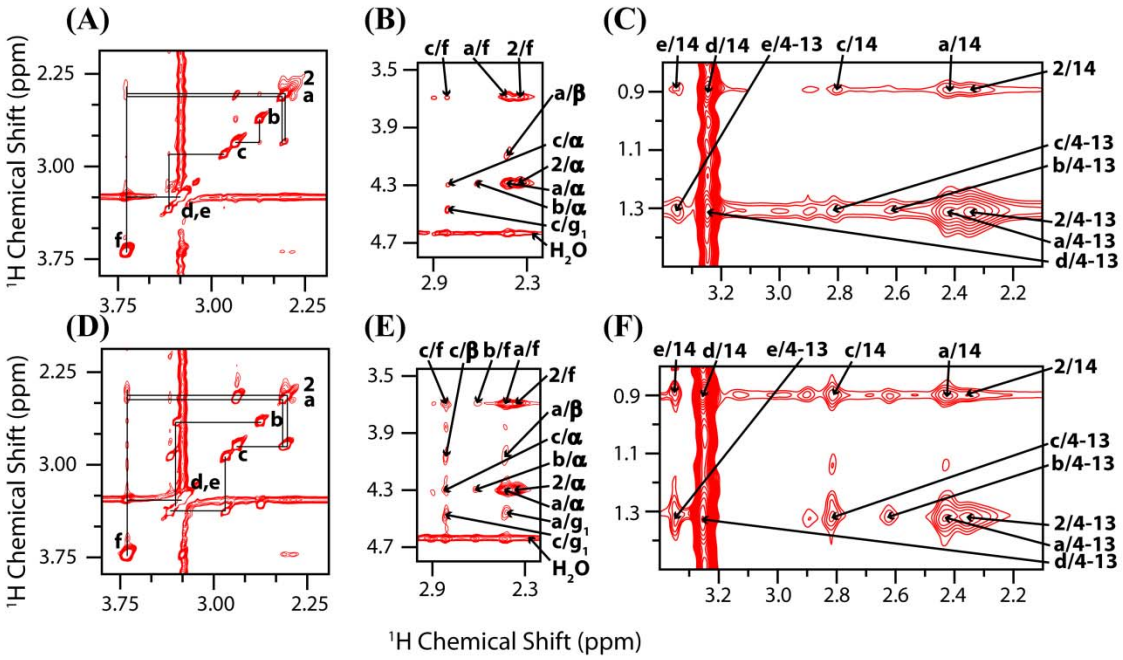

Figure 3.2 The 2D ^{1}H-^{1}H MAS NOESY and ^{1}H RFDR spectra of the dendrimer and lipid mixture (acquired on samples B1 and B2; see methods and materials). Different regions of the NOESY spectrum acquired with a 150 ms mixing time showing **(A)** dendrimer intramolecular crosspeaks, **(B)** dendrimer-lipid headgroup crosspeaks, and **(C)** dendrimer-lipid tail crosspeaks. Bottom: Different regions of the ^{1}H RFDR spectrum acquired with a 30 ms mixing time showing **(D)** dendrimer intramolecular crosspeaks, **(E)** dendrimer-lipid headgroup crosspeaks, and **(F)** dendrimer-lipid tail crosspeaks. The crosspeaks are numbered according to the scheme described in Figure 3.1.

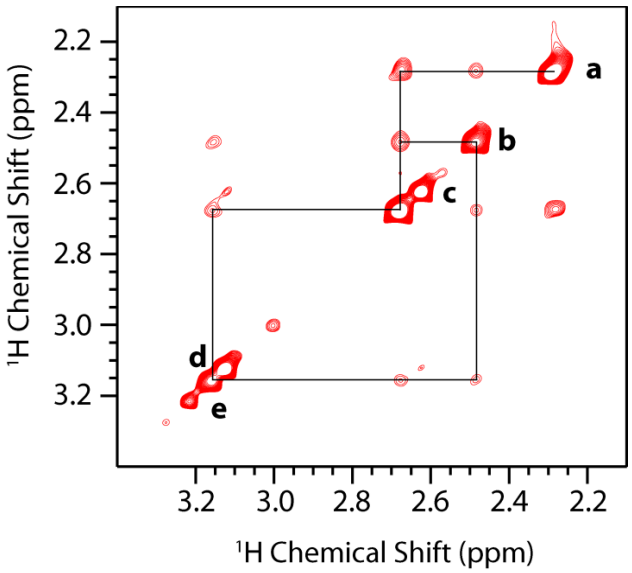

Figure 3.3 The ^{1}H-^{1}H MAS NOESY spectrum of 10 mg dendrimer dissolved in 45 µL 10 mM sodium phosphate buffer prepared at a pH of 7.3 (dendrimer in an aqueous environment). The spectrum was obtained in the manner described for the dendrimer-lipid samples but with a mixing time of 100 ms. A comparison of the relative intensities of the diagonal peaks and crosspeaks in this spectrum with the spectra shown in Figure 3.2A, 3.2B, and 3.2C suggests that there are more motions contributing to NOE relaxation when the dendrimer is in aqueous environment than when the dendrimer is in a lipid environment. Note that NOESY crosspeaks are more intense in this spectrum in spite of the shorter mixing time being used (100 ms as opposed to 150 ms).

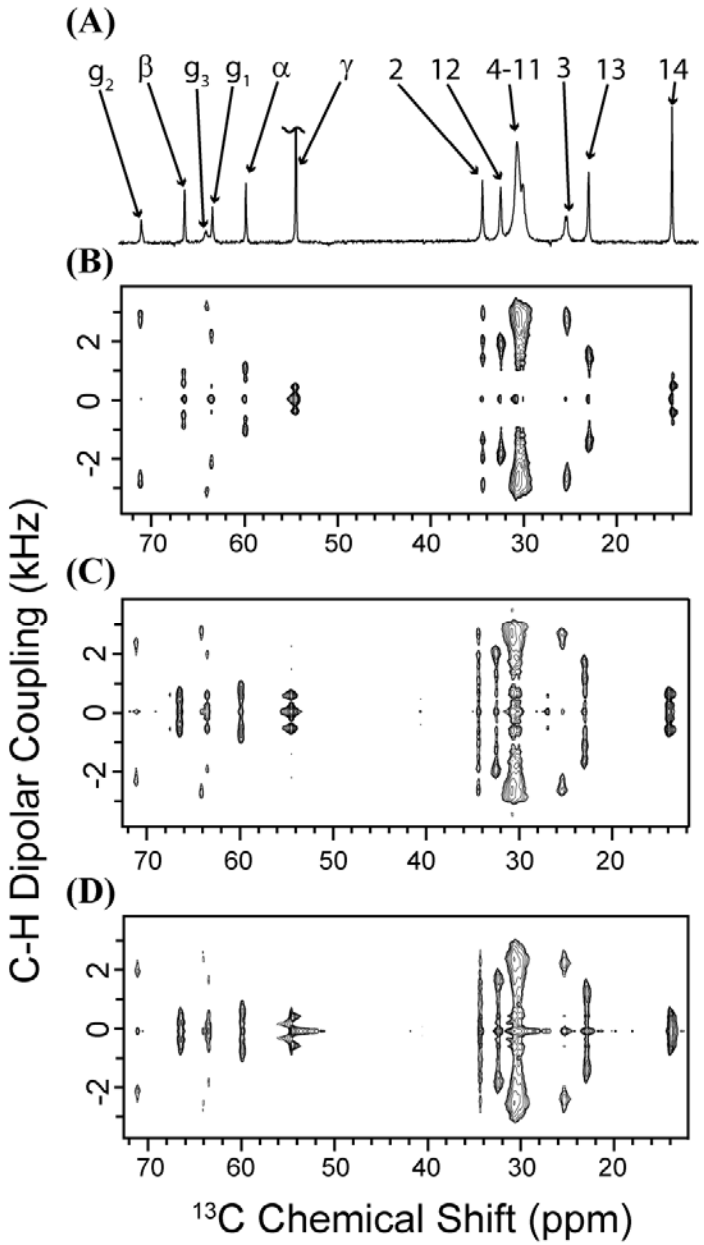

Figure 3.4 The R-PDLF spectra of DMPC MLVs containing dendrimers (acquired on samples A1-A3; see methods and materials). The $R18_1^7$ recoupling sequence during the t_1 period was used for recoupling the C-H dipolar coupling under MAS (35, 38). The scaling factor of this recoupling sequence is 0.315. **(A)** A 1D ^{13}C NMR spectrum on pure DMPC lipid bilayers. **(B)** 2D R-PDLF spectra of pure DMPC bilayers, **(C)** DMPC bilayers with 0.073 mole % (3 wt. %) G5 dendrimers, (D) and DMPC bilayers with 0.018 mole % (3 wt. %) G7 dendrimers.

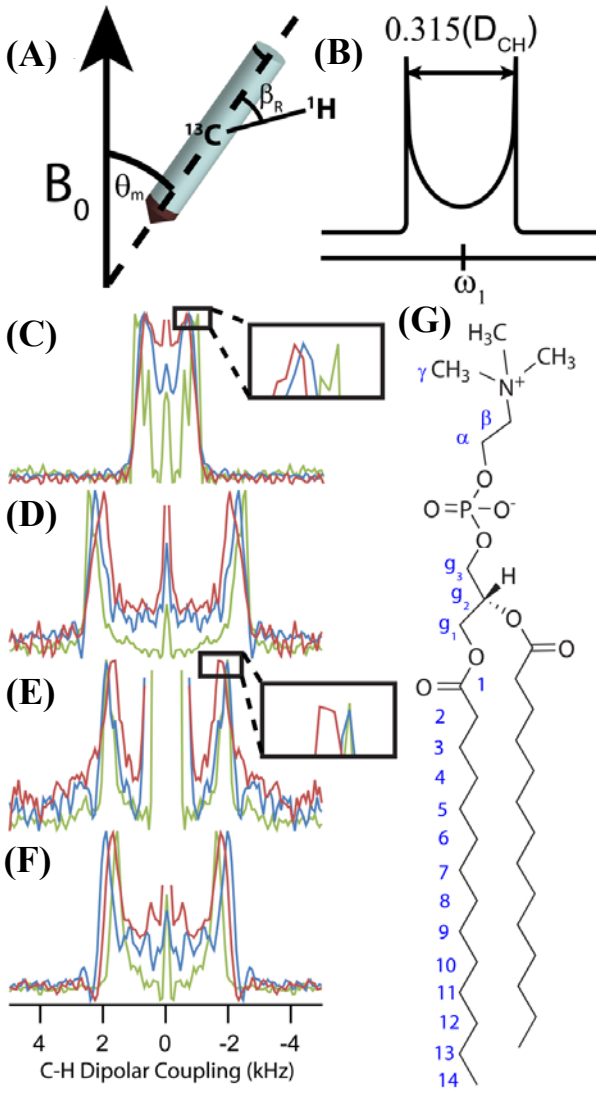

Figure 3.5 Selected C-H dipolar coupling slices of R-PDLF spectra show that dendrimers rigidify lipid tails and change lipid bilayer electrostatics (acquired on samples A1-A3; see methods and materials). (A) A rotor under MAS and the relationship between the rotor frame and the laboratory frame. Since the extent to which the transverse magnetization of protons evolve under the recoupled C-H dipolar coupling depends on the angle between the C-H bond vector and the long axis of the rotor (indicated as β_R here), a lineshape pattern with two "horns," or singularities, results in the dipolar coupling dimension. (B) A theoretical C-H dipolar coupling powder pattern produced in the indirect dimension of an R-PDLF spectrum, illustrating how the C-H dipolar coupling is measured. It is the distance between the two "horns" (mathematical singularities) multiplied by 1/0.315 (38). Also shown are the dipolar coupling slices for the control sample (in green), the G5 dendrimer associated sample (in blue) and the G7 associated sample (in red) for the (C) α carbon, (D) g_2 carbon, (E) g_1 carbon, and (F) 12 carbon. (G) The molecular structure of a DMPC molecule with its carbon atoms labeled for reference.

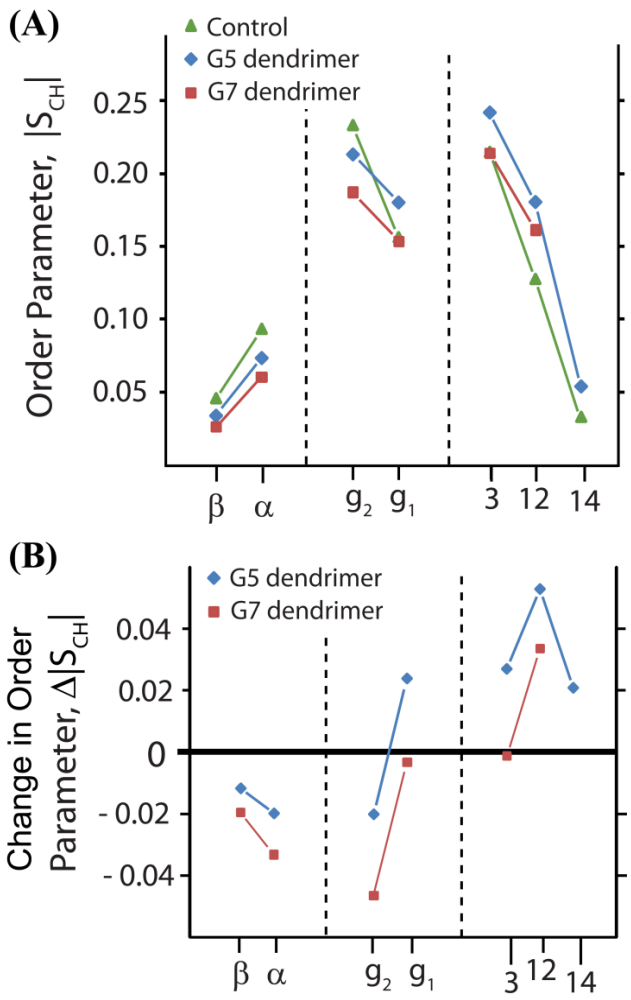

Figure 3.6 Order parameters show that dendrimers rigidify lipid tails and change lipid bilayer electrostatics (derived from R-PDLF spectra acquired on samples A1-A3; see methods and materials). (A) Order parameters determined from the experimentally measured ^{1}H-^{13}C dipolar couplings. The control, pure lipid sample order parameters are indicated in green, the G5 dendrimer associated order parameters are indicated in blue and the G7 dendrimer associated order parameters are indicated in red. (B) The changes in the order parameters recorded of the dendrimer associated samples relative to the pure lipid control sample.

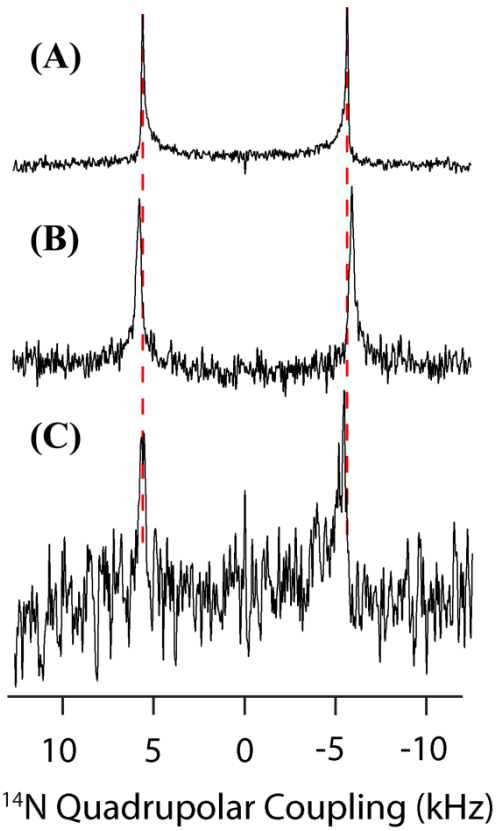

Figure 3.7 The ^{14}N NMR spectra of dendrimer and lipid samples acquired under static conditions. Acquired on samples A1-A3 (see methods and materials). (A) The DMPC ^{14}N NMR spectrum (the quadrupolar splitting, or ν_Q, is 11.2 kHz) with dashed lines for comparison with, (B) the ^{14}N NMR spectrum of the G5 dendrimer and DMPC mixture (ν_Q is 11.6 kHz) and, (C) the ^{14}N NMR spectrum of the G7 dendrimer and DMPC mixture (ν_Q is 11.1 kHz).

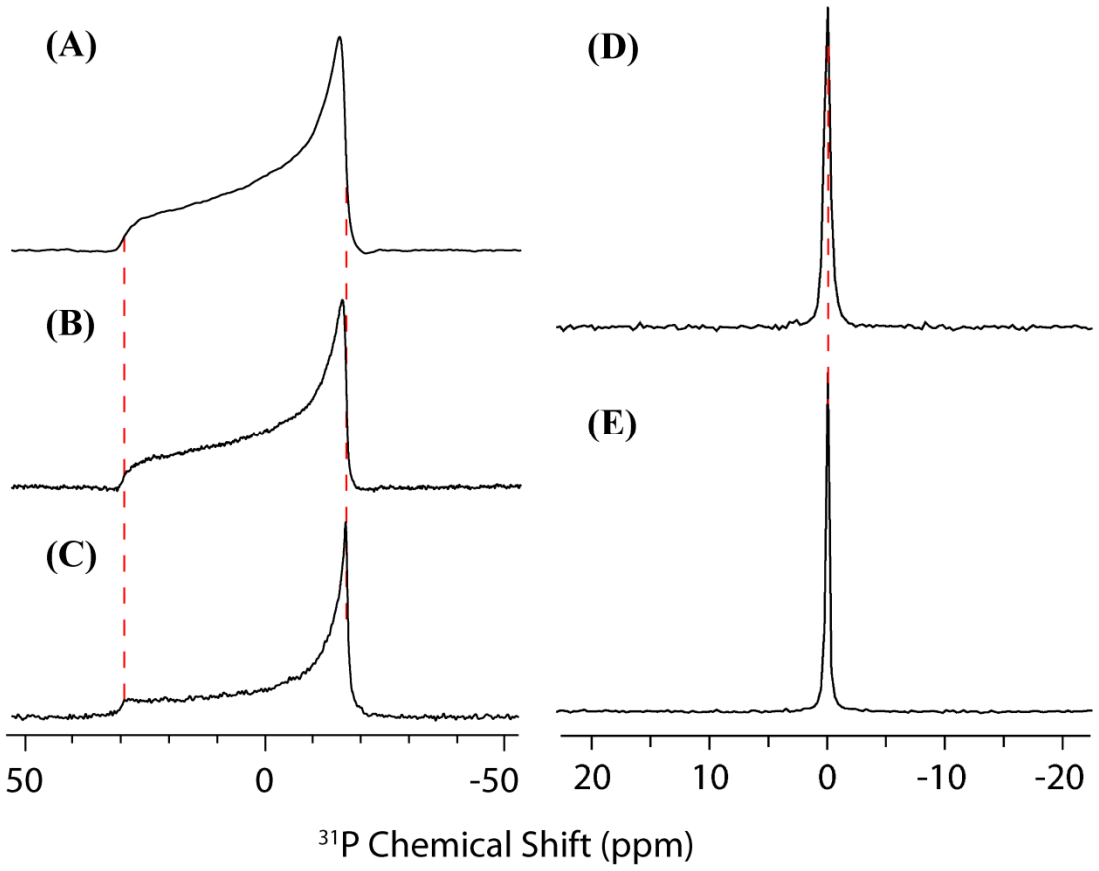

Figure 3.8 ^{31}P NMR spectra of dendrimer and lipid samples acquired under various conditions. Deionized water and lipid mixtures were used for (A-C) and samples B1 and B2 were used for (D-E). (A) The ^{31}P NMR spectrum acquired under static conditions of (A) pure DMPC MLVs (CSA span 46.2 ppm) (B) DMPC and G5 dendrimer (CSA span 46.8 ppm) (C) DMPC and G7 dendrimer (CSA span is 47.6 ppm). The ^{31}P NMR spectrum acquired under 10 kHz magic angle spinning (MAS) of (D) a DMPC and G5 PAMAM dendrimer and (E) a DMPC lipid sample. The samples used in (D) and (E) are hydrated to 50 wt. % by 0.1 M sodium phosphate buffer and the samples used in (A), (B), and (C) are hydrated to 50 wt. % by distilled, deionized water.

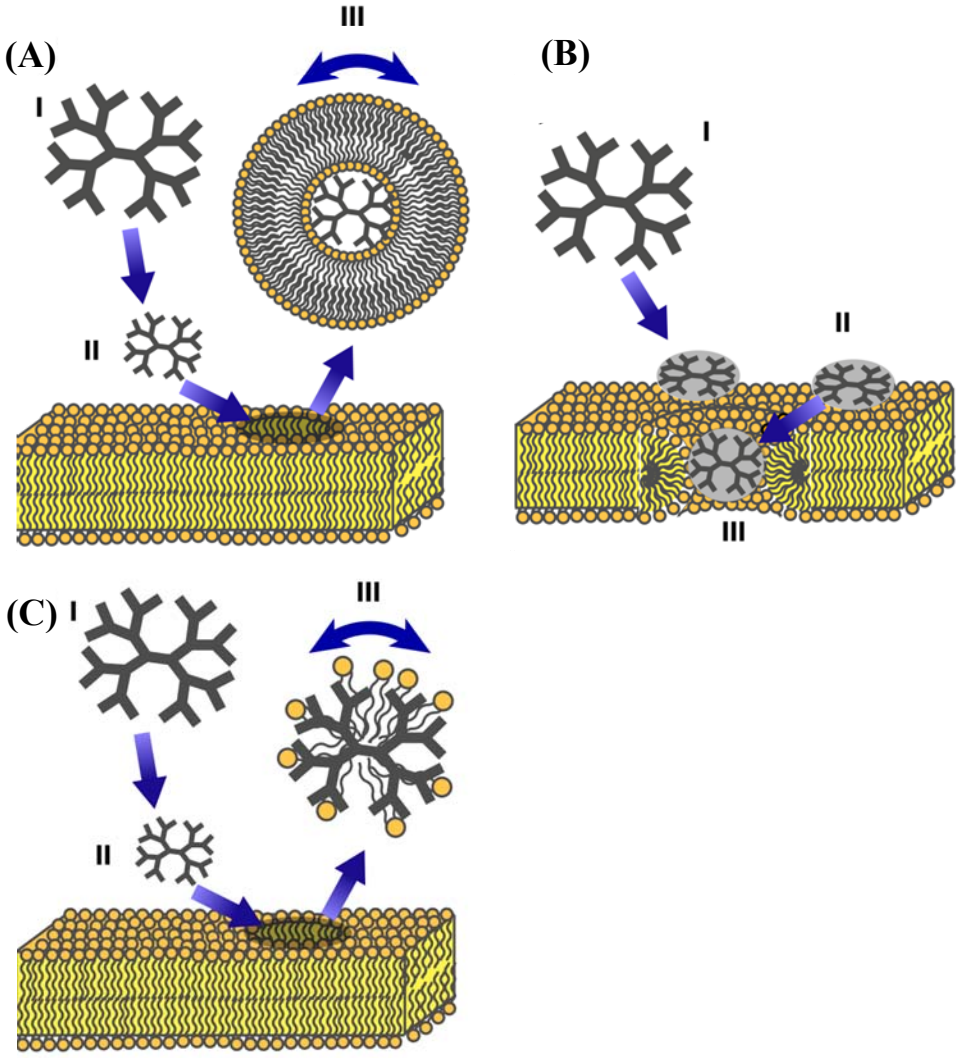

Figure 3.9 Likely models of dendrimer-lipid interaction. (A) A dendrimer-filled lipid vesicle model of lipid bilayer disruption. The dendrimer binds at the surface of the membrane causing a bending stress that is relieved by the formation of dendrimer filled micelles (11, 15). (B) Membrane disruption by the abstraction of micellar lipid and dendrimer structures from the lipid bilayer. This mechanism is similar to Model A except the lipid tails are intercalated into the interior with the headgroups associated with the charged amines of the dendrimer (15, 56). (C) A carpet model of dendrimer-filled lipid bilayer disruption (23, 58). Surface binding of the dendrimer creates excess curvature in the membrane (18, 21), which is relieved by the formation of lipid-lined toroidal pores. After toroidal pores are eventually formed, there may more than one dendrimer inside the pore, although only one dendrimer is depicted here.

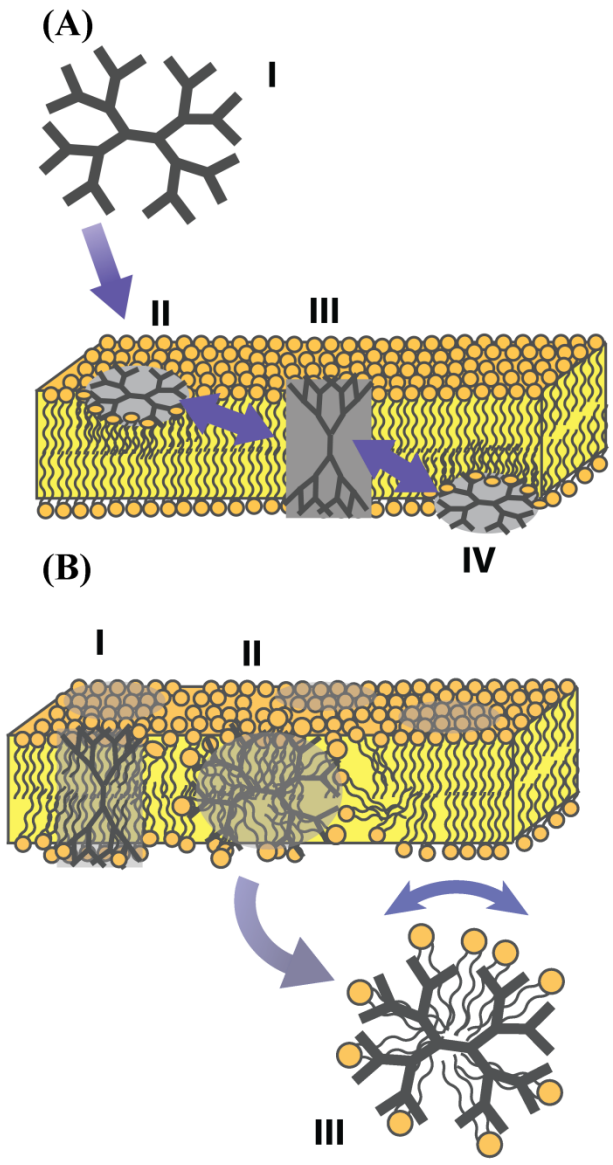

Figure 3.10 Plausible models of dendrimer-lipid interaction at low and high concentrations of dendrimer. (A) Model ofdendrimer-lipid interactions at low dendrimer concentrations. The dendrimer can traeverse the bilayer by first binding to the surface of the outer leaflet, inserting into the membrane making contacts at both leaflets, and finally dissociating from the membrane on the opposite side. (B) At higher dendrimer concentrations the structural integrity of the membrane is weakened and dendrimer-lipid micelles are formed.

3.7 References

1. Topp, A., B. J. Bauer, J. W. Klimash, R. Spindler, D. A. Tomalia, and E. J. Amis. 1999. Probing the Location of the Terminal Groups of Dendrimers in Dilute Solution. Macromolecules 32:7226-7231.

2. Lee, H., J. R. Baker, and R. G. Larson. 2006. Molecular dynamics studies of the size, shape, and internal structure of 0% and 90% acetylated fifth-generation polyamidoamine dendrimers in water and methanol. J. Phys. Chem. B 110:4014-4019.

3. Wooley, K. L., C. A. Klug, K. Tasaki, and J. Schaefer. 1997. Shapes of Dendrimers from Rotational-Echo Double-Resonance NMR. J. Am. Chem. Soc. 119:53-58.

4. Jiang, Y. H., P. Emau, J. S. Cairns, L. Flanary, W. R. Morton, T. D. McCarthy, and C. C. Tsai. 2005. SPL7013 gel as a topical microbicide for prevention of vaginal transmission of SHIV89.6P in macaques. AIDS Res. Hum. Retroviruses 21:207-213.

5. Bourne, N., L. R. Stanberry, E. R. Kern, G. Holan, B. Matthews, and D. I. Bernstein. 2000. Dendrimers, a new class of candidate topical microbicides with activity against herpes simplex virus infection. Antimicrob. Agents. Ch. 44:2471-2474.

6. Kukowska-Latallo, J. F., K. A. Candido, Z. Cao, S. S. Nigavekar, I. J. Majoros, T. P. Thomas, L. P. Balogh, M. K. Khan, and J. R. Baker, Jr. 2005. Nanoparticle Targeting of Anticancer Drug Improves Therapeutic Response in Animal Model of Human Epithelial Cancer. Cancer Res. 65:5317-5324.

7. Kelly, C. V., M. G. Liroff, L. D. Triplett, P. R. Leroueil, D. G. Mullen, J. M. Wallace, S. Meshinchi, J. R. Baker, B. G. Orr, and M. M. B. Holl. 2009. Stoichiometry and Structure of Poly(amidoamine) Dendrimer-Lipid Complexes. ACS Nano 3:1886-1896.

8. Hong, S., P. R. Leroueil, E. K. Janus, J. L. Peters, M.-M. Kober, M. T. Islam, B. G. Orr, J. R. Baker, and M. M. Banaszak Holl. 2006. Interaction of Polycationic Polymers with Supported Lipid Bilayers and Cells: Nanoscale Hole Formation and Enhanced Membrane Permeability. Bioconjugate Chem. 17:728-734.

9. Kelly, C. V., P. R. Leroueil, E. K. Nett, J. M. Wereszczynski, J. R. Baker, B. G. Orr, M. M. B. Holl, and I. Andricioaei. 2008. Poly(amidoamine) dendrimers on lipid bilayers I: Free energy and conformation of binding. J. Phys. Chem. B 112:9337-9345.

10. Pantos, A., D. Tsiourvas, G. Nounesis, and C. M. Paleos. 2005. Interaction of functional dendrimers with multilamellar liposomes: Design of a model system for studying drug delivery. Langmuir 21:7483-7490.

11. Mecke, A., S. Uppuluri, T. M. Sassanella, D. K. Lee, A. Ramamoorthy, J. R. Baker, B. G. Orr, and M. M. B. Holl. 2004. Direct observation of lipid bilayer disruption by poly(amidoamine) dendrimers. Chem. Phys. Lipids 132:3-14.

12. Tsogas, I., T. Theodossiou, Z. Sideratou, C. M. Paleos, H. Collet, J. C. Rossi, B. Romestand, and A. Cornmeyras. 2007. Interaction and transport of poly(L-lysine) dendrigrafts through liposomal and cellular membranes: The role of generation and surface functionalization. Biomacromolecules 8:3263-3270.

13. Quintana, A., E. Raczka, L. Piehler, I. Lee, A. Myc, I. Majoros, A. Patri, T. Thomas, J. Mulé, and J. Baker. 2002. Design and Function of a Dendrimer-Based Therapeutic Nanodevice Targeted to Tumor Cells Through the Folate Receptor. Pharm. Res. 19:1310-1316.

14. Hong, S., A. U. Bielinska, A. Mecke, B. Keszler, J. L. Beals, X. Shi, L. Balogh, B. G. Orr, J. R. Baker, and M. M. Banaszak Holl. 2004. Interaction of Poly(amidoamine) Dendrimers with Supported Lipid Bilayers and Cells: Hole Formation and the Relation to Transport. Bioconjugate Chem. 15:774-782.

15. Mecke, A., I. J. Majoros, A. K. Patri, J. R. Baker, M. M. B. Holl, and B. G. Orr. 2005. Lipid bilayer disruption by polycationic polymers: The roles of size and chemical functional group. Langmuir 21:10348-10354.

16. Kelly, C. V., P. R. Leroueil, B. G. Orr, M. M. B. Holl, and I. Andricioaei. 2008. Poly(amidoamine) dendrimers on lipid bilayers II: Effects of bilayer phase and dendrimer termination. J. Phys. Chem. B 112:9346-9353.

17. Lee, H., and R. G. Larson. 2008. Coarse-grained molecular dynamics studies of the concentration and size dependence of fifth- and seventh-generation PAMAM dendrimers on pore formation in DMPC bilayer. J. Phys. Chem. B 112:7778-7784.

18. Lee, H., and R. G. Larson. 2008. Lipid bilayer curvature and pore formation induced by charged linear polymers and dendrimers: The effect of molecular shape. J. Phys. Chem. B 112:12279-12285.

19. Chen, J. M., J. A. Hessler, K. Putchakayala, B. K. Panama, D. P. Khan, S. Hong, D. G. Mullen, S. C. DiMaggio, A. Som, G. N. Tew, A. N. Lopatin, J. R. Baker, M. M. B. Holl, and B. G. Orr. 2009. Cationic Nanoparticles Induce Nanoscale Disruption in Living Cell Plasma Membranes. J. Phys. Chem. B 113:11179-11185.

20. Ginzburg, V. V., and S. Balijepailli. 2007. Modeling the thermodynamics of the interaction of nanoparticles with cell membranes. Nano Lett. 7:3716-3722.

21. Zhang, Z.-Y., and B. D. Smith. 2000. High-Generation Polycationic Dendrimers Are Unusually Effective at Disrupting Anionic Vesicles: Membrane Bending Model. Bioconjugate Chem. 11:805-814.

22. Betley, T. A., M. M. B. Holl, B. G. Orr, D. R. Swanson, D. A. Tomalia, and J. R. Baker. 2001. Tapping mode atomic force microscopy investigation of poly(amidoamine) dendrimers: Effects of substrate and pH on dendrimer deformation. Langmuir 17:2768-2773.

23. Leroueil, P. R., S. Hong, A. Mecke, J. R. Baker, B. G. Orr, and M. M. Banaszak Holl. 2007. Nanoparticle Interaction with Biological Membranes: Does Nanotechnology Present a Janus Face? Acc. Chem. Res. 40:335-342.

24. Braun, C. S., J. A. Vetro, D. A. Tomalia, G. S. Koe, J. G. Koe, and C. R. Middaugh. 2005. Structure/function relationships of polyamidoamine/DNA dendrimers as gene delivery vehicles. J. Pharm. Sci. 94:423-436.

25. Gardikis, K., S. Hatziantoniou, K. Viras, M. Wagner, and C. Demetzos. 2006. A DSC and Raman spectroscopy study on the effect of PAMAM dendrimer on DPPC model lipid membranes. Int. J. Pharm. 318:118-123.

26. Klajnert, B., and R. M. Epand. 2005. PAMAM dendrimers and model membranes: Differential scanning calorimetry studies. Int. J. Pharm. 305:154-166.

27. Ottaviani, M. F., R. Daddi, M. Brustolon, N. J. Turro, and D. A. Tomalia. 1999. Structural modifications of DMPC vesicles upon interaction with poly(amidoamine) dendrimers studied by CW-electron paramagnetic resonance and electron spin-echo techniques. Langmuir 15:1973-1980.

28. Ottaviani, M. F., P. Matteini, M. Brustolon, N. J. Turro, S. Jockusch, and D. A. Tomalia. 1998. Characterization of starburst dendrimers and vesicle solutions and their interactions by CW- and pulsed-EPR, TEM, and dynamic light scattering. J. Phys. Chem. B 102:6029-6039.

29. Hallock, K. J., D.-K. Lee, and A. Ramamoorthy. 2003. MSI-78, an Analogue of the Magainin Antimicrobial Peptides, Disrupts Lipid Bilayer Structure via Positive Curvature Strain. Biophys. J. 84:3052-3060.

30. Ludtke, S. J., K. He, W. T. Heller, T. A. Harroun, L. Yang, and H. W. Huang. 1996. Membrane pores induced by magainin. Biochemistry 35:13723-13728.

31. Smith, P. E. S., J. R. Brender, and A. Ramamoorthy. 2009. Induction of Negative Curvature as a Mechanism of Cell Toxicity by Amyloidogenic Peptides: The Case of Islet Amyloid Polypeptide. J. Am. Chem. Soc. 131:4470-4478.

32. Nanga, R. P. R., J. R. Brender, S. Vivekanandan, N. Popovych, and A. Ramamoorthy. 2009. NMR Structure in a Membrane Environment Reveals

Putative Amyloidogenic Regions of the SEVI Precursor Peptide $PAP_{248-286}$. J. Am. Chem. Soc. 131:17972-17979.

33. Majoros, I. J., B. Keszler, S. Woehler, T. Bull, and J. R. Baker. 2003. Acetylation of poly(amidoamine) dendrimers. Macromolecules 36:5526-5529.

34. Cakara, D., J. Kleimann, and M. Borkovec. 2003. Microscopic Protonation Equilibria of Poly(amidoamine) Dendrimers from Macroscopic Titrations. Macromolecules 36:4201-4207.

35. Zhao, X., M. Eden, and M. H. Levitt. 2001. Recoupling of heteronuclear dipolar interactions in solid-state NMR using symmetry-based pulse sequences. Chem. Phys. Lett. 342:353-361.

36. Nakai, T., and T. Terao. 1992. Measurements of heteronuclear dipolar powder patterns due only to directly bonded couplings. Magn. Reson. Chem. 30:42-44.

37. Morris, G. A., and R. Freeman. 1979. Enhancement of Nuclear Magnetic-Resonance Signals by Polarization Transfer. J. Am. Chem. Soc. 101:760-762.

38. Dvinskikh, S. V., H. Zimmermann, A. Maliniak, and D. Sandstrom. 2004. Measurements of motionally averaged heteronuclear dipolar couplings in MAS NMR using R-type recoupling. J. Magn. Reson. 168:194-201.

39. Dvinskikh, S. V., V. Castro, and D. Sandstrom. 2005. Efficient solid-state NMR methods for measuring heteronuclear dipolar couplings in unoriented lipid membrane systems. Phys. Chem. Chem. Phys. 7:607-613.

40. Macdonald, P. M., J. Leisen, and F. M. Marassi. 1991. Response of Phosphatidylcholine in the Gel and Liquid-Crystalline States to Membrane-Surface Charges. Biochemistry 30:3558-3566.

41. Ulrich, A. S., and A. Watts. 1994. Molecular Response of the Lipid Headgroup to Bilayer Hydration Monitored by ^{2}H-NMR. Biophys. J. 66:1441-1449.

42. Bechinger, B., and J. Seelig. 1991. Conformational-Changes of the Phosphatidylcholine Headgroup due to Membrane Dehydration - A ^{2}H-NMR Study. Chem. Phys. Lipids 58:1-5.

43. Yamamoto, K., R. Soong, and A. Ramamoorthy. 2009. Comprehensive Analysis of Lipid Dynamics Variation with Lipid Composition and Hydration of Bicelles Using Nuclear Magnetic Resonance (NMR) Spectroscopy. Langmuir 25:7010-7018.

44. Aucoin, D., D. Camenares, X. Zhao, J. Jung, T. Sato, and S. O. Smith. 2009. High-resolution ^{1}H MAS RFDR NMR of biological membranes. J. Magn. Reson. 197:77-86.

45. Huster, D., K. Arnold, and K. Gawrisch. 1999. Investigation of lipid organization in biological membranes by two-dimensional nuclear overhauser enhancement spectroscopy. J. Phys. Chem. B 103:243-251.

46. Yau, W. M., and K. Gawrisch. 2000. Lateral lipid diffusion dominates NOESY cross-relaxation in membranes. J. Am. Chem. Soc. 122:3971-3972.

47. Rothgeb, T. M., and E. Oldfield. 1981. ^{14}N Nuclear Magnetic-Resonance Spectroscopy as a Probe of Lipid Bilayer Headgroup Structure. J. Biol. Chem. 256:6004-6009.

48. Santos, J. S., D. K. Lee, and A. Ramamoorthy. 2004. Effects of antidepressants on the conformation of phospholipid headgroups studied by solid-state NMR. Magn. Reson. Chem. 42:105-114.

49. Lee, H., and R. G. Larson. 2006. Molecular dynamics simulations of PAMAM dendrimer-induced pore formation in DPPC bilayers with a coarse-grained model. J. Phys. Chem. B 110:18204-18211.

50. Ottaviani, M. F., P. Favuzza, B. Sacchi, N. J. Turro, S. Jockusch, and D. A. Tomalia. 2002. Interactions between starburst dendrimers and mixed DMPC/DMPA-Na vesicles studied by the spin label and the spin probe techniques, supported by transmission electron microscopy. Langmuir 18:2347-2357.

51. Barry, J., M. Fritz, J. R. Brender, P. E. S. Smith, D.-K. Lee, and A. Ramamoorthy. 2009. Determining the Effects of Lipophilic Drugs on Membrane Structure by Solid-State NMR Spectroscopy: The Case of the Antioxidant Curcumin. J. Am. Chem. Soc. 131:4490-4498.

52. Henzler-Wildman, K. A., G. V. Martinez, M. F. Brown, and A. Ramamoorthy. 2004. Perturbation of the hydrophobic core of lipid bilayers by the human antimicrobial peptide LL-37. Biochemistry 43:8459-8469.

53. Thennarasu, S., D. K. Lee, A. Poon, K. E. Kawulka, J. C. Vederas, and A. Ramamoorthy. 2005. Membrane permeabilization, orientation, and antimicrobial mechanism of subtilosin A. Chem. Phys. Lipids 137:38-51.

54. Mecke, A., D. K. Lee, A. Ramamoorthy, B. G. Orr, and M. M. B. Holl. 2005. Membrane thinning due to antimicrobial peptide binding: An atomic force microscopy study of MSI-78 in lipid bilayers. Biophys. J. 89:4043-4050.

55. Tomalia, D. A. 2005. Birth of a new macromolecular architecture: dendrimers as quantized building blocks for nanoscale synthetic polymer chemistry. Prog. Polym. Sci. 30:294-324.

56. Cheng, Y. Y., Q. L. Wu, Y. W. Li, J. J. Hu, and T. W. Xu. 2009. New Insights into the Interactions between Dendrimers and Surfactants: 2. Design of New Drug

Formulations Based on Dendrimer-Surfactant Aggregates. J. Phys. Chem. B 113:8339-8346.

57. Oren, Z., and Y. Shai. 1998. Mode of action of linear amphipathic alpha-helical antimicrobial peptides. Biopolymers 47:451-463.

58. Bechinger, B., and K. Lohner. 2006. Detergent-like actions of linear amphipathic cationic antimicrobial peptides. Biochim. Biophys. Acta 1758:1529-1539.

59. Wi, S., and C. Kim. 2008. Pore structure, thinning effect, and lateral diffusive dynamics of oriented lipid membranes interacting with antimicrobial peptide protegrin-1: ^{31}P and ^{2}H solid-state NMR study. J. Phys. Chem. B 112:11402-11414.

60. Sengupta, D., H. Leontiadou, A. E. Mark, and S. J. Marrink. 2008. Toroidal pores formed by antimicrobial peptides show significant disorder. Biochim. Biophys. Acta 1778:2308-2317.

61. Mecke, A., I. Lee, J. R. Baker, M. M. B. Holl, and B. G. Orr. 2004. Deformability of poly(amidoamine) dendrimers. Eur. Phys. J. E 14:7-16.

62. Yang, W., Y. Li, Y. Cheng, Q. Wu, L. Wen, and T. Xu. 2009. Evaluation of phenylbutazone and poly(amidoamine) dendrimers interactions by a combination of solubility, 2D-NOESY NMR, and isothermal titration calorimetry studies. J. Pharm. Sci. 98:1075-1085.

CHAPTER 4

DEVELOPMENT OF NMR METHODS FOR HIGH RESOLUTION MOLECULAR IMAGING OF MEMBRANE ASSOCIATED MOLECULES*

4.1 Summary

The structural biology of biomembranes and the molecules that associate with them has rapidly evolved into a new frontier of science. Although there are still a few major challenges, separated local field (SLF) NMR spectroscopy has become an invaluable tool in obtaining structural images of membrane proteins under physiological conditions. Recent studies have demonstrated the use of rotating-frame SLF techniques to accurately measure anisotropic interactions between NMR active nuclei that contain structural information. Although these techniques can accurately measure strong heteronuclear dipolar couplings between directly bonded nuclei, all weak dipolar couplings are suppressed. On the other hand, weak heteronuclear dipolar couplings can be measured using laboratory-frame SLF experiments, but only at the expense of spectral resolution for strongly dipolar coupled spins. In the present study, we implemented 2D PELF (proton-evolved local-field) pulse sequences using either COMPOZER-CP (COMPOsite ZERo – Cross Polarization) or WIM (windowless isotropic mixing) for magnetization transfer. These PELF sequences can be used for the measurement of a broad range of heteronuclear dipolar couplings, allowing for a complete mapping of biomolecule dynamics in a lipid bilayer environment. Results suggest that the PELF based experimental approaches will have a profound impact on solid-state NMR

* Reproduced in part with permission from Soong, R., P.E.S. Smith, J. Xu, K. Yamamoto, S.-C. Im, L. Waskell, and A. Ramamoorthy. 2010. Proton-Evolved Local-Field Solid-State NMR Studies of Cytochrome b5 Embedded in Bicelles, Revealing both Structural and Dynamical Information. J. Am. Chem. Soc. 132: 5779-5788. Copyright 2010 American Chemical Society

spectroscopy of membrane proteins and other membrane-associated molecules in aligned media such as bicelles. However, the extraction of structural and dynamical information via NMR spectroscopy also requires assigning NMR resonances to the correct chemical sites of a molecule. To that end, a modification was made to the SLF pulse sequence which allows resonance assignment. A sophisticated multidimensional heteronuclear correlation NMR experiment is demonstrated that will enable the assignment of NMR resonances. Although the focus of this project is analyzing membrane protein structure and dynamics, the techniques developed can be applied to study the structure and dynamics of any biomembrane system.

4.2 Introduction

Membrane proteins, which constitute a third of all proteins in nature, regulate and direct a host of important cellular processes, ranging from transport of nutrients to generation of energy. Membrane proteins exhibit molecular motions on a wide range of time-scales under physiological conditions and insight into their motions is the key to understanding their functions. Molecular motions on the order of milliseconds are frequently observed in many essential and fascinating biological processes ranging from ligand binding to enzyme catalysis (1-4). Fast timescale side chain dynamics can provide clues into the mechanism by which ions migrate through membrane protein channels. Many membrane-associated enzymes, such as microsomal cytochrome P450, exhibit dynamic structural plasticity that enables the binding of substrates with various sizes and stereochemistry (5-6). Over the years, significant efforts have been devoted to understand the intricate molecular dynamics of soluble proteins; however, complete characterization of membrane protein dynamics continues to be a challenge (7-14). In principle, solid-

state NMR spectroscopy is a versatile tool for probing molecular dynamics occurring on timescales that vary from picoseconds (bond libration) to days (protein aggregation). These motions often influence various NMR observables such as chemical shift anisotropy, dipolar coupling and quadrupole coupling. Standard high-resolution solution NMR techniques have provided valuable insights into membrane protein structure-function relationships, but information regarding protein dynamics in lipid bilayers remains elusive (7-11, 15). The slow tumbling rate of most lipid membrane systems leads to various undesirable line broadening effects that make solution NMR techniques not applicable. Therefore, most solution NMR studies of membrane protein are restricted to proteins reconstituted in detergent micelles in cases where they may retain their functions and tumble rapidly enough to average out various undesirable line broadening effects. However, the dynamics observed in these systems can be different from those in a lipid bilayer environment. Solid-state NMR can overcome the undesirable line broadening effects associated with membrane proteins in lipid bilayers. High-resolution solid-state NMR requires the sample to be mechanically aligned or spun at the magic angle (54.7°) relative to the external magnetic field direction to suppress the line-broadening effects associated with nuclear spin interactions and allow for the reconstitution and study of membrane proteins in their native environment (16-19).

Separated local field (SLF) spectroscopy of aligned samples holds a great promise as a practical tool for studying membrane proteins in lipid bilayers (20-23). In these experiments, resonances from the different chemical sites are separated and the local field at each chemical site, which results from dipolar coupling to other nuclei and is a rich reservoir of structural and dynamical information, is studied individually. Alignment

media used for membrane protein structural studies can be made to closely mimic the native membrane environment and experiments can be carried out under physiological conditions (13, 24-26). Indeed, SLF has been successful in providing detailed structural information of α-helical membrane proteins in well-hydrated bilayer environments. A typical SLF spectrum correlates heteronuclear dipolar couplings between nuclei such as ^{15}N or ^{13}C and their directly bonded ^{1}H nuclei with the CSAs of ^{15}N or ^{13}C. Importantly, dipolar coupling and CSA are sensitive to the whole body motions of a protein, and are therefore capable of providing detailed dynamical and structural information (27-29). In order to extract dynamical and structural information from an SLF spectrum, one must be able to accurately measure a broad range of dipolar couplings between directly bonded spin pairs. However, in most commonly used rotating-frame SLF protocols, such as HIMSELF (Heteronuclear Isotropic Mixing Spin Exchange via Local Field), PISEMA (Polarization Inversion Spin Exchange at the Magic Angle) and SAMMY, various weak heteronuclear dipolar couplings are effectively suppressed in favor of simple spectral line-shape and improved resolution in the indirect dipolar coupling dimension (30-31). Laboratory-frame SLF experiments such as PELF (proton evolved local field) provide high sensitivity and resolution for loop regions, soluble domains, and mobile parts of membrane proteins such that structural and dynamical information can be extracted from these regions in a SLF spectrum (31-32). Also, PELF is capable of resolving a broad range of dipolar couplings from directly bonded spin pair, which is absolutely necessary for determining both dynamics and structures of membrane proteins. Despite these unique advantages, applications of PELF in structural biology remain to be established.

In this project, the use of COMPOZER-CP or WIM with the PELF to acquire highly resolved 2D NMR spectra in the solid-state is demonstrated. However, structure determination via NMR spectroscopy also requires that the different chemical sites can be identified according to their chemical shifts. Then their spatial relationship with each other can be correlated via nuclear spin interactions such as scalar couplings or dipolar couplings. If proton spin-diffusion can be tightly controlled, it can be used to generate correlations between proton spins without obscuring the resulting spectra. It is demonstrated that proton-mediated spin diffusion to generate correlations between the neighboring spins. The use of this PELF-MIX sequence enables resonance assignment and the complete determination of membrane proteins' structures.

4.3 Theory

NMR active nuclei (spins) have nonzero angular momentum. This angular momentum is analogous to the angular momentum of a macroscopic spinning object, but a nuclear spin is not "spinning" in the classical sense. The term "spin" is used because the observable behavior of the NMR active nuclei is similar to that of a spinning macroscopic object. The angular momentum of a nuclear spin is fixed by its spin quantum number, I, and is equal to $\hbar\sqrt{I(I+1)}$. According to the Heisenberg uncertainty principle, only the magnitudes of the total angular momentum and one of its directional components ($\hbar m_z$, where m_z, the secondary spin quantum number, can be any number I, I-1, ..., -I) can be known simultaneously.

Every spin has a magnetization proportional to its angular momentum. The constant of proportionality, γ, is called the gyromagnetic ratio. The z-component of a nucleus's angular is given by the operator, $\hat{I}_z$:

$$\hat{I}_z|I,m_z\rangle = \hbar m_z|I,m_z\rangle \quad [4.1]$$

Because magnetization is proportional to angular momentum, with a constant of proportionality, γ, the magnetic moment of a nuclear spin is given as:

$$\hat{\mu}_z|I,m_z\rangle = \gamma\hbar m_z|I,m_z\rangle \quad [4.2]$$

where $\hat{\mu}_z$ is the z-component magnetization operator. For a spin-$^1/_2$ nucleus ($s=^1/_2$), the eigenfunction with $m_z = +^1/_2$ is usually abbreviated $|\alpha\rangle$ and the eigenfunction with $m_z = -^1/_2$ is usually abbreviated $|\beta\rangle$. The potential energy (U) associated with orienting a magnetic dipole (such as a bar magnet) in a static magnetic field is given by:

$$U = -\boldsymbol{\mu} \cdot \mathbf{B} \quad [4.3]$$

By analogy, the Hamiltonian for an NMR active nuclear spin (with a magnetic moment) interacting with the magnetic field of an NMR spectrometer is:

$$\hat{H} = -\hat{\boldsymbol{\mu}} \cdot \mathbf{B} = -\hat{\mu}_z B_z \quad [4.4]$$

since the spectrometer magnetic field is defined as lying along the z-direction of the laboratory reference frame (33-36). From this point onward, the circumflex "^" accent may be dropped for operators, except where the fact that an object is an operator is meant to be emphasized.

4.3.1 A real NMR sample

A real NMR sample contains many spins. One can solve for any macroscopically observable quantity, A, with a corresponding quantum mechanical operator, $\hat{A}$, in the following manner:

$$A = \sum_a w_a \langle \psi_a | \hat{A} | \psi_a \rangle \quad [4.5]$$

where w_a is defined as the population of spins in the quantum mechanical state defined by the $|\psi_a\rangle$ wavefunction and the sum extends over all spins, a, of the NMR sample. It is convenient to insert an identity matrix using the completeness relation, $\mathbb{I} = \sum_b |b\rangle\langle b|$ (the eigenfunctions $|b\rangle$ form an orthonormal eigenbasis):

$$A = \sum_a \sum_b w_a \langle \psi_a | \hat{A} | b \rangle \langle b | \psi_a \rangle \quad [4.6]$$

Rearranging this equation gives:

$$A = \sum_a \sum_b w_a \langle b | \psi_a \rangle \langle \psi_a | \hat{A} | b \rangle \quad [4.7]$$

The density matrix, ρ, is defined as $\rho \equiv \sum_a p_a |\psi_a\rangle\langle\psi_a|$ (where p_a is the probability that a nuclear spin is described by the wavefunction $|\psi_a\rangle$), and multiplied by N, the number of spins in the sample:

$$N\rho = N \sum_a p_a |\psi_a\rangle \langle\psi_a| = \sum_a w_a |\psi_a\rangle\langle\psi_a| \quad [4.9]$$

Substituting equation [4.9] back into equation [4.7], it is found that:

$$A = N \sum_b \langle b | \rho \hat{A} | b \rangle = N \, \mathrm{Tr}\{\rho \hat{A}\} \quad [4.10]$$

according to the definition of trace (the trace of a matrix P, or "Tr{P}," is the sum of its diagonal elements). Analogous to the manner in which a wavefunction describes the state of a single NMR spin, a density matrix describes the macroscopic state of an ensemble of NMR spins. In the spectrometer's magnetic field, the density matrix at equilibrium ($\rho_{eq.}$) is given by:

$$\rho_{eq.}=\sum_{m_z}\frac{\exp\left[\left(-\frac{1}{2}\gamma\hbar m_z B_z/k_B T\right)\right]}{Z}\left|\psi_{m_z}\right\rangle\left\langle\psi_{m_z}\right| = A_1\mathbb{I} + A_2 I_z \qquad [4.11]$$

where A_1 and A_2 are scalar coefficients, Z is the partition function, k_B is the Boltzmann constant and T is the temperature. In principle, all the properties of the NMR sample are reproduced if the sample is considered to have a density matrix of $\rho=I_z$ at equilibrium and so it is assumed that $\rho=I_z$ at equilibrium. These angular momentum operators are often used as a simplified representation of the state of an NMR sample at any given moment in time. The use of a linear combination of base operators to represent the density matrix is called the product operator formalism (37). Graphical representations which describe angular momentum operator terms in the density matrix are given in Figure 4.1 (33-36).

4.3.2 The Liouville-von Neumann equation governs the evolution of the density matrix

A differential equation describing the time evolution of the density matrix can easily be derived from the time dependent Schrödinger equation. First, the partial derivative of the density matrix, defined as $\rho\equiv\sum_a p_a \left|\psi_a\right\rangle\left\langle\psi_a\right|$, is taken with respect to time:

$$\frac{\partial \rho}{\partial t} = \frac{\partial}{\partial t}\left(\sum_a p_a \left|\psi_a\right\rangle\left\langle\psi_a\right|\right) \quad [4.12]$$

According to the product rule:

$$\frac{\partial \rho}{\partial t} = \sum_a p_a \left(\frac{\partial}{\partial t}\left|\psi_a\right\rangle\right)\left\langle\psi_a\right| + p_a\left|\psi_a\right\rangle\left(\frac{\partial}{\partial t}\left\langle\psi_a\right|\right) \quad [4.13]$$

The time-dependent Schrödinger equation may be written:

$$\frac{\partial\left|\psi\right\rangle}{\partial t} = -\frac{i}{\hbar}\hat{H}\left|\psi\right\rangle \quad [4.14]$$

Or, rearranging:

$$\frac{\partial\left\langle\psi\right|}{\partial t} = \frac{i}{\hbar}\left\langle\psi\right|\hat{H} \quad [4.15]$$

Using both [4.13] and [4.14] to substitute into [4.12], the following expression is derived:

$$\frac{\partial \rho}{\partial t} = -\frac{i}{\hbar}\sum_a p_a\left(\hat{H}\left|\psi_a\right\rangle\left\langle\psi_a\right| - \left|\psi_a\right\rangle\left\langle\psi_a\right|\hat{H}\right) = -\frac{i}{\hbar}\left(\hat{H}\rho - \rho\hat{H}\right) = \frac{i}{\hbar}[\rho,\hat{H}] \quad [4.16]$$

This is the famous Louiville-von Neumann equation. Its general solution is given as:

$$\rho(t) = e^{-i\hat{H}t}\rho(0)\, e^{i\hat{H}t} \quad [4.17]$$

Recall the Hamiltonian for an NMR active nuclear spin (with a magnetic moment) interacting with the magnetic field of an NMR spectrometer. It is possible to solve for the evolution of the density matrix under the influence of the spectrometer's magnetic field as follows:

$$\rho(t) = e^{-i\hat{H}t}\rho(0)\, e^{i\hat{H}t} = e^{-\gamma\hbar B_z I_z t} I_z e^{\gamma\hbar B_z I_z t} \quad [4.18]$$

Expanding $e^{-\gamma\hbar B_z I_z}$ into a power series in I_z and solving the right side of the equation, we find that $\rho(t)= I_z$. In other words, because $\left[\rho,\widehat{H}\right] = 0$, $\frac{\partial\rho}{\partial t}=0$ (33-36).

4.3.3 The rotating frame and toggling (interaction) frames

Consider an NMR sample magnetized along the x-axis of the laboratory frame. Its time evolution will be:

$$\rho(t) = e^{-\gamma\hbar B_z I_z t} I_x e^{\gamma\hbar B_z I_z t} = I_x \cos\gamma\hbar B_z\, t - I_y \sin\gamma\hbar B_z t \qquad [4.19]$$

This result might be obtained by expanding $e^{-\gamma\hbar B_z I_z}$ into an infinite product series and multiplying it by I_x on the right hand side. Then, after multiplying by $e^{\gamma\hbar B_z I_z}$ on the left hand side and rearranging, one will find the power series expansion of $\sin\gamma\hbar B_z t$ multiplied by nested commutators that all equal $-I_y$ and the power series expansion of $\cos\gamma\hbar B_z\, t$ multiplied by expressions equaling I_x. The evolution of these operator terms of the density matrix has been described in detail by Sørenson et al. (37). The spins are said to precess about the magnetic field at their Larmor frequency.

Linearly oscillating RF magnetic fields are applied to NMR samples to perturb the sample. These linearly RF fields may be decomposed into two counter-rotating RF fields. In the rotating frame, an on resonance pulse applied along the x-axis remains along the x-axis. Just as was the case with Zeeman precession (as shown above) occuring about the static spectrometer field, magnetization vectors will precess about the magnetic field in the rotating frame, which is called nutation (see Figure 4.2). Before the oscillating magnetization is recorded by the spectrometer, it is mixed with a reference signal and ultimately a low frequency signal that corresponds to nuclear spin evolution in the

rotating reference frame is recorded. Unless otherwise noted, the rotating reference frame will automatically be assumed from now on.

In general, the magnetization of the sample is observed in a reference frame that rotates at a frequency of $\gamma\hbar B_z$ along with the x-magnetization of the sample. In this reference frame, I_x remains I_x unless the chemical environment of the spin (or some other NMR interaction) changes its precession frequency. The rotating frame is an example of an "interaction reference frame" that accounts for the Zeeman precession of NMR spins about the large, static magnetic field of an NMR spectrometer. In general, reference frames may be adopted where the applied radiofrequency (RF) pulses have no effect on the density matrix. In these reference frames, however, new time dependencies are introduced into the NMR interactions, such as dipolar coupling, as a result of mathematically neutralizing the effect of RF pulses. If several RF pulses are applied, it is possible, given that certain conditions are met, to "toggle" between references frames and the reference frame assumed is called a toggling reference frame (38-40).

4.3.4 Average Hamiltonian theory

Just like reorientation can average the time evolution of nuclear spins, it is possible to perturb a spin system with varying RF pulses. If the perturbation is periodic and cyclic, the spins will evolve as if under the influence of an average Hamiltonian ($\bar{H}$). This average Hamiltonian may be used to describe the spin evolution under COMPOZER-CP of coupled I and S spins. The use of this theory will be demonstrated in the treatment of coupled I and S nuclear spins under COMPOZER-CP irradiation (41).

4.3.5 Regular cross polarization

In regular cross-polarization (Figure 4.3), a 90° y-phase phase pulse is applied to the proton channel, which creates I_x magnetization of the proton spins. Then continuous x phase RF irradiation is applied. In the rotating frame, the I_x magnetization only feels the magnetic field of the radiofrequency irradiation, which is along the x direction in the rotating frame. Therefore, the proton magnetization remains along the x-axis of the rotating reference frame. This is called a spin-lock. Meanwhile, RF radiation of the same strength is applied to the S-channel, which means that, in the rotating frame S spins feel the same effect from the RF irradiation from the S channel as I spins feel the effect of RF irradiation from the I channel (the corresponding nutation frequencies are the same, see Figure 4.2).

An interaction reference frame is assumed where the effects of I spin and S spin irradiation are zero (called the double-rotating reference frame (43)). In this reference frame, assuming both RF fields are applied exactly at resonance with the I and S spins, during the spin lock on the I channel and irradiation on the S channel, the interaction frame Hamiltonian can be described as:

$$\widehat{H} \propto I_z S_z + I_y S_y \qquad [4.20]$$

This Hamiltonian leads to time-oscillatory coherence transfer when only one I and S spin are connected. However, when a bath of I spins (usually protons) is present, a smoother build-up of magnetization is achieved as magnetization from the I spins equilibrates with the S spin (see Figure 4.4 for a comparison of these two cases) (42).

4.3.6 Composite zero degree cross polarization (COMPOZER-CP)

COMPOZER-CP consists of a series of 360° pulses applied simultaneously on both the I and the S channels. Consider 360° pulses applied simultaneously along the x-axes on both the I and S channels. The interaction frame Hamiltonian (that accounts for the interaction between the I and S spins and the RF fields) is given as (44):

$$\hat{\mathrm{H}}_{\mathrm{d}}(t) = \mathrm{d}\left[\mathrm{I_z}\cos(\omega_{1I}t) + \mathrm{I_y}\cos(\omega_{1I}t)\right]\left[\mathrm{S_z}\cos(\omega_{1S}t) + \mathrm{S_y}\cos(\omega_{1S}t)\right] \qquad [4.21]$$

where ω_{1I} and ω_{1S} represent the strengths of the RF fields applied. The time evolution of a spin system subject to this Hamiltonian is complicated by the Hamiltonian's time-dependence. The average Hamiltonian theory states that the time evolution of the spin system

$$\hat{\mathrm{U}}_{\mathrm{d}}(t)\rho(0)\hat{\mathrm{U}}_{\mathrm{d}}^{-1}(t) \qquad [4.22]$$

where $\hat{\mathrm{U}}_{\mathrm{d}}(t) = \exp\left[-\mathrm{i}\hat{\mathrm{H}}_{\mathrm{d}}(t)t\right]$ can be approximated, when the RF irradiation applied and the Hamiltonians governing spin evolution are periodic and cyclic, using an average, time-independent Hamiltonian (41)

$$\hat{\mathrm{U}}_{\mathrm{d}}(t)\rho(0)\hat{\mathrm{U}}_{\mathrm{d}}^{-1}(t) \approx \bar{\mathrm{U}}_{\mathrm{d}}\,\rho(0)\bar{\mathrm{U}}_{\mathrm{d}}^{-1} \qquad [4.23]$$

where $\bar{\mathrm{U}}_{\mathrm{d}} = \exp(-\mathrm{i}\bar{\mathrm{H}}_{\mathrm{d}}t)$, and the evolution arising the RF fields applied are cyclic over a cycle τ (meaning $\bar{\mathrm{U}}_{\mathrm{RF}} = \exp(-\mathrm{i}\bar{\mathrm{H}}_{\mathrm{RF}}\tau) = \mathbb{I}$, where $\mathbb{I}$ is the identity matrix).

$$\bar{\mathrm{H}}_{\mathrm{d}} = \frac{1}{\tau}\int_0^{\tau} dt\hat{\mathrm{H}}_{\mathrm{d}}(t) \qquad [4.24]$$

$\bar{\mathrm{U}}_{\mathrm{d}}$ is the zeroth order approximation of the time evolution of the spin system (higher orders of approximation may be used to obtain a more accurate impression of the nuclear

spins' evolution). Substituting for $\hat{H}_d(t)$ using equation [4.21] and integrating from zero to $t = 2\pi/\omega_{1I} = 2\pi/\omega_{1S}$ (a 360° x-phase pulse is applied), it is found that

$$\bar{H}_d = \frac{d}{2}(I_zS_z+I_yS_y) \quad [4.25]$$

These calculations may be repeated for y-phase pulses (instead of an x-phase pulses), giving an overall zeroth order average Hamiltonian of

$$\bar{H}_d = \frac{d}{2}(2I_zS_z+I_xS_x+I_yS_y) \quad [4.26]$$

Because this Hamiltonian contains a $I_xS_x+I_yS_y$ term, it affects magnetization transfer from the I spins to the S spins along the z axis. Composite pulses, where the phase of the RF irradiation is switched by 180°, are used in COMPOZER-CP to minimize the effect of RF pulse miscalibration. Although this transfer of magnetization along the z-axis has the practical advantage that magnetization transfer along the z-axis can be maintained for a much longer (due to differences in the relaxation along the spectrometer static field, T_1, and the spin-lock field $T_{1\rho}$), for COMPOZER-CP's applications to PELF, the fact that homonuclear dipolar coupling between I spins (which connects the I spin to its I spin bath as shown in Figure 4.3), given by $\hat{H}_D = D(3I_{1z}I_{2z} - \mathbf{I_1}\cdot\mathbf{I_2})$, is scaled down by half is a particularly useful feature of COMPOZER-CP. Compared to the regular CP sequence, less coupling to the I spin bath is observed for the COMPOZER-CP sequence, as shown in Figure 4.5. However, as may be noted from equation [4.26] (the dipolar coefficient *d* is scaled by half and the Hamiltonian contains I_zS_z terms that do not contribute to magnetization transfer), magnetization transfer occurs more slowly when the COMPOZER-CP sequence is used. This homonuclear decoupling property of COMPOZER-CP led to the development of PELF-COMPOZER (44).

4.3.7 Using COMPOZER-CP or WIM for magnetization transfer instead of regular CP vastly improves spectral resolution

A typical PELF radio frequency (RF) pulse sequence is given in Figure 4.5. In the PELF sequence, the transverse magnetizations of protons evolve under heteronuclear dipolar coupling (with an evolution frequency Ω_{IS}) during the incrementable t_1 period, while chemical shifts of protons and ^{1}H-^{1}H homonuclear dipolar couplings are suppressed. This "labels" the protons with their heteronuclear dipolar coupling to the rare nucleus (often ^{13}C or ^{15}N) (31, 45-46). After the t_1 period, the transverse ^{1}H magnetization is transferred to the rare nucleus (referred to as X, often either ^{13}C or ^{15}N) for detection as shown in Figure 4.5. Since there is no homonuclear dipolar coupling between rare X nuclei and each ^{1}H spin is coupled to a single X nuclear spin, for every resolvable X resonance, either a single doublet corresponding to a single ^{1}H-X dipolar coupling or a simple superposition of doublets corresponding to different sets of ^{1}H-X pairs is observed in the indirect frequency dimension of a 2D PELF spectrum. The elegant PELF technique thereby avoids the complicated multiplet-type spectral pattern typically observed in the indirect dimension of other SLF sequences where X spin transverse magnetizations are allowed to evolve under the dipolar couplings to many ^{1}H nuclei (32, 47). In other words, after dipolar coupling between a rare X nucleus and the ^{1}H nuclei has evolved for a period of t_1, the relevant term of the density operator contributing to the detected signal is given as

$$\sum_j I^j_{x/y} \cos \Omega_{IS} \qquad [4.26]$$

Magnetization transfer in a PELF pulse sequence can be accomplished by any of the following means, depending on sample conditions and the spin system dynamics: a standard cross-polarization (CP) scheme, a CP scheme based on the Lee-Goldburg

homonuclear dipolar decoupling, WIM (Windowless Isotropic Mixing), COMPOZER-CP, or INEPT (Insensitive Nuclei Enhanced by Polarization Transfer)/RINEPT (Refocused Insensitive Nuclei Enhanced by Polarization Transfer). The resolution and sensitivity of a 2D PELF spectrum critically depends on the details of the pulse sequence used to transfer the ^{1}H transverse magnetization (32, 47). For example, a short transfer time is required to suppress ^{1}H spin diffusion, which manifests as a broad zero-frequency peak in the indirect dipolar coupling frequency dimension that severely obscures the spectrum (because a certain amount of magnetization gets transferred to the rare nucleus regardless of how dipolar coupling evolves on the protons, a baseline shift manifests in the indirect dimension which manifests as a zero frequency artifact in the final spectrum) (32). Furthermore, for most solid-state systems the rapid rotating-frame relaxation ($T_{1\rho}$) of protons, which causes the amount of spin-locked magnetization to decay, could hamper the efficiency of magnetization transfer, particularly in the standard CP sequence where the transverse magnetization is transferred from protons to less-sensitive nuclei like ^{13}C or ^{15}N. Since for most systems the proton T_1 (spin lattice relaxation time, a time relating the rate at which magnetization exponentially grows along the z-axis) is much longer than $T_{1\rho}$, it is advantageous to use a magnetization transfer scheme whereby the transfer of magnetization occurs along the z-axis. Currently, two schemes, WIM and COMPOZER-CP, can render such a magnetization transfer while providing homonuclear decoupling to dampen the ^{1}H-^{1}H spin diffusion process (44, 47). It may be noted that the homonuclear decoupling of WIM sequence is more effective than that of the COMPOZER-CP. Therefore, in this study, the performances of these two schemes (COMPOZER-CP and WIM) in PELF sequences are compared with that of the standard

CP. The other two magnetization transfer sequences, namely Lee-Goldburg-CP and INEPT, are excluded from this study. Lee-Goldburg-CP is highly sensitive to the offset from the nuclei's Larmor frequency (it requires that the irradiation applied be offset from the nuclear Larmor frequency) and may not be appropriate as a general magnetization transfer protocol (47). Furthermore, magnetization transfer by INEPT sequences only occurs in highly mobile samples and is therefore limited in their applicability to only the mobile regions of membrane proteins (23).

4.3.8 Resonance assignments in solid-state NMR using the PELF-MIX sequence

These insights require detailed information at the atomistic level in which only a high-resolution technique, such as NMR spectroscopy or X-ray crystallography, can provide. In particular, solid-state NMR (SS-NMR) spectroscopy has become a powerful technique used to elucidate molecular structures and dynamics for non-crystalline samples. The generation of correlations between proton resonances of a PELF spectrum may be accomplished by inserting a mixing period before the transfer of magnetization, as shown in Figure 4.6. The process of proton spin diffusion, if controlled, may be used to generate correlations between spatially proximate protons without obscuring 2D NMR spectra. The use of COMPOZER-CP or WIM minimizes the obscuring effect of spin diffusion during the magnetization transfer step. Reinstituting proton spin diffusion in a controlled manner allows the correlation between protons to be established, while the obscuring properties of spin diffusion remain negligible. By using deuterated samples, the obscuring effects of proton spin diffusion may be further minimized and the correlations between the protons of interest will be magnified.

This technique is established via computer simulations and has been demonstrated experimentally on a MBBA (n-4'-MethoxyBenzylidene-n-ButylAnilin) liquid crystal sample. The goal is to establish the feasibility of this approach and its applicability in membrane protein studies.

4.4 Experimental methods

Numerical simulations were performed using the program SPINEVOLUTION (48). The simulated spectra and CP buildup curve were plotted using *SigmaPlot 9.0*. The details of the simulation are described in the results section below. All numerical simulations were performed on a 2.0 GHz Intel Quad Core HP desktop running Window Vista.

4.5 Results of the numerical investigations of PELF

The influence of magnetization transfer schemes on the resolution and sensitivity of a 2D PELF spectrum, specifically in the heteronuclear dipolar coupling dimension, is investigated through numerical simulations on a hypothetical spin system defined in Figure 4.7 using the SPINEVOLUTION software (48). In this spin system, an NH group is weakly coupled to an neighboring proton such that it demonstrates the case of a biomolecules embedded in the membranes and/or to reflect motionally averaged N-H dipolar couplings as found in relatively mobile regions of a protein. N-H dipolar coupling slices taken from the indirect dimension of the simulated SLF spectrum are shown in Figure 4.8. As illustrated by our numerical simulations (Figures 4.8 and 4.9), not only the choice of the magnetization transfer scheme but also the duration of the magnetization transfer significantly influence the resolution of a PELF spectrum. With a transfer contact

time of approximately 250 μs, all of the magnetization transfer schemes give identical dipolar doublets corresponding to the large dipolar coupling (D_1). As the transfer time is increased, significant differences between the spectra are observed, which is a direct consequence of the differences among the magnetization transfer schemes employed (see Figure 4.9). Figure 4.9 shows that the intensity of the strong dipolar coupling (the outer doublet in Figure 4.8) oscillates strongly as a function of magnetization transfer time when WIM or regular CP was used as a magnetization transfer sequence. The WIM sequence offers the highest homonuclear decoupling and therefore allows for the detection and isolation of the weak dipolar coupling D_2 in the presence of the strong coupling D_1, which could be suppressed by the choice of an appropriate magnetization transfer time. On the other hand, as the strength of the homonuclear decoupling decreases, the spectral resolution deteriorates because of the obscuring effect of spin diffusion. Spin diffusion manifests as a zero frequency artifact in the indirect dimension (see Figures 4.8E and 4.8F). As a result, an intense central peak at the zero frequency is observed, obstructing the measurements of weak dipolar couplings. Also, for a long contact time, D_1 is more effectively suppressed when COMPOZER-CP or WIM magnetization transfer schemes are used, which is a consequence of the spin diffusion facilitated by the proton bath. Therefore, the use of these magnetization transfer schemes allow for broader optimal contact time conditions.

The use of the PELF method to extract dynamical and structural information from cytochrome b_5 (Cytb5), a membrane-anchored protein, is demonstrated in Figure 4.10. Cytochrome b_5 consists of a transmembrane domain near the C-terminal, a water-soluble heme-containing domain, and a linker region that connects these two domains. Functional

studies have shown that the length of the linker region is crucial for cytochrome b_5 to interact with and donate an electron to activate cytochrome P450 (49). In the present study, a mutant of cytochrome b_5 (mutant-Cytb5), which lacks 8 residues in its linker region, is used to demonstrate the efficiency of the PELF sequence. A previous solid-state NMR study revealed the various domains of this protein display motions occurring on a wide range of timescales (23). Since the mutant protein used in this study lacks 8 residues in the linker region, the motion of the soluble domain should be significantly reduced such that small, yet measurable, dipolar couplings can be observed. Therefore, it is an ideal system to firmly establish and demonstrate the effectiveness of using the PELF sequence to study the structure and dynamics of membrane proteins in magnetically-aligned bicelles. See appendix C for sample preparation details and for a detailed description of how the spectra shown in Figure 4.10 were acquired.

Numerical simulations on a 4-spin system (shown in 4.11E) were performed to study how correlations amongst neighbouring spins are generated via proton spin diffusion. In this case, the spin diffusion process takes place between the protons in the absence of a proton bath, which allows for the sequential assignment resonances in an SLF spectrum. This is analogous to a PELF-MIX experiment performed in a deuterated background. Because the spin-diffusion process and the magnetization transfer processes occur independently, the quality and quantity of spin-diffusion can be manipulated, which enables the acquisition of high quality spectra and proton-proton correlations. Due to the large homonuclear dipolar couplings between protons, only a short mixing time period (t_{mix}) is required to generate a complete correlation mapping compared to the recently proposed proton driven ^{15}N-^{15}N-correlation technique (50). The use of PELF-

MIX to obtain ^{1}H-^{1}H correlations for MBBA (n-4'-MethoxyBenzylidene-n-ButylAnilin) liquid crystal sample is demonstrated in Figure 4.12. See appendix C for sample preparation details and for a detailed description of how the spectra shown in Figure 4.12 were acquired.

4.6 Discussion of the numerical investigations of PELF

In summary, from these numerical simulations, we may conclude the following: 1) significant resolution is gained by using a magnetization transfer scheme that suppresses ^{1}H-^{1}H interactions, 2) the main contributors to the central peak observed in the 2D PELF spectrum using the COMPOZER-CP and the regular CP originate from the proton spin diffusion process, 3) weak ^{1}H-^{1}H dipolar coupling ensures that the amount of ^{1}H magnetization transferred to an X nucleus builds up steadily, which enables a broad range of transfer times to be used, and 4) proton spin-diffusion can be incorporated back into the PELF sequence to generate ^{1}H-^{1}H correlations, which are important for resonance assignment in the solid state. When a ^{1}H-^{1}H dipolar coupling is completely eliminated, magnetization is transferred back and forth between insensitive X nuclei and sensitive ^{1}H nuclei, and therefore the transfer time has to be carefully calibrated. This makes PELF-COMPOZER the most generally suitable technique for measuring weak X-^{1}H dipolar couplings (X may be ^{13}C or ^{15}N). In order to acquire a highly resolved SLF spectrum of an aligned membrane protein using the 2D PELF pulse sequence, one must use a magnetization transfer scheme that suppresses ^{1}H-^{1}H dipolar coupling interactions while using the shortest contact time that permits the observation of the desired range of dipolar coupling frequencies. However, PELF-WIM affords more control over the spin-

diffusion process and therefore is most often the better choice for resonance assignment in the solid state.

Notably, the resolution afforded using the PELF techniques described here can be extended to other spin systems, particularly the methyl groups. Recently, ^{13}C labeled methyl groups have been demonstrated to be an exquisite NMR probe for investigating dynamics, structure and biological functions of large protein complexes and the fact that Val, Ile, Leu, Ala, Met and Thr, constitute 30 - 45% of all the amino acids in membrane proteins, the methyl group is becoming an important molecular probe for interrogating membrane protein structures and dynamics (51-53). However, the use of methyl ^{13}C-^{1}H dipolar couplings in SLF studies of membrane proteins remains a challenge due to the lack of dispersion in the methyl ^{13}C chemical shifts as well as the complicated multiplet lineshape in the indirect dimension due to the use of SLF sequences such as PISEMA, HIMSELF and SAMMY (51, 53). Therefore, the PELF methods implemented in the current studies can be used to simplify the complicated line shape in the indirect dimension, allowing for the accurate measurement of methyl's ^{13}C-^{1}H dipolar couplings. The methyl ^{13}C-^{1}H dipolar couplings can provide dynamical information on a variety of biological systems. For example, the association of two different helices of a membrane protein often restricts the methyl group rotation at the binding interface, resulting in an increase in the magnitude of methyl's ^{13}C-^{1}H dipolar couplings. Therefore, through measuring the changes in the ^{13}C-^{1}H dipolar couplings, both the binding interface between two helices and the strength of their interactions at each methyl site can be deduced by comparing the order parameters of methyl groups as long as their resonances are resolvable. Furthermore, methyl ^{13}C-^{1}H dipolar couplings can provide structural

constraints regarding the helical tilt similar to the recently proposed GALA (Geometric Analysis of Labeled Alanines) method that exploits the deuterium quadrupolar coupling of a CD_3 system (54-55). While the GALA method is successful in providing the tilt angle of a helix in both oriented and unoriented samples, it requires numerous selectively deuterated methyl samples for different Ala residues, which is not practical (55). The advantage of using the CH_3 group is that multiple Ala methyl sites can be ^{13}C labeled and their ^{13}C-^{1}H dipolar couplings can be simultaneously measured using the PELF protocols provided their resonances are resolvable. Therefore, the PELF sequence can be extended to CH_3 spin systems, providing both side chain dynamics and structural constraints for refining protein secondary structures (51).

The ability to measure a broad range of dipolar couplings allows for not only the determination of structures, but also the understanding of protein dynamics at various time scales as illustrated in our studies. Dipolar couplings can provide information on both the orientation of bond vectors and the amplitude of motions up to the millisecond time scale (56-58). Under the commonly used rotating-frame SLF pulse sequences, only motions in the range of $10^{-4} – 10^{-5}$ s are observed, which reflects the rotational diffusion of a transmembrane α-helix (59). However, under the PELF approach, motions up to 10^{-3} s are revealed; thus, opening up a new avenue for probing protein dynamics via solid-state NMR experiments on aligned samples. In fact, a complete mapping of protein dynamics is now possible, using a combination of relaxation and dipolar coupling measurements (58). Currently, applications of SLF spectroscopy mainly focus on the determination of the transmembrane domain structures of membrane proteins. Yet, in many cases, particularly for the case of membrane-associated receptors, a significant

portion of the protein is in the cytoplasmic domain and conformational changes in one region of a protein can be propagated to another region through changes in protein motions such as those observed in dynamically driven allosteric interactions (60). Despite many advances in solid-state NMR methodology, the synergy of these conformational changes has so far not been well characterized. Thus, the ability to produce a complete mapping of protein dynamics and their correlation with each other will allow for a better understanding of the intricate and enigmatic relationships between the structure of a protein and its biological functions.

4.7 Acknowledgements

This work was supported by the National Institutes of Health (GM084018 and RR023597 to A.R.) and CRIF-NSF funding for the NMR spectrometer.

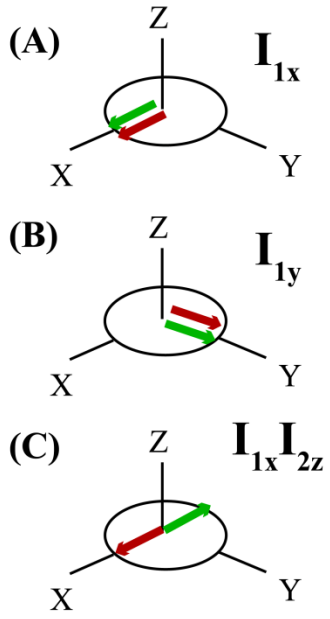

Figure 4.1 Diagrams of product operators. Adapted from (37), figure 1. The product operators shown here represent x, y, and z macroscopic magnetization in the rotating reference frame for a system of two coupled I = l/2 nuclei. Each arrow represents roughly half of the magnetization associated with the spin indexed as one. (A) Magnetization along the x-axis of the rotating frame (for spin one). (B) Magnetization along the y-axis. (C) Antiphase x magnetization of spin one (the x-magnetization of spin one is correlated to the z-magnetization of spin two). Single quantum coherences are states of the density matrix, such as I_x (A) and I_y (B) above, that connect two energy levels with $\Delta m=\pm 1$; they are a coherent superpositions of the $|\boldsymbol{\alpha}\rangle$ and $|\boldsymbol{\beta}\rangle$ states which have a difference in the m secondary spin quantum number of ±1. For example, if one takes the outer product of the I_x operator eigenket in the I_z eigenbasis, i.e. $\frac{\mathbf{1}}{\mathbf{2}}(|\boldsymbol{\alpha}\rangle + |\boldsymbol{\beta}\rangle)(\langle\boldsymbol{\alpha}| + \langle\boldsymbol{\beta}|)$, one will see off-diagonal elements arise in the corresponding matrix that are often referred to as a single-quantum coherences (this also works for the I_y operator eigenket). This matrix represents the density matrix of a pure ensemble where every spin has a wavefunction of $|\boldsymbol{\psi}\rangle = \frac{\mathbf{1}}{\sqrt{\mathbf{2}}}(|\boldsymbol{\alpha}\rangle + |\boldsymbol{\beta}\rangle)$. In practice, the spins in a real NMR experiment almost never all have the same wavefunction (the eigenket of I_x, in this case) and a measure of the disorder in the wavefunctions of the spins is known as the von Neumann entropy. A term of I_x means that $\langle I_x\rangle$ tends to be greater than zero for most spins in the NMR sample.

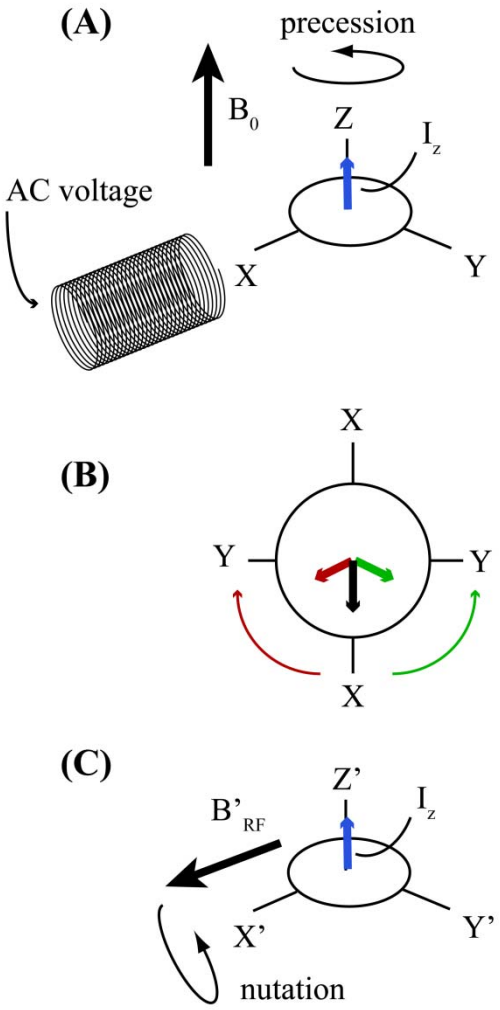

Figure 4.2 Spin evolution in various reference frames. (A) In the laboratory frame, magnetization precesses about the Z axis. The nuclear spins reach an equilibrium magnetized state and a magnetization proportional to I_z results. An AC voltage applied through a solenoid coil will result in a linearly oscillating magnetic field being applied along the X axis of the laboratory frame (in modern spectrometers, other coil geometries might be used). As shown in (B), this linearly oscillating magnetic field (black) might be decomposed into two counter-rotating, circularly polarized, oscillating magnetic fields (green and red) of which only one, on resonance, component will influence the evolution of nuclear spins. (C) In the rotating frame, the interaction that the nuclear spins have with the static magnetic field of the spectrometer is accounted for and does not influence spin dynamics (the frame rotates along with the nuclear spins as they precess). Therefore, the nuclear spins only see the component of RF field applied at resonance along the X' axis of the rotating frame and nutate about this axis. The nutation frequency may be used as a measure of the applied RF field strength.

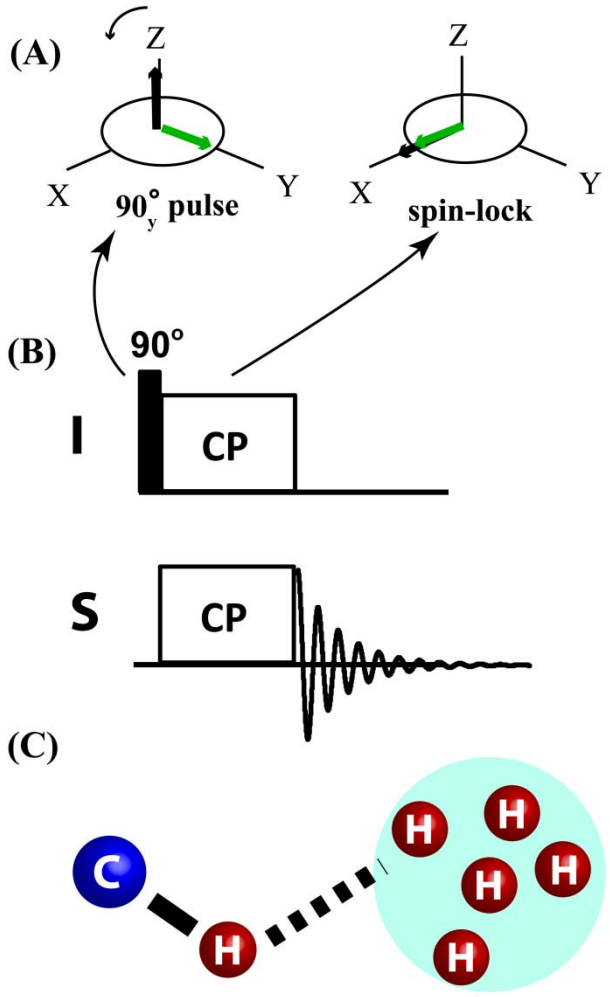

Figure 4.3 The regular cross polarization (CP) pulse sequence. (A) On the I channel, a 90° y-phase pulse (written as $90°_y$) is applied, as shown by the green arrow. The black magnetization vector is then tilted into the xy-plane, and ends oriented along the x-axis. As soon as the magnetization reaches the x-axis of the rotating frame, RF radiation with x phase is applied, resulting in the magnetization being "locked" along the x axis of the rotating reference frame. (B) The CP pulse sequence. The blocks represent periods where AC current is applied through the circuit. The S channel RF irradiation is usually along the x-axis of the rotating frame. (C) A diagram illustrating that the oscillatory properties of magnetization transfer between carbon and proton spins is smoothed out by the proton's coupling to a proton bath (the term is used in analogy to its use in thermodynamics).

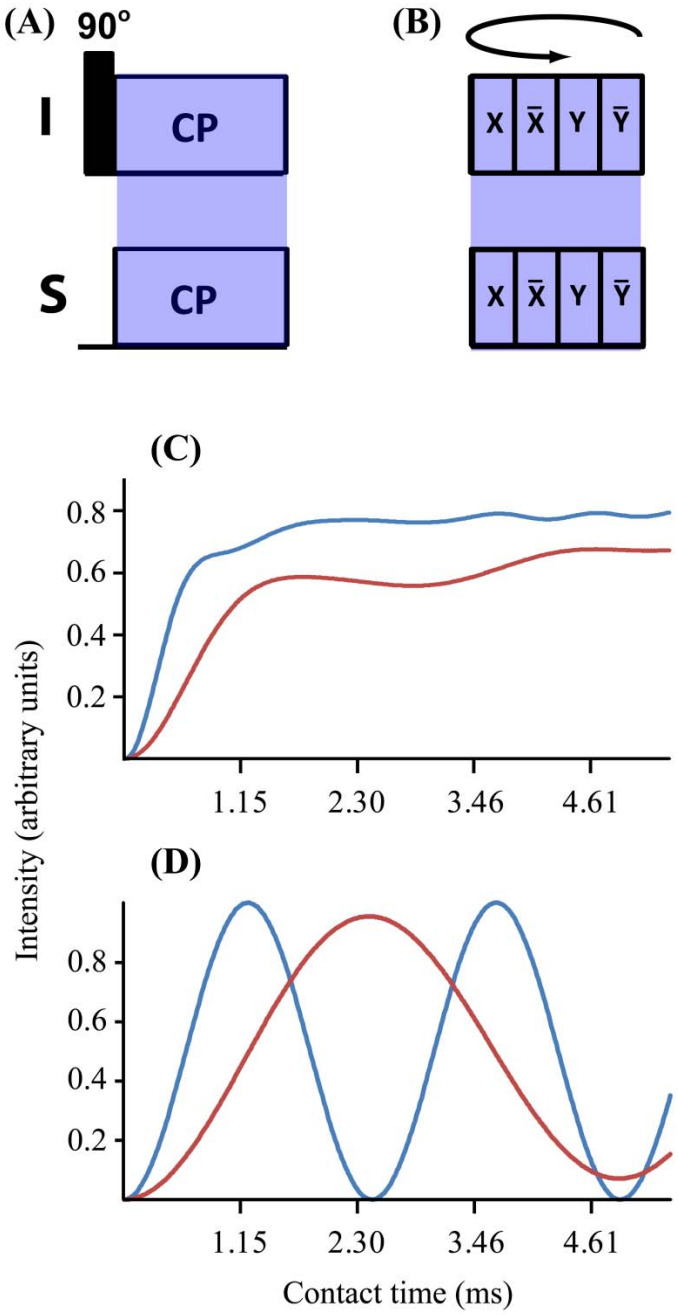

Figure 4.4 Magnetization build-up along the x-axis (for regular CP) or the z-axis (for COMPOZER-CP) for the S nucleus. During the contact time highlighted in blue for (A) regular CP and (B) COMPOZER-CP (note that the block of 4 pulses is repeated for COMPOZER-CP), S spin magnetization build-up along the x-axis of the rotating reference frome is monitored for regular CP and along the z-axis for COMPOZER-CP. In (C), the build-up of magnetization for COMPOZER-CP (red) and regular CP (blue) is given for a ^{15}N-^{1}H-^{1}H spin system connected to a bath of seven protons and, in (D), the build-up is given in the absence of a proton bath. (C) and (D) were simulated using the SPINEVOLUTION software (48).

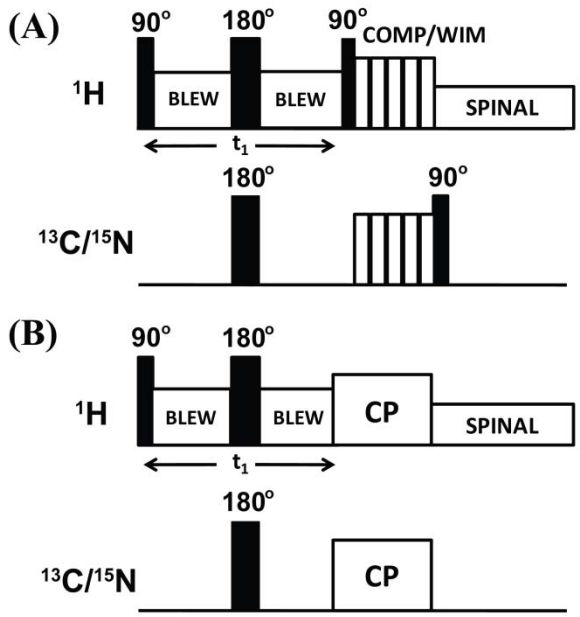

Figure 4.5 Radio frequency PELF pulse sequences for 2D SLF spectroscopy of solids. In these pulse sequences, proton homonuclear decoupling in the t_1 period is achieved using the BLEW-12 sequence and SPINAL-64 is used to decouple protons during acquisition. Proton transverse magnetization after the t_1 period is transferred to X nuclei using the COMPOZER-CP or WIM pulse sequence. (A) or by the standard cross-polarization sequence (B). A supercycled COMPOZER sequence consists of a series of 360° pulses with phases x, -x, y, -y, -y, y, -x, x. The WIM sequence consists of a series of 90° pulses of phases -x, y, -x, -x, y, -x, x, y, x, x, y, x. Since the z-component of proton magnetization is transferred as the z-component of ^{15}N or ^{13}C spin magnetization under both WIM and COMPOZER-CP sequences, a 90° read pulse on the ^{15}N or ^{13}C channel is used for detection.

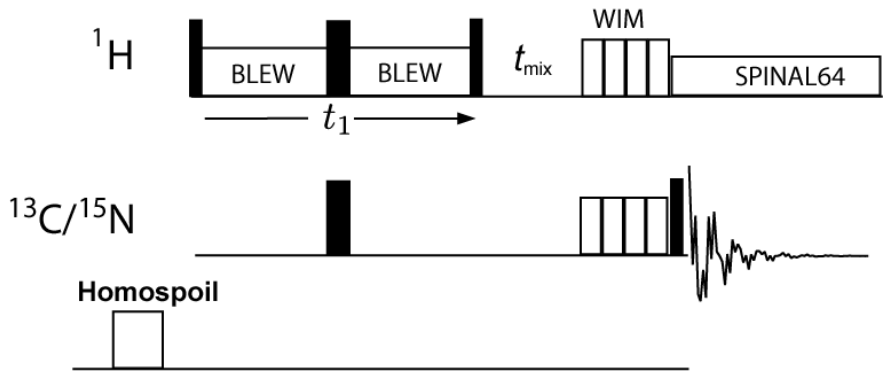

Figure 4.6 Pulse sequence used for high resolution PELF-MIX experiments. All narrow solid squares represent 90-degree pulses, while the wide solid squares are 180-degree pulses. A homo-spoil pulse is applied before any pulses which destroys any magnetization in the transverse (xy) plane.

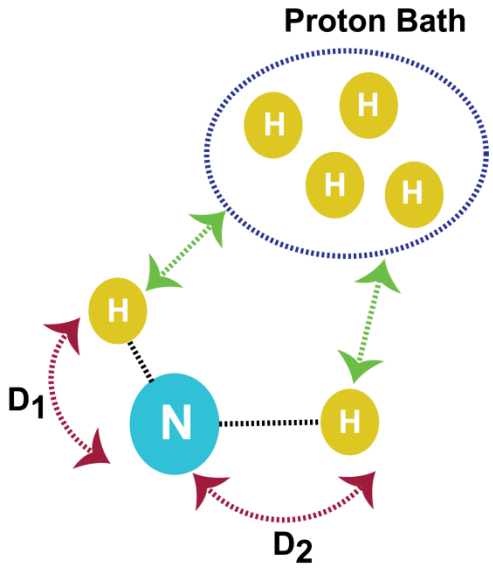

Figure 4.7 A schematic of a hypothetical spin system to evaluate the PELF pulse sequence. In this system, a ^{15}N nucleus is strongly dipolar coupled to two nearby protons. The dipolar coupling values used in the simulations are $D_1 = 1750$ Hz and $D_2 = 500$ Hz. The ^{15}N-^{1}H dipolar couplings are arranged such that $D_1 > D_2$ and each of these protons is weakly dipolar coupled to a proton bath as indicated by the green arrows.

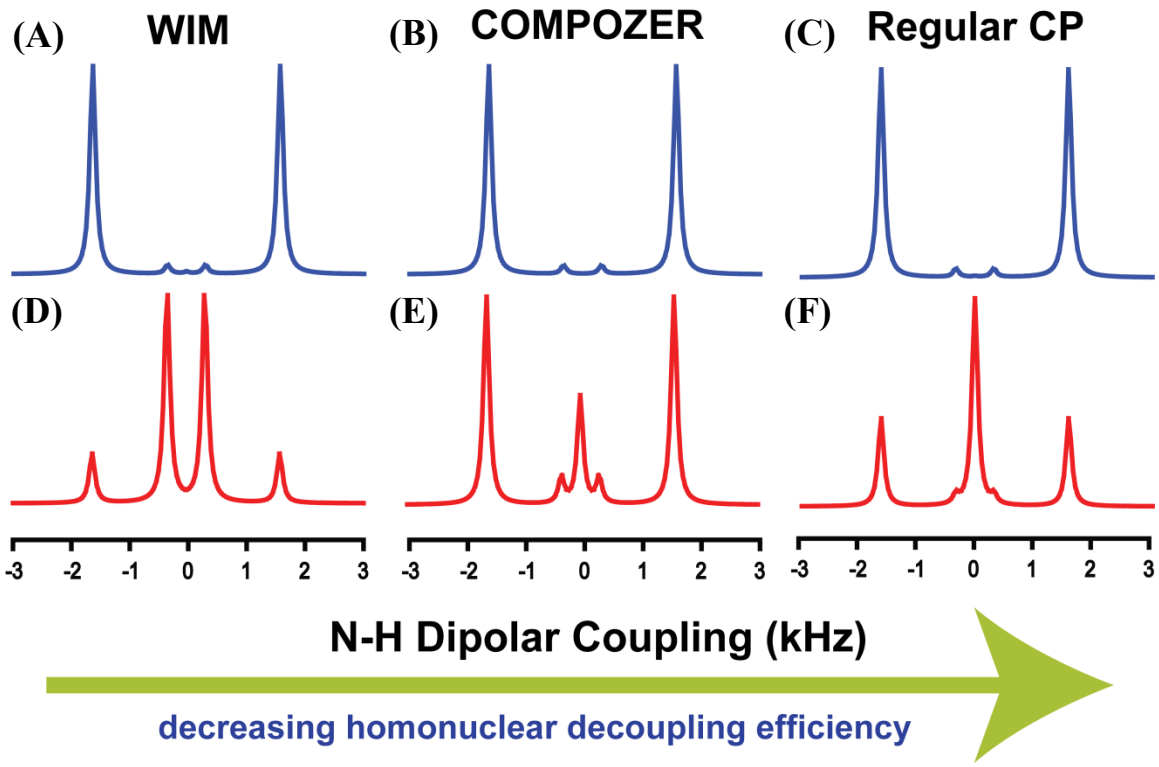

Figure 4.8 Numerically simulated PELF spectra under different magnetization transfer schemes. It should be noted that WIM is known for its efficient suppression of ^{1}H-^{1}H dipolar couplings and is better than the COMPOZER-CP sequence. On the other hand, the regular CP sequence does not employ any special sequence to suppress ^{1}H-^{1}H dipolar couplings. Spectra (A-C) were simulated using a contact time of 250 μs and spectra (D-F) were simulated using a contact of 3 ms.

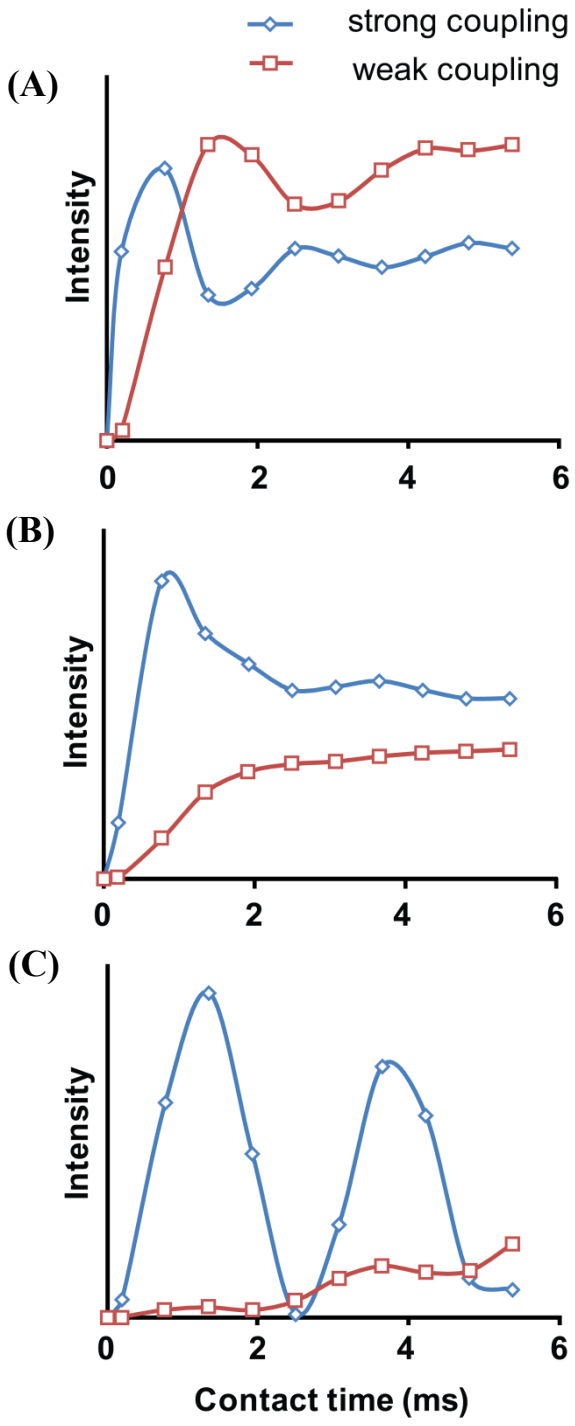

Figure 4.9 Simulated magnetization transfer efficiency as a function of transfer time by a regular-CP (A), COMPOZER-CP (B), and WIM (C) in a 2D PELF experiment. Details are discussed in the text.

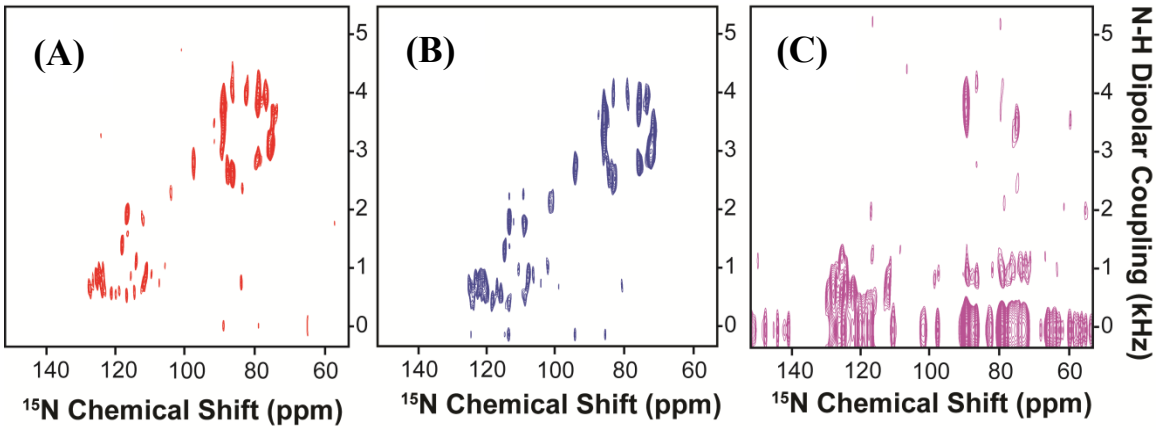

Figure 4.10 PELF spectra of magnetically-aligned bicelles containing a uniformly-15N-labeled cytochrome b5. Spectra were obtained using (A) WIM for 210 μs contact time, (b) COMPOZER-CP with an optimized contact time of 240 μs, and (c) RAMP-CP with an optimized contact time of 800 μs. All PELF spectra were acquired using a ^{1}H RF field strength of 41 kHz and SPINAL proton decoupling (61) during acquisition. All spectra are shown at the same contour level for a direct comparison.

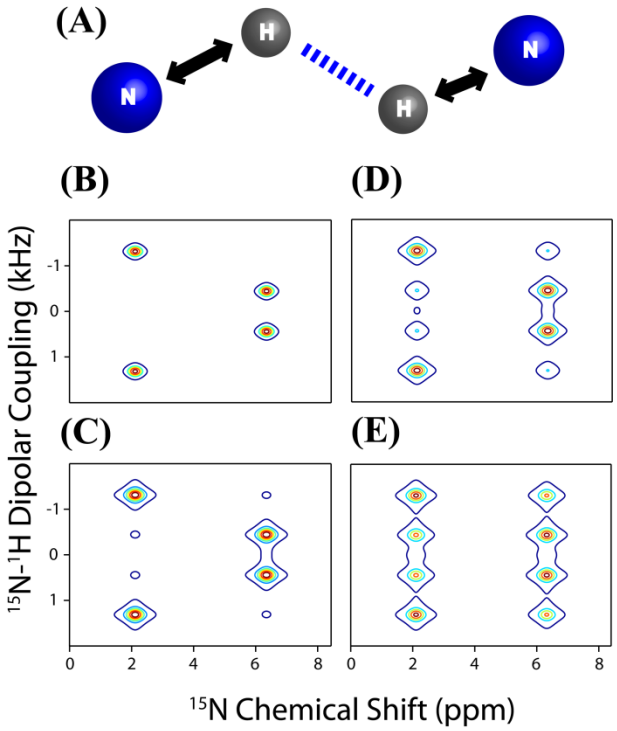

Figure 4.11 A series of simulated PELF-MIX spectra of the spin system shown in (A) taken at mixing times of (B) 0, (C) 5, (D) 15 and (E) 30 ms.

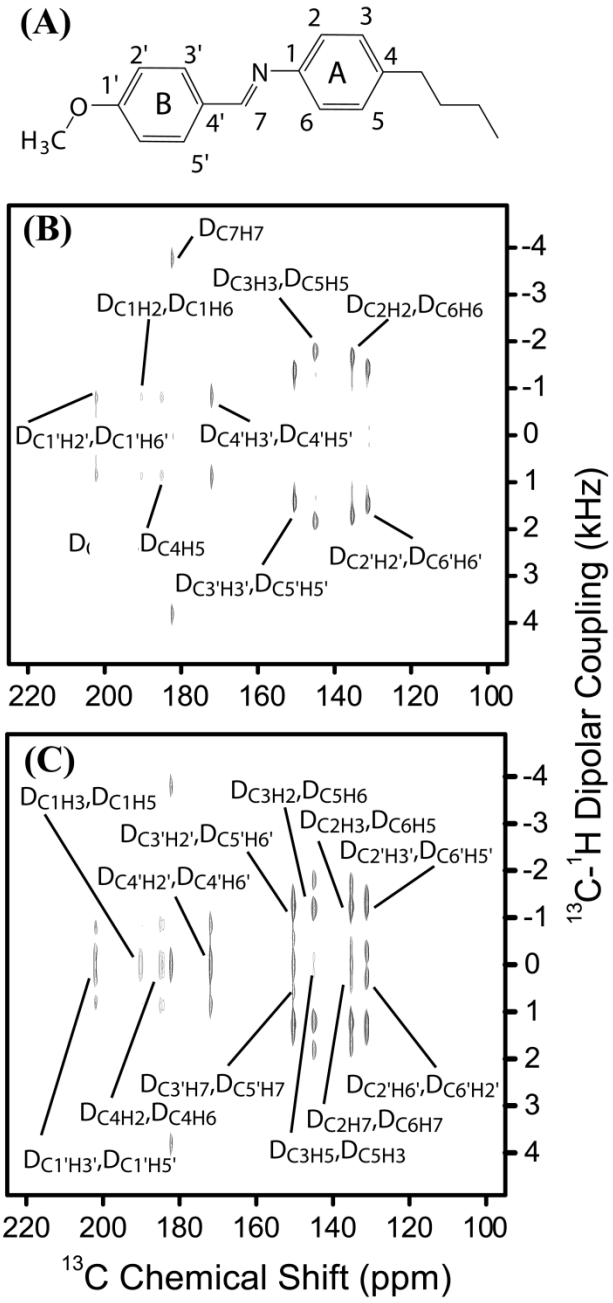

Figure 4.12 Experimental demonstration of the PELF-MIX sequence. (A) The structure of a MBBA molecule. (B) A 2D PELF spectrum of an aligned sample of MBBA at t_{mix} = 0. (C) A 2D PELF-MIX spectrum of MBBA at t_{mix} = 150 ms.

4.8 References

1. Loria, J. P., R. B. Berlow, and E. D. Watt. 2008. Characterization of Enzyme Motions by Solution NMR Relaxation Dispersion. Acc. Chem. Res. 41:214-221.

2. Korzhnev, D. M., K. Kloiber, V. Kanelis, V. Tugarinov, and L. E. Kay. 2004. Probing Slow Dynamics in High Molecular Weight Proteins by Methyl-TROSY NMR Spectroscopy: Application to a 723-Residue Enzyme. J. Am. Chem. Soc. 126:3964-3973.

3. Skrynnikov, N. R., F. A. A. Mulder, B. Hon, F. W. Dahlquist, and L. E. Kay. 2001. Probing Slow Time Scale Dynamics at Methyl-Containing Side Chains in Proteins by Relaxation Dispersion NMR Measurements: Application to Methionine Residues in a Cavity Mutant of T4 Lysozyme. J. Am. Chem. Soc. 123:4556-4566.

4. Zintsmaster, J. S., B. D. Wilson, and J. W. Peng. 2008. Dynamics of Ligand Binding from ^{13}C NMR Relaxation Dispersion at Natural Abundance. J. Am. Chem. Soc. 130:14060-14061.

5. Dürr, U. H. N., L. Waskell, and A. Ramamoorthy. 2007. The cytochromes P450 and b_5 and their reductases--Promising targets for structural studies by advanced solid-state NMR spectroscopy. Biochim. Biophys. Acta 1768:3235-3259.

6. Ellis, J., A. Gutierrez, I. L. Barsukov, W.-C. Huang, J. G. Grossmann, and G. C. K. Roberts. 2009. Domain Motion in Cytochrome P450 Reductase. J. Biol. Chem. 284:36628-36637.

7. Liang, B. Y., and L. K. Tamm. 2007. Structure of outer membrane protein G by solution NMR spectroscopy. Proc. Natl. Acad. Sci. USA 104:16140-16145.

8. Arora, A., F. Abildgaard, J. H. Bushweller, and L. K. Tamm. 2001. Structure of outer membrane protein A transmembrane domain by NMR spectroscopy. Nat. Struct. Mol. Biol. 8:334-338.

9. Hwang, P. M., R. E. Bishop, and L. E. Kay. 2004. The integral membrane enzyme PagP alternates between two dynamically distinct states. Proc. Natl. Acad. Sci. USA 101:9618-9623.

10. Hwang, P. M., W. Y. Choy, E. I. Lo, L. Chen, J. D. Forman-Kay, C. R. H. Raetz, G. G. Prive, R. E. Bishop, and L. E. Kay. 2002. Solution structure and dynamics of the outer membrane enzyme PagP by NMR. Proc. Natl. Acad. Sci. USA 99:13560-13565.

11. Porcelli, F., R. Verardi, L. Shi, K. A. Henzler-Wildman, A. Ramamoorthy, and G. Veglia. 2008. NMR structure of the cathelicidin-derived human antimicrobial peptide LL-37 in dodecylphosphocholine micelles. Biochemistry 47:5565-5572.

12. Porcelli, F., B. A. Buck-Koehntop, S. Thennarasu, A. Ramamoorthy, and G. Veglia. 2006. Structures of the dimeric and monomeric variants of magainin antimicrobial peptides (MSI-78 and MSI-594) in micelles and bilayers, determined by NMR spectroscopy. Biochemistry 45:5793-5799.

13. Traaseth, N. J., J. J. Buffy, J. Zamoon, and G. Veglia. 2006. Structural dynamics and topology of phospholamban in oriented lipid bilayers using multidimensional solid-state NMR. Biochemistry 45:13827-13834.

14. Traaseth, N. J., L. Shi, R. Verardi, D. G. Mullen, G. Barany, and G. Veglia. 2009. Structure and topology of monomeric phospholamban in lipid membranes determined by a hybrid solution and solid-state NMR approach. Proc. Natl. Acad. Sci. USA 106:10165-10170.

15. Van Horn, W. D., H. J. Kim, C. D. Ellis, A. Hadziselimovic, E. S. Sulistijo, M. D. Karra, C. L. Tian, F. D. Sonnichsen, and C. R. Sanders. 2009. Solution Nuclear Magnetic Resonance Structure of Membrane-Integral Diacylglycerol Kinase. Science 324:1726-1729.

16. Ravindranathan, K. P., E. Gallicchio, A. E. McDermott, and R. M. Levy. 2007. Conformational dynamics of substrate in the active site of cytochrome P450BM-3/NPG complex: Insights from NMR order parameters. J. Am. Chem. Soc. 129:474-475.

17. Goldbourt, A., B. J. Gross, L. A. Day, and A. E. McDermott. 2007. Filamentous phage studied by magic-angle spinning NMR: Resonance assignment and secondary structure of the coat protein in Pf1. J. Am. Chem. Soc. 129:2338-2344.

18. Zhou, D. H., G. Shah, C. Mullen, D. Sandoz, and C. M. Rienstra. 2009. Proton-Detected Solid-State NMR Spectroscopy of Natural-Abundance Peptide and Protein Pharmaceuticals. Angewandte Chemie-International Edition 48:1253-1256.

19. Ader, C., R. Schneider, S. Hornig, P. Velisetty, E. M. Wilson, A. Lange, K. Giller, I. Ohmert, M. F. Martin-Eauclaire, D. Trauner, S. Becker, O. Pongs, and M. Baldus. 2008. A structural link between inactivation and block of a K+ channel. Nat. Struct. Mol. Biol. 15:605-612.

20. Traaseth, N. J., R. Verardi, K. D. Torgersen, C. B. Karim, D. D. Thomas, and G. Veglia. 2007. Spectroscopic validation of the pentameric structure of phospholarnban. Proc. Natl. Acad. Sci. USA 104:14676-14681.

21. Ramamoorthy, A., S. K. Kandasamy, D. K. Lee, S. Kidambi, and R. G. Larson. 2007. Structure, topology, and tilt of cell-signaling peptides containing nuclear

localization sequences in membrane bilayers determined by solid-state NMR and molecular dynamics simulation studies. Biochemistry 46:965-975.

22. Lambotte, S., P. Jasperse, and B. Bechinger. 1998. Orientational distribution of alpha-helices in the colicin B and E1 channel domains: A one and two dimensional N-15 solid-state NMR investigation in uniaxially aligned phospholipid bilayers. Biochemistry 37:16-22.

23. Dürr, U. H. N., K. Yamamoto, S.-C. Im, L. Waskell, and A. Ramamoorthy. 2007. Solid-State NMR Reveals Structural and Dynamical Properties of a Membrane-Anchored Electron-Carrier Protein, Cytochrome b5. J. Am. Chem. Soc. 129:6670-6671.

24. Diller, A., C. Loudet, F. Aussenac, G. Raffard, S. Fournier, M. Laguerre, A. Grelard, S. J. Opella, F. M. Marassi, and E. J. Dufourc. 2009. Bicelles: A natural 'molecular goniometer' for structural, dynamical and topological studies of molecules in membranes. Biochimie 91:744-751.

25. De Angelis, A. A., S. C. Howell, A. A. Nevzorov, and S. J. Opella. 2006. Structure determination of a membrane protein with two trans-membrane helices in aligned phospholipid bicelles by solid-state NMR spectroscopy. J. Am. Chem. Soc. 128:12256-12267.

26. Buffy, J. J., N. J. Traaseth, A. Mascioni, P. L. Gor'kov, E. Y. Chekmenev, W. W. Brey, and G. Veglia. 2006. Two-dimensional solid-state NMR reveals two topologies of sarcolipin in oriented lipid bilayers. Biochemistry 45:10939-10946.

27. Esteban-Martin, S., E. Strandberg, G. Fuertes, A. S. Ulrich, and J. Salgado. 2009. Influence of Whole-Body Dynamics on ^{15}N PISEMA NMR Spectra of Membrane Proteins: A Theoretical Analysis. Biophys. J. 96:3233-3241.

28. Traaseth, N. J., K. N. Ha, R. Verardi, L. Shi, J. J. Buffy, L. R. Masterson, and G. Veglia. 2008. Structural and dynamic basis of phospholamban and sarcolipin inhibition of Ca2+-ATPaset. Biochemistry 47:3-13.

29. Page, R. C., S. Kim, and T. A. Cross. 2008. Transmembrane helix uniformity examined by spectral mapping of torsion angles. Structure 16:787-797.

30. Ramamoorthy, A., C. H. Wu, and S. J. Opella. 1995. 3-Dimensional Solid-State NMR Experiment that Correlates the Chemical-Shift and Dipolar Coupling Frequencies of 2 Heteronuclei. J. Magn. Reson. 107:88-90.

31. Dvinskikh, S., U. H. N. Durr, K. Yamamoto, and A. Ramamoorthy. 2006. A high-resolution solid-state NMR approach for the structural studies of bicelles. Journal of the American Chemical Society 128:6326-6327.

32. Dvinskikh, S., U. H. N. Durr, K. Yamamoto, and A. Ramamoorthy. 2006. A high-resolution solid-state NMR approach for the structural studies of bicelles. J. Am. Chem. Soc. 128:6326-6327.

33. Szabo, A., and N. S. Ostlund. 1996. Modern Quantum Chemistry: Introduction to Advanced Electronic Structure Theory. Dover.

34. Griffiths, D. J. 2005. Introduction to Quantum Mechanics. Pearson Prentice Hall.

35. Slichter, C. P. 1990. Principles of Magnetic Resonance. Springer-Verlag, New York.

36. Sakurai, J. J. 1994. Modern Quantum Mechanics. Addison-Wesley Pub. Co.

37. Sorensen, O. W., G. W. Eich, M. H. Levitt, G. Bodenhausen, and R. R. Ernst. 1983. Product Operator-Formalism for the Description of NMR Pulse Experiments. Prog. Nucl. Mag. Res. Sp. 16:163-192.

38. Pines, A., and J. S. Waugh. 1972. Quantitative aspects of coherent averaging. simple treatment of resonance offset processes in multiple-pulse NMR. J. Magn. Reson. 8:354-365.

39. Maricq, M. M. 1982. Application of average Hamiltonian theory to the NMR of solids. Phys. Rev.B 25:6622.

40. Gullion, T. 2006. Rotational-Echo, Double-Resonance NMR. In Modern Magnetic Resonance. Springer Netherlands. 713-718.

41. Haeberlen, U., and J. S. Waugh. 1968. Coherent Averaging Effects in Magnetic Resonance. Phys. Rev. 175:453-467.

42. Hartmann, S. R., and E. L. Hahn. 1962. Nuclear Double Resonance in the Rotating Frame. Phys. Rev. 128:2042.

43. Muller, L., A. Kumar, T. Baumann, and R. R. Ernst. 1974. Transient Oscillations in NMR Cross-Polarization Experiments in Solids. Physical Review Letters 32:1402-1406.

44. Fukuchi, M., A. Ramamoorthy, and K. Takegoshi. 2009. Efficient cross-polarization using a composite 0° pulse for NMR studies on static solids. J. Magn. Reson. 196:105-109.

45. Hong, M., A. Pines, and S. Caldarelli. 1996. Measurement and assignment of long-range C-H dipolar couplings in liquid crystals by two-dimensional NMR spectroscopy. J. Phys. Chem. 100:14815-14822.

46. Hong, M., K. Schmidt-Rohr, and H. Zimmermann. 1996. Conformational constraints on the headgroup and sn-2 chain of bilayer DMPC from NMR dipolar couplings. Biochemistry 35:8335-8341.

47. Dvinskikh, S. V., K. Yamamoto, and A. Ramamoorthy. 2006. Heteronuclear isotropic mixing separated local field NMR spectroscopy. J. Chem. Phys. 125034507.

48. Veshtort, M., and R. G. Griffin. 2006. SPINEVOLUTION: A powerful tool for the simulation of solid and liquid state NMR experiments. J. Magn. Reson. 178:248-282.

49. Clarke, T. A., S. C. Im, A. Bidwai, and L. Waskell. 2004. The role of the length and sequence of the linker domain of cytochrome b_5 in stimulating cytochrome P4502B4 catalysis. J. Biol. Chem. 279:36809-36818.

50. Xu, J., J. Struppe, and A. Ramamoorthy. 2008. Two-dimensional homonuclear chemical shift correlation established by the cross-relaxation driven spin diffusion in solids. J. Chem. Phys. 128.

51. Wu, C. H., B. B. Das, and S. J. Opella. 2010. ^{1}H-^{13}C Hetero-Nuclear Dipole-Dipole Couplings of Methyl Groups in Stationary and Magic Angle Spinning Solid-State NMR Experiments of Peptides and Proteins. J. Magn. Reson. 202:127-134.

52. Sprangers, R., and L. E. Kay. 2007. Quantitative dynamics and binding studies of the 20S proteasome by NMR. Nature 445:618-622.

53. Tugarinov, V., R. Sprangers, and L. E. Kay. 2004. Line narrowing in methyl-TROSY using zero-quantum ^{1}H-^{13}C NMR spectroscopy. J. Am. Chem. Soc. 126:4921-4925.

54. Strandberg, E., S. Özdirekcan, D. T. S. Rijkers, P. C. A. van der Wel, R. E. Koeppe Ii, R. M. J. Liskamp, and J. Antoinette Killian. 2004. Tilt Angles of Transmembrane Model Peptides in Oriented and Non-Oriented Lipid Bilayers as Determined by 2H Solid-State NMR. Biophys. J. 86:3709-3721.

55. van der Wel, P. C. A., E. Strandberg, J. A. Killian, and R. E. Koeppe Ii. 2002. Geometry and Intrinsic Tilt of a Tryptophan-Anchored Transmembrane α-Helix Determined by ^{2}H NMR. Biophys. J. 83:1479-1488.

56. Tolman, J. R., and K. Ruan. 2006. NMR residual dipolar couplings as probes of biomolecular dynamics. Chem. Rev. 106:1720-1736.

57. Zhuang, T., H. Leffler, and J. H. Prestegard. 2006. Enhancement of bound-state residual dipolar couplings: Conformational analysis of lactose bound to Galectin-3. Protein Sci. 15:1780-1790.

58. Zhang, Q., A. C. Stelzer, C. K. Fisher, and H. M. Al-Hashimi. 2007. Visualizing spatially correlated dynamics that directs RNA conformational transitions. Nature 450:1263-1267.

59. Park, S. H., A. A. Mrse, A. A. Nevzorov, A. A. De Angelis, and S. J. Opella. 2006. Rotational diffusion of membrane proteins in aligned phospholipid bilayers by solid-state NMR spectroscopy. J. Magn. Reson. 178:162-165.

60. Kalodimos, C. G., R. Boelens, and R. Kaptein. 2002. A residue-specific view of the association and dissociation pathway in protein-DNA recognition. Nat. Struct. Mol. Biol. 9:193-197.

61. Fung, B. M., A. K. Khitrin, and K. Ermolaev. 2000. An Improved Broadband Decoupling Sequence for Liquid Crystals and Solids. J. Magn. Reson. 142:97-101.

CHAPTER 5

CONCLUSIONS AND FUTURE DIRECTIONS

5.1 Conclusions

The goal of this project was to investigate the interaction between cell membrane binding molecules, such as peptides and drug compounds, and biological lipid bilayers. Based on solid-state NMR and DSC experiments, we have revealed that IAPP, a peptide hormone implicated in type II diabetes, disrupts biological membranes by a curvature induction mechanism (1). Our solid-state NMR experimental studies have also shown that PAMAM dendrimers are thermodynamically stable when inserted inside zwitterionic lipid bilayers. In addition to these biological NMR studies, new NMR methods for studying the structure and dynamics of lipid bilayers and lipid bilayer associated molecules were developed (2).

The practicality of a PELF NMR pulse sequence to generate a complete mapping of dynamics, by measuring dipolar couplings of directly bonded N-H spin pairs, of a membrane anchored cytochrome b_5 in magnetically-aligned bicelles was demonstrated (2). Importantly, under our approach, an SLF spectrum of both transmembrane and mobile regions is recorded in a single experiment, allowing for a complete correlation of protein dynamics between the two regions. Although this method is demonstrated successfully on a membrane protein, it can also be used for other aligned liquid crystalline materials. Finally, while this method of extracting dynamical information can be extended to system of two binding helices, MD simulations will be needed to include all the motions pertaining to such a complex in order to provide a proper and insightful

description regarding its motions in membranes. The PELF-MIX technique demonstrated in the present studies is capable of generating correlation between resonances as well as long-range distance constrains for structure determination of aligned samples. The use of proton spin diffusion is advantage compared to other proton driven ^{15}N-^{15}N correlations due to the use of a short t_{mix} and the capability of probing long distance correlations (3). These PELF-MIX experimental approaches are applicable to wide range of aligned systems ranging from membrane proteins to liquid crystals.

It was also found that IAPP peptide fragments induce a high degree of negative curvature strain in lipid bilayers (1). It is therefore likely that one of the mechanisms by which IAPP peptides permeabilize lipid bilayers involves either the formation of toroidal pores or non-specific membrane disruption due to excessive negative curvature strain. The induction of a similar degree of negative curvature by 1-19 N-terminal fragments of IAPP, which do not form amyloid fibers when embedded in the membrane, indicates amyloid formation is not essential for this process. Importantly, we found that non-toxic $rIAPP_{1-37}$ does not induce a great degree of negative curvature strain, suggesting that toxicity may be linked to the induction of negative curvature. Since membrane curvature can be modified by ligand binding, we believe that results from this study will be useful to design compounds that can be used to prevent the interaction of IAPP with the cell membrane and therefore the cell-toxicity of IAPP. This study demonstrates that bicelles are useful to study the affinity of ligands to bind with curved regions of the cell membrane and also to investigate the role of toroidal pores in the function of membrane disruptive peptides like antimicrobial peptides, toxin peptides, and fusion peptides.

Lastly, it was shown that dendrimers can localize deep inside zwitterionic lipid bilayers in a process apparently dominated by the hydrophobic association of the lipid acyl chain with the interior of the dendrimer. Since the hydrophobicity of the dendrimer interior can be tuned by altering the composition of the building blocks of the dendrimer (4), this finding has practical consequences both for the design of new nanodevices to both carry lipophilic drugs to biomembranes and for avoiding some of the negative aspects of unfunctionalized PAMAM dendrimers interactions with biomembranes.

5.2 Future directions

With the new NMR methods established in this project, higher resolution molecular images of lipid bilayer systems are obtainable. The increase in resolution made available by the use of the PELF techniques developed in this project can be used to study the interactions of several amyloid and antimicrobial peptides in a high-throughput manner. Trends in the behavior of these peptides are starting to emerge and thre is some interest studying these trends (5-7), which will require the use of NMR methods that are convenient and provide fast acquisition of detailed structural and dynamical information. The PELF techniques proposed in this project are robust and can be used to study a wide variety of peptides' interactions with lipid bilayers.

Understanding the mechanisms whereby these amyloid disease peptides misfold and form toxic aggregates –particularly in their initial, soluble oligomeric stages– is essential to the development of amyloid disease treatments (possible mechanisms of IAPP mediated cell membrane disruption are shown in figure 5.1). Nevertheless, because of rapid amyloid protein aggregation, detailed structural and dynamical knowledge of the toxic intermediates most relevant to the pathologies of amyloid diseases remains elusive.

NMR methodologies developed over the last few years in the Frydman lab promise to overcome the difficulties inherent in atomic-level structural studies of amyloid peptide aggregation. Particularly useful in the study of these peptides' aggregation are the SOFAST-HMQC techniques, developed by Schanda et al. (8) These methods may be applied in solid state NMR under magic angle spinning.

The aggregation of amyloid peptides in a wide variety of environments is of interest. The functionalization of dendrimers to dissolve β-amyloid peptides has recently been proposed (9). A detailed characterization of the action of these dendrimer-based therapeutics is possible with SOFAST-HMQC techniques. Particularly important in these investigations will be the effects that these therapeutics have on the transient intermediates believed to be important to the membrane disrupting activity of amyloid peptides.

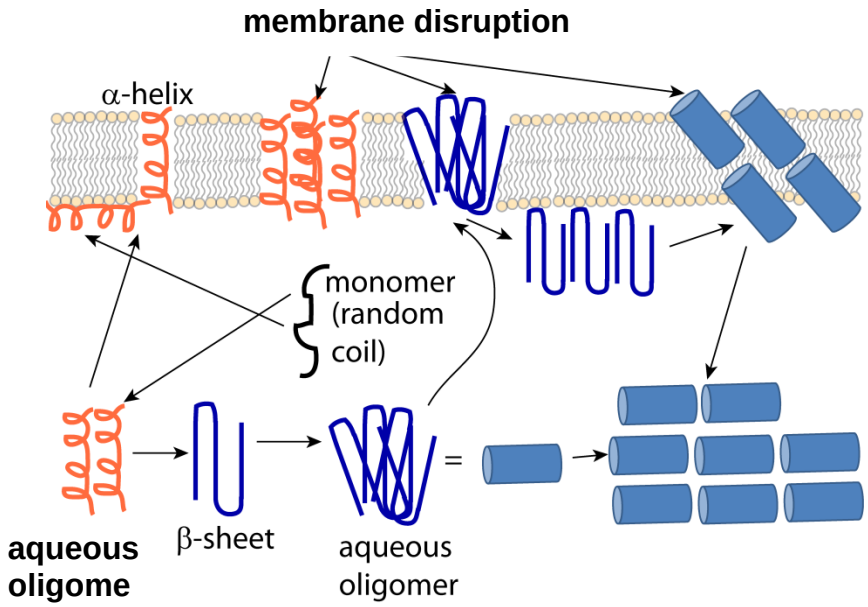

Figure 5.1 Possible mechanisms of amyloid peptide mediated cell membrane disruption.

5.3 References

1. Smith, P. E. S., J. R. Brender, and A. Ramamoorthy. 2009. Induction of Negative Curvature as a Mechanism of Cell Toxicity by Amyloidogenic Peptides: The Case of Islet Amyloid Polypeptide. J. Am. Chem. Soc. 131:4470-4478.

2. Soong, R., P. E. S. Smith, J. Xu, K. Yamamoto, S.-C. Im, L. Waskell, and A. Ramamoorthy. In press. J. Am. Chem. Soc.

3. Xu, J., J. Struppe, and A. Ramamoorthy. 2008. Two-dimensional homonuclear chemical shift correlation established by the cross-relaxation driven spin diffusion in solids. J. Chem. Phys. 128.

4. Tomalia, D. A. 2005. Birth of a new macromolecular architecture: dendrimers as quantized building blocks for nanoscale synthetic polymer chemistry. Prog. Polym. Sci. 30:294-324.

5. Kajava, A. V., U. Baxa, and A. C. Steven. 2009. β arcades: recurring motifs in naturally occurring and disease-related amyloid fibrils. FASEB J.:fj.09-145979.

6. Ruschak, A. M., and A. D. Miranker. 2009. The Role of Prefibrillar Structures in the Assembly of a Peptide Amyloid. J. Mol. Biol. 393:214-226.

7. Abedini, A., and D. P. Raleigh. 2009. A role for helical intermediates in amyloid formation by natively unfolded polypeptides? Physical Biology 6.

8. Schanda, P., and B. Brutscher. 2005. Very fast two-dimensional NMR spectroscopy for real-time investigation of dynamic events in proteins on the time scale of seconds. J. Am. Chem. Soc. 127:8014-8015.

9. Shi, W., S. Dolai, S. Rizk, A. Hussain, H. Tariq, S. Averick, W. L'Amoreaux, A. El Ldrissi, P. Banerjee, and K. Raja. 2007. Synthesis of monofunctional curcumin derivatives, clicked curcumin dimer, and a PAMAM dendrimer curcumin conjugate for therapeutic applications. Org. Lett. 9:5461-5464.

APPENDIX A

PHOSPHORUS-31 NMR SPECTRUM OF A HUMAN ISLET AMYLOID POLYPEPTIDE AND BICELLE MIXTURE

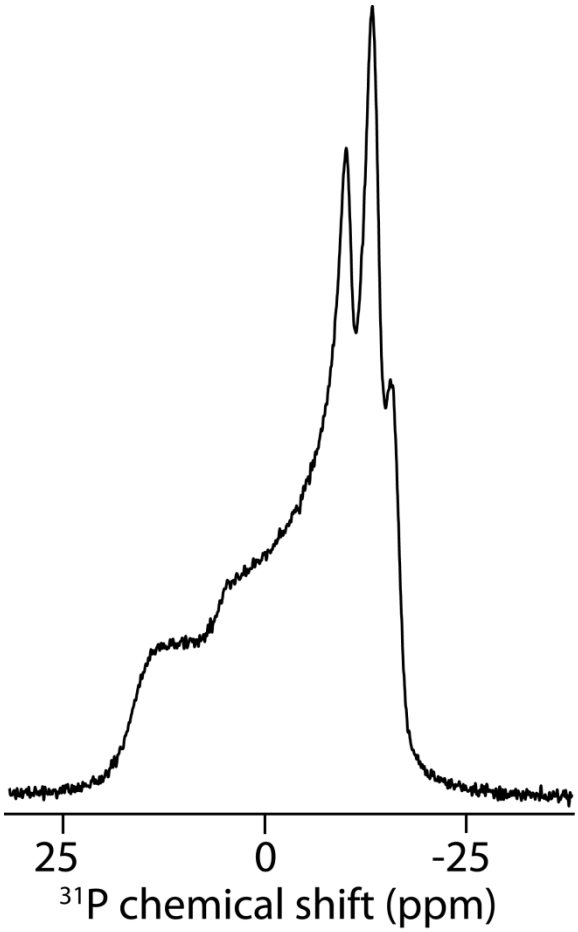

The ^{31}P NMR spectrum of the hIAPP$_{1-19}$ bicelle sample. In contrast to the rIAPP$_{1-19}$ and rIAPP$_{1-37}$ samples, hIAPP$_{1-19}$ bicelles do not align well as shown by the span of the ^{31}P chemical shift.

APPENDIX B

THE HYDRATION LEVEL OF DENDRIMER AND LIPID SAMPLES ASSESSED BY PROTON NMR

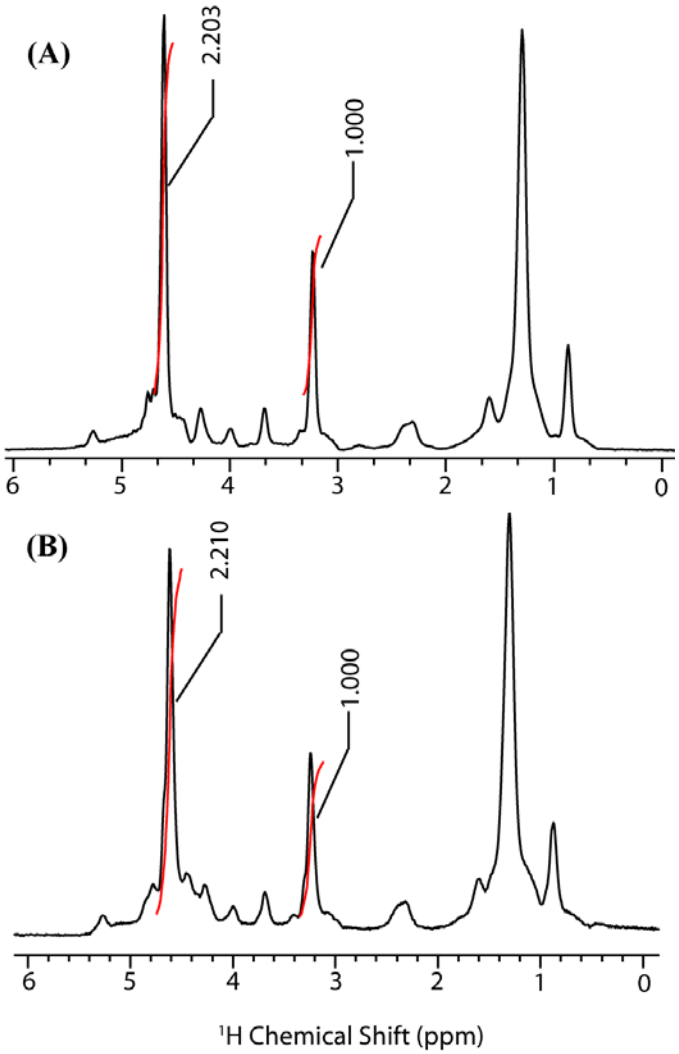

The ^{1}H spectra of **(A)** the G5 dendrimer and lipid sample and the **(B)** G7 dendrimer and lipid sample. The area of the water peak (at ~4.7 ppm) is in both cases about 2.2 times the area of the gamma 1H lipid peak (at ~3.15 ppm). There are 9 γ ^{1}H nuclei per lipid molecule and 2 ^{1}H nuclei per water molecule, which means that there are ~10 water molecules per lipid.

APPENDIX C

SAMPLE PREPARATION AND NMR EXPERIMENTAL DETAILS FOR EXPERIMENTAL PELF DEMONSTRATIONS

C1. Preparation of magnetically-aligned bicelles

A detailed procedure on the preparation and characterization of magnetically-aligned bicelles containing cytochrome b_5 can be found in our previous publication (1) while it is outlined very briefly here. In general, the quantity of lipids in bicelles are calculated according to the q = [DMPC]/[DHPC] ratio and in the present study bicelles with a q value of 3.5 was used. Lipid-detergent mixture was hydrated with an appropriate amount of HEPES buffer (10 mM HEPES, pH = 7.0) to obtain the desired wt% of lipids, typically ~ 50 wt%, for the reconstitution of a mutant cytrochrome b_5. The solution of lipid-detergent mixture was gently vortexed after every freeze/thaw cycle until an optically clear solution was obtained.

C2. Reconstitution of mutant-cytrochrome b_5 in bicelles

Uniformly ^{15}N-labeled mutant-cytochrome b_5 expressed and purified according to previous protocols (1) was concentrated into a stock solution of 4.3 mM. The amount of protein used in each experiment was calculated according to the desired lipid to protein ratio. A 300:1 DMPC:protein ratio was used in this study. The protein was reconstituted into bicelles by adding an appropriate amount of the protein stock solution to a bicelle solution and the final lipid concentration was diluted to 25 wt% and the final volume was

160 μL. The solution was gently vortexed to ensure proper mixing of protein and lipids and was subsequently transfer to an NMR rotor.

C3. PELF-COMPOZER and PELF-WIM NMR experiments

NMR experiments were carried out on a Varian Infinity-600 MHz solid-state NMR spectrometer using a 4 mm triple-resonance magic angle spinning (MAS) probe under static sample conditions. The ^{1}H and ^{15}N resonance frequencies were 599.8 and 60.78 MHz respectively. About 40 mg of lipids mixed with 3 mg of mutant cytochrome b_5 were loaded in a 4 mm NMR glass tube of 4 cm length, and the tube was closed tightly with a Teflon tape to avoid any leakage inside the probe and completely closed with a cap. The sample was then equilibrated for about 30 minutes inside the magnet at the measurement temperature prior to the signal acquisition. The 2D PELF spectra were obtained using the following parameters: 5 μs 90^0 pulse, 40 kHz ^{15}N sweep width, 28 t_1 increments, 3000 scans, a 3 s recycling delay, and a 25 kHz ^{1}H decoupling. A 50 kHz BLEW-12 (Burum, Linder, Ernst Windowless) (2) pulse sequence was used for homonuclear decoupling during the t_1 period and the SPINAL-64 (3) pulse sequence was used to decouple protons during signal acquisition in the t_2 period. The PELF-MIX experiments were performed on Varian 400M VNMRS spectrometer equipped with a low-E double channel probe. The NMR experiments on MBBA were carried out at 25°C, and the sample was in the liquid crystalline phase, aligned by the external NMR magnetic field.

DKDVKYYTLEEIKKHNHSKSTWLIKHHKVYDLTKFLEEHPGGEEVLREQAGGD

ATENFEDVGHSTDARELSKTFIIGELHPDDRSKLSKPMETLITTVDSNSSWWTNW

VIPAISALIVALMY

Figure C1. The amino acid sequence of a full-length wild-type rabbit cytochrome b_5. High-resolution structures of the soluble domain of the protein have been reported from solution NMR and X-ray crystallography studies, whereas the structure of the full-length protein is unknown as it has not been amenable for studies using high-resolution methods. Secondary structures such as α-helix (blue) and β-sheet (green) are indicated based on previous studies. The 8 amino acids that were deleted from the linker region of the wild-type cytochrome b_5 to obtain a mutant are shown in red.

C4. References

1. Dürr, U. H. N., L. Waskell, and A. Ramamoorthy. 2007. The cytochromes P450 and b_5 and their reductases--Promising targets for structural studies by advanced solid-state NMR spectroscopy. Biochim. Biophys. Acta 1768:3235-3259.

2. Burum, D. P., M. Linder, and R. R. Ernst. 1981. Low-Power Multipulse Line Narrowing in Solid-State NMR. J. Magn. Reson. 44:173-188.

3. Fung, B. M., K. Ermolaev, and Y. L. Yu. 1999. ^{13}C NMR of liquid crystals with different proton homonuclear dipolar decoupling methods. J. Magn. Reson. 138:28-35.